Modeling, Analysis and Control of DC Hybrid Power Systems

by

Yanhui Xie

A dissertation submitted in partial fulfillment
of the requirements for the degree of
Doctor of Philosophy
(Naval Architecture and Marine Engineering)
in The University of Michigan
2010

Doctoral Committee:

Professor Jing Sun, Co-Chair
Professor James S. Freudenberg, Co-Chair
Associate Professor Chunting Mi
Assistant Professor Ryan Eustice

Dedicated to my daughter, Xiwen Xie, and to my wife, Yunyun Ni.

Acknowledgements

Many people have contributed to the production of this dissertation, although only my name appears on the cover. Hence, I absolutely owe my gratitude to all those people who encouraged and helped me to finally finish this dissertation.

My deepest gratitude is to my advisors, Professor Jing Sun and Professor James S. Freudenberg, at the University of Michigan. Their consistent encouragement and support helped me overcome many challenges and finish this dissertation. I am extremely thankful to Professor Chunting Mi. I spent almost one year in his power electronics lab to build our hybrid power system testbed which has significantly contributed to this dissertation. I am also thankful to Professor Ryan Eustice for his constructive comments and suggestions.

I would like to gratefully and sincerely thank all my friends and colleagues in the RACE Lab at the University of Michigan for valuable discussions and enjoyable friendship. Specifically, I would like to thank Reza Ghaemi, Handa Xi, Zhen Li, Gayathri Seenumani, Christopher Vermillion, Vasilios Tsourapas, Soryeok Oh, Amey Karnik, Jian Chen, and Zhao Lu.

I also like to acknowledge the U.S. Office of Naval Research for the financial support under Grants No. N00014-08-1-0611 and N00014-05-1-0533.

Finally, and most importantly, I would like to thank my wife Yunyun Ni. Without her support, encouragement, patience and unwavering love, I may never have finished

this dissertation. I thank my parents, Shiqi Xie and Xiangyun Meng, and Yunyun's parents, Guofu Ni and Huiying Zhang, who always have their faith in me and give me the support and strength to overcome the difficulties.

Contents

List of Figures

Figure

List of Tables

Table

List of Abbreviations

AES	All Electric Ship
CM-PWM	Current Mode Pulse Width Modulation
DABC	Dual Active Bridge Converter
DHPS	DC Hybrid Power System
EPM	Electric Propulsion Module
FBC	Full Bridge Converter
FPS	Fuel Processing System
FR	Fuel Reformer
HDS	Hydro Desulphurizer
HEX	Heat Exchanger
MIXER	Mixer
InPA-SQP	Integrated Perturbation Analysis and Sequential Quadratic Programming
IPS	Integrated Power System
LMPC	Linear Model Predictive Control
MPC	Model Predictive Control
NLMPC	Nonlinear Model Predictive Control

PCM	Power Conversion Module
PEM	Polymer Electrolyte Membrane
PGM	Power Generation Module
PMSM	Permanent Magnet Synchronous Motor
PSM	Phase Shift Modulation
PWM	Pulse Width Modulation
WGS	Water Gas Shift reactor
UPS	Uninterruptible Power Supply

Abstract

Modeling, Analysis and Control of DC Hybrid Power Systems

by

Yanhui Xie

Co-Chairs: Jing Sun and James S. Freudenberg

All electric ships are featured with integrated power systems which combine electric propulsion technology with heterogeneous power generation and distribution technologies to form one single electrical platform. The auxiliary and main power generation system form an isolated hybrid power system to feed the ship service loads and to meet the propulsion power requirement. Although for decades, the methodologies for power converter control have been explored in many publications, the modeling, analysis, and control of hybrid power systems with multiple power converters remains an interesting open problem, leading to its exclusive focus in this dissertation.

Along with the opportunities introduced by hybrid power systems, the interconnectivity and complexity represent a major system analysis, design and optimization challenge, calling for the development of effective tools. Therefore, a comprehensive testbed is developed. Moreover, component level modeling, analysis and modulation strategy development are performed to ensure system level performance. A new power flow model for the dual active bridge converter is derived. The new model provides a physical interpretation of the observed phenomena and identifies

other characteristics that are validated by experiments. To overcome the drawbacks of traditional modulation strategies, a novel modulation strategy is developed for the dual active bridge converter. The experimental results verified that, if the new strategy is used to modulate the dual active bridge converter, this testbed can be used as an effective tool for optimal power management algorithm development for the hybrid power systems.

The development of advanced control algorithms, together with the increased computational power of microprocessors, enables us to deal with the control problem from a new perspective. In this dissertation, the voltage regulation problem for a full bridge DC/DC converter is formulated as both a linear and a nonlinear Model Predictive Control (MPC) problem with a nonlinear constraint that captures the peak current protection requirement. The experimental results reveal that both the MPC algorithms can successfully achieve voltage regulation and peak current protection. The successful implementation of the MPC schemes on the full bridge DC/DC converter paves the way for future system-level advanced control algorithm development for hybrid power systems.

Chapter 1

Introduction

Next generation All Electric Ships (AES) is enabled by Integrated Power Systems (IPS) which incorporate a set of primary and auxiliary power sources to provide the propulsion power and, at the same time, energize the shipboard electric loads [1, 2]. The IPS is mainly comprised of Power Generation Modules (PGM), Power Conversion Modules (PCM), Electric Propulsion Modules (EPM) and vital/nonvital loads. The PGM could be a gas turbine, diesel engine or fuel cell power system. The auxiliary power generation system, such as a fuel cell power system, usually only energizes the ship service loads while the main power generation systems, such as the gas turbine and diesel engine, provide power for both the propulsion loads and the ship service loads. Therefore, the auxiliary and main power generation system form an isolated hybrid power system to feed the ship service loads and to meet the propulsion power requirements.

As the power conditioning device, the power converter is the enabling technology to address the power management problems for the hybrid power system. However, for the isolated hybrid power system of the IPS, the wide range of operating conditions, the requirements for fast power response and load following, coupled with the

stringent constraints of high power quality and system reliability, have imposed challenges for control of the power converters whose dynamic characteristics are highly nonlinear. Motivated by the challenges and importance of the hybrid power system controls, this dissertation has focused on modeling, analysis and control of power converters for the hybrid power systems.

1.1 Background and Literature Review

1.1.1 Integrated Power System of All Electric Ships

An Integrated Power System (IPS) of an AES provides electric power to all shipboard loads, including the propulsion system, with an integrated plant [1, 2]. The IPS associated with the AES typically has electric propulsion, sophisticated electric weaponry systems and ship service as electric loads. Unlike a traditional mechanical propulsion system which uses long shafts to deliver energy from the prime movers to the propulsion systems, the electric propulsion systems, including motor drives and electric motors, are connected to the power plants through an electrical distribution system. Under emergent battle scenarios, a large amount of power can be unlocked from the propulsion system to support the electric weaponry systems. Moreover, ship service loads are powered from the same power network as the electric propulsion system through a power distribution system.

To enhance the reliability and survivability of the IPS, Zonal Electric Distribution System (ZEDS) was introduced [3,4]. Unlike the conventional radial electric distribution system which radially distributes power to the loads through load centers, ZEDS employs two main buses (starboard bus and port bus) to provide redundant power flow paths for vital loads. With the introduction of Power Electronic Building Block (PEBB) [5,6], the ZEDS could seamlessly and dynamically reconfigure the power flow

paths in response to different priorities of loads for different real time battle scenarios.

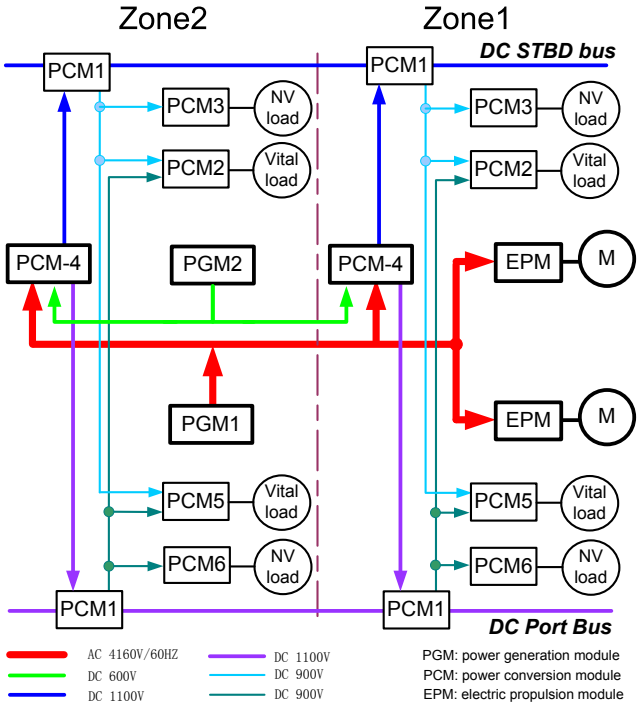

Figure 1.1: One-line diagram for integrated power system of all electric ship.

Fig.1.1 illustrates a one-line diagram of the IPS with the zonal architecture. The two main buses of the ZEDS are simultaneously powered by both the main power generation system (marked as PGM1 in Fig.1.1) and the auxiliary power generation system (marked as PGM2 in Fig.1.1). The auxiliary power generation system is a fuel cell power system which provides power for the ZEDS through an isolated DC/DC converter. In addition, the main power generation system, namely a gas turbine/generator set, also provides power for the ZEDS through cascaded power conversion systems which consist of a rectifier (AC/DC) and an isolated DC/DC converter. Moreover, an energy storage device is often necessary to improve the transient performance of the hybrid power system. Therefore, an isolated bidirectional DC/DC converter is placed between the energy storage device and the DC bus. The PCM-4 which is consisting of the three isolated DC/DC converters serves as the power

conditioning system for the main power generation system, auxiliary power generation system and energy storage system. The output terminals of the three converters are connected together to feed DC buses of the ZEDS, therefore forming a DC Hybrid Power System (DHPS) for the IPS of an AES [92, 93].

1.1.2 DC Hybrid Power System

Hybridization through integration of multiple power sources, especially those with complementary characteristics, can achieve high system performance and reliability. For example, wind energy, if combined with micro-hydro or diesel power generation [20], [21], can provide low cost and high reliability power solutions for island and remote area communities. The integration of fuel cells to shipboard power systems [22, 93] and to automotive powertrains [23, 27–29] results in low emissions and high system efficiency.

Since these power sources have different response time and efficiency, dynamic optimal power management is critical to the power system stability, efficiency and performance [67–69]. Therefore, how to coordinate the power converters to achieve optimal efficiency and maximum reliability during transients is a big challenge for the power management system of the DHPS.

Even though power converters have been widely used in industry, commercial, and military applications, their utility in multi-source, multi-load hybrid power systems has brought many new challenges in their design, integration and control. For example, they typically require a wide operating range and fast transient response, thereby placing new emphasis on dynamic response. The need to have multiple converters work in concert also demands coordinated control to manage the dynamic interactions among involved components. On one hand, stringent safety and reliability requirements mandate a total protection of the system from constraint violation and

component failure. On the other hand, demands for high efficiency and fast transient response render the conservative safety oriented strategy insufficient. Therefore, how to achieve high system efficiency and superior transient performance without compromising system integrity becomes one of the focuses in power converter design and optimal control.

1.1.3 Full Bridge and Dual Active Bridge Converters

Since a DHPS usually has multiple energy storage device and power sources, there must be multiple power converters to serve as the power conditioning devices. The full bridge and dual active bridge topologies were initially proposed in previous studies [54], [55] for both high power density and high power applications. They are very attractive because of their zero voltage switching, low component stresses, and high power density features. Moreover, the high frequency transformer prevents fault propagation and enables a flexible output/input voltage ratio. Therefore, with a full bridge or a dual active bridge DC/DC converter as the power conditioning system, different types of power sources and energy storage systems can be applied to high DC voltage applications, such as the DC zonal electrical distribution system of an all electric ship [93].

The Dual Active Bridge Converter (DABC) has been widely used in applications such as Uninterruptible Power Supplies (UPS), battery charging and discharging systems, and auxiliary power supplies for hybrid electrical vehicles. For example, in [34], the authors investigated an off-line UPS design based on dual active bridge topology. The use of a DABC for bidirectional energy delivery between an energy storage system and a DC power system is addressed in [35–38]. In [39, 43–45], the authors evaluate different dual active bridge configurations for automotive applications. [46–48] adopt a DABC as the core circuit of the power conversion system between an AC power

system and a DC voltage source.

For applications which involve energy storage systems, DABCs are expected to operate over a wide range of operating conditions without substantial performance degradation, especially for mobile applications. However, several issues have been reported in the literature when the magnitude of the input and output voltage does not match. First, the soft-switching region, in which switching losses can be minimized, will be significantly reduced [38, 54, 55], which leads to high switching loss. Second, the circulating energy will be substantial [32, 49–51, 54, 55], which leads to high conduction loss. Therefore, high power loss and low system efficiency for certain operating conditions will be expected if the DABC operates with a wide input voltage range. Moreover, our experiments revealed several additional phenomena such as the internal power transfer and phase drift, that deteriorate the performance of the DABC [94, 95].

To eliminate the circulating energy and extend the soft-switching range, several modulation strategies are proposed and evaluated [32, 35, 36, 53]. Those strategies introduce multiple control inputs to adjust the pulse width of the AC voltage of the two full bridges and their phase difference respectively, leading to an over-actuated system with complicated characteristics. To improve the system efficiency, resonant converters have been studied extensively in [11–13, 17–19, 24–26, 30, 31, 40–42, 63]. To extend the power range of the DAB converter for ultra-capacitor applications, a triangular modulation strategy is proposed [52] for low power applications. For high power applications, the triangular shape of the inductor current leads to a high RMS value and high peak current, causing low system efficiency and high component current stress [52].

1.1.4 Power Converter Control

Several challenges arise for the DC/DC converter control design. First, the power devices of the DC/DC converters have very complicated time varying switching behavior which defines the shape of the inductor current, making the dynamic model development of power converters a challenge. Second, DC/DC converters used for mobile applications typically have a wide range of operating conditions and stringent transient performance requirements, further complicating the control design. Furthermore, the control input, which typically is the pulse width or phase shift, is bounded due to physical limitations of power converters. Finally, safe operation requirements such as peak current limitation may impose additional nonlinear constraints.

Traditionally, there are two classes of algorithms for DC/DC converter control, namely the voltage mode control and current mode control [70–73]. Voltage mode control achieves voltage regulation through a single-loop voltage control scheme. To limit the current during transient operation within safe operation range, the feedback control gain must be carefully chosen, otherwise an additional protection circuit has to be incorporated. Current mode control includes two sub-classes, namely the average current control and peak current control. In addition to a voltage feedback loop, current mode control employs an inner inductor current feedback loop to improve performance. Performance enhancements, including superb line regulation and inherent over-current protection, can be achieved for current mode control. However, current mode control has a sub-harmonic oscillation problem when the duty ratio is greater than 0.5 [74]. Besides, this method requires inductor current sensing, which increases system cost and tends to have noise sensitivity problems. The development of advanced control algorithms, together with the increased computational power of microprocessors, enables us to deal with the control problem from a new perspective. For example, one step predictive control based algorithms are applied to power

electronics system, see e.g., [75] while Model Predictive Control (MPC) has been implemented in an electric drive system for direct torque control [76, 77] and in a flying capacitor converter [78]. For the full bridge DC/DC converter under investigation, the peak current protection problem can be formulated as a constraint for an optimal control problem, which can be effectively dealt with using MPC.

MPC, also known as receding horizon control, is a class of control algorithms that optimize future plant response using a linear or a nonlinear model [79–81]. At a given time k, the first element of an optimal control sequence is applied to the plant to drive the outputs as close as possible to a desired trajectory. It is worthwhile to point out that the closed-loop system performance of MPC is directly dependent on model accuracy. In real applications, model uncertainty and disturbances can lead to steady-state error or deteriorated transient performance, especially when a linear model is employed to predict the response of a nonlinear plant with a wide operating range. To eliminate steady-state error, offset-free MPC schemes have been developed in previous studies [82–85], to guarantee offset-free control around a neighborhood of the steady-state.

In classical MPC, the control action at each time step is obtained by solving an online optimization problem with a given cost function. However, solving an optimization problem is often computationally demanding, which contributes to the fact that most successful applications have been found for systems with slow dynamics and abundant computational power. For systems with fast dynamics, explicit MPC [86,87] has been proposed which pre-computes the optimal solutions and stores them for online lookup. Explicit MPC has been implemented for fast dynamic applications with a millisecond level time constant [88]. The major challenge of implementing explicit MPC is that the number of entries in the lookup table increases exponentially as the length of the horizon increases. Moreover, in explicit MPC, nonlinear constraints are

addressed using piece-wise affine approximations. As such, the size of the lookup table increases as the required accuracy of approximation increases. Consequently, the application of an explicit MPC is limited to small problems with low dimensions [89].

To extend the applicability of the MPC to broader classes of systems with fast dynamics, a novel numerical optimization algorithm is developed to improve computational efficiency. This algorithm is referred to as the Integrated Perturbation Analysis and Sequential Quadratic Programming (InPA-SQP) solver [90,91]. It combines the computational advantages of perturbation analysis and optimality of the SQP solution by treating the optimization problem at time k as a perturbed problem at time $k-1$. This combination can significantly improve computational efficiency and is particularly useful for MPC, where an optimal control problem must be solved repeatedly over the receding horizon. It is worthwhile to point out that the InPA-SQP algorithm can be applied to solve the MPC optimal control problem for nonlinear systems with mixed state and control input constraints.

1.2 Dissertation Scope and Contributions

1.2.1 Dissertation Scope

For a DHPS, an effective control scheme managing power flow among power sources, energy storage device and loads is required to maintain power balance at all times. The main aim of the control scheme is to satisfy the requirements of the electrical loads while maximizing the system efficiency and ensuring safe operation of each individual component. The control scheme can be structured in two levels. The top level is performed by the top level power management strategy. Signals for loads, power sources, energy storage device and power converters are sent to the top level strategy to calculate the desired power to be supplied by the energy storage device

and power sources. The lower level is performed by the individual controller of each power converter. These individual controllers use the actual and the reference output power to decide how to manipulate the corresponding power converter.

Several challenges arise for the power management algorithm development for the DHPS at both levels, including:

1. Given the complexity, stringent transient requirements and inter-connectivity of the DHPS, it is necessary to develop a tool for modeling and control scheme development and validation. Such a tool must be able to support both the top level power management algorithm and lower level controller development and implementation. The top level algorithm usually involves an online optimization process whose optimal solution has to be calculated within a short time interval. The lower level controller has to calculate the control inputs and translate them into PWM signals to manipulate power converters with high switching frequency in realtime.

2. The power converters have to be able to track the corresponding power profile calculated by the top level algorithm. However, power converters of the DHPS typically have a very wide operating range. Therefore, the lower level controller and modulation strategy for each converter must be able to support the wide operating range for the power converters.

3. For the DHPS, there are many constraints to be considered to ensure safe and reliable operation of the DHPS. For example, the voltage and current limitations of power switches should not be violated; the voltage of the energy storage device must be maintained within a certain range. All these constraints impose additional challenges for power converter control.

This dissertation discusses modeling, analysis, and control of a DHPS, as well as

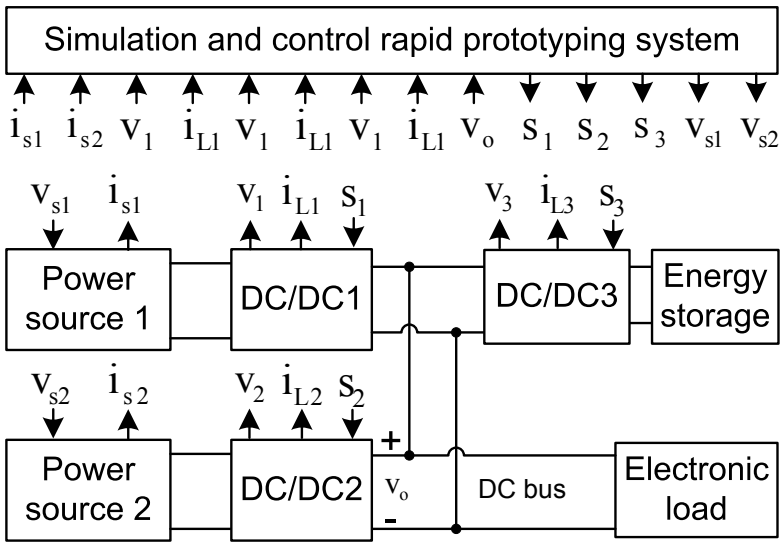

Figure 1.2: Configuration of a DHPS.

the tools development. The configuration of the DHPS addressed in this dissertation is shown in Fig.1.2, which involves two power sources and an energy storage device. This architecture reflects some of the hybrid power systems used for automotive and shipboard Auxiliary Power Unit (APU) applications. The research effort has been distributed to both the system level tools development and component (individual power converter) level modeling, analysis, and control. The developed IPS model can be used as a numerical tool for failure emulation, power flow path reconfiguration and energy management. Moreover, the integration of the three power converters with other commercial-off-the-shelf components ensures that the DHPS testbed can facilitate optimal power management initiatives. In addition to system level tools development, a large proportion of effort has been devoted to component (individual power converter) level modeling, analysis, modulation and control. This is intended to ensure that all power converters of the DHPS should be able to quickly and accurately track the power profiles given by a top level power management algorithm. Moreover, to explore the application of advanced control algorithm on power converters, MPC

schemes of the FBC also have been investigated to achieve voltage regulation without peak current violation. This paves the way for the future system-level advanced control algorithm development.

1.2.2 Contributions

This dissertation has focused on modeling, analysis and control of DC hybrid power systems. The contributions of this dissertation are summarized as follows:

- A DHPS testbed has been built at the Realtime Advanced Control Engineering Lab at the University of Michigan to provide the research infrastructure to support the power management for all electric ships. The testbed consists of a digital simulation and control rapid prototyping platform, two unidirectional FBCs, a bidirectional DABC, two programmable power sources, two programmable loads, and a supercapacitor based energy storage bank. This DHPS testbed facilitates system level analysis, optimization and control of a DC hybrid power system of an AES.

- A modularized simulation model for an IPS of an AES is developed. The IPS model has power generation modules including a gas turbine and a fuel cell power system, two electric propulsion modules and a zonal electric distribution system which, by itself, has many power conversion modules. The simulation results verify that the IPS model can be used for failure emulation, power flow path reconfiguration and energy management. This model provides an effective tool for AES system research.

- A new power flow model for a DABC over a wide operating range is developed. In addition to those major parameters used by conventional power flow analysis, this new model incorporates minor parameters, namely the power semiconduc-

tor voltage loss and dead time. The minor parameters are critical for explaining the observed internal power transfer and phase drift phenomena, which are relevant to power flow characterization of the DABC. While the new model provides a more accurate prediction over a wide range of operating conditions, it also identifies new characteristics such as reverse power transfer and energy sink that are observed in experiments. Therefore, the new model can serve as a research tool for optimal hardware design, operating range selection and power management strategy development. The experimental results illustrate the effectiveness of the new model.

- A current-mode PWM modulation strategy for a dual active bridge DC/DC converter is developed. The proposed modulation strategy can avoid the drawbacks of the conventional phase shift modulation and achieve: (1) zero circulating current to reduce conduction loss; (2) soft-switching over the full operating range to reduce switching loss; (3) zero idling power to eliminate idle loss; (4) simple but accurate power flow characterization; and (5) controllable output power between zero and the maximum for different combinations of terminal voltages. Moreover, the proposed modulation strategy enables the converter to achieve the same power density under the same current stress as that of a phase shift modulated converter. Therefore, in comparison with the traditional ones, the proposed strategy is more suitable for energy storage system application.

- The MPC schemes are employed to control the FBC. The MPC schemes can achieve voltage regulation without violating a peak current constraint. Comparative evaluation of LMPC and NLMPC schemes for a FBC is performed. The computation time and closed loop system performances under starting, overload and load step change conditions are compared. The experimental results reveal

that both the LMPC and NLMPC schemes can successfully achieve voltage regulation and peak current protection. Considering the algorithm complexity, the closed loop performance and the necessary computation time, we conclude that the NLMPC scheme is more desirable than the LMPC for this application. To the best knowledge the author, this is the first implicit MPC application reported in open literature for a DC/DC power converter with a millisecond level time constant.

1.3 Dissertation Overview

The dissertation is organized into eight chapters. The first chapter introduces the background, research scope and contributions of this dissertation. The second and third chapters develops tools for the DHPS and IPS of an AES. The fourth and fifth chapters present a novel power flow model and develop a new modulation strategy to improve the power control performance for the FBC. The sixth chapter presents the experimental results that validate the power tracking capability of the DHPS. The seventh chapter develops and compares MPC schemes for the FBC. The final chapter summarizes results and outlines future research work. The remainder of the dissertation is organized as follows:

Chapter 2 develops a testbed for a DC hybrid power system. The major components of this testbed, including the realtime simulation and control rapid prototyping platform, the isolated unidirectional and bidirectional DC/DC converters, the programmable power sources, the programmable electronics loads and the supercapacitor based energy storage bank are introduced.

Chapter 3 introduces a simulation model for the IPS of an AES. Different subsystems of the IPS model are first developed. A LabVIEW based graphic user

interface is then presented. Finally, the simulation results verify that the IPS model can be used to perform simulations for scenarios such as failure emulation, power flow path reconfiguration and energy management.

Chapter 4 presents a novel power flow model for the DABC. The conventional power flow analysis is first introduced. Then, the effects of minor parameters such as the power semiconductor voltage loss and dead time are investigated. Based on the analysis, a new power flow model is then developed. The model can accurately predict the power flow over a wide operating range. The experimental results confirmed the effectiveness of the new model.

Chapter 5 develops a novel current mode PWM strategy for the DABC. The modulation strategy is first introduced. Then, the characteristics of the power converter modulated by the new strategy are analyzed. Finally, the experimental results confirm the superior performance of the dual active converter modulated by the proposed new modulation strategy.

Chapter 6 presents the experimental results that validate the power tracking capability of the DHPS. The power controllers are designed to track the power profile provided by the top level power management algorithm. The experimental results reveal that the designed controllers can track the power profiles quickly and closely.

Chapter 7 develops the MPC schemes for voltage regulation control of the FBC and compares linear and nonlinear MPC schemes. First, the peak current protection constraint is derived. Then, the dynamic model of the FBC is developed, based on which a nonlinear observer is designed for state and parameter estimation. After that, offset-free linear MPC and nonlinear MPC problems are formulated,

followed by an introduction of the InPA-SQP algorithm. Finally, the computation time and closed loop performance of the LMPC and NLMPC are compared through experimental tests.

Chapter 8 presents conclusions and outlines future research plans.

Chapter 2

DC Hybrid Power System Testbed Development

As a large scale complex system, the IPS encompasses power generation, distribution, propulsion and ship service loads. Subsystems involved in IPS range from thermal power plants such as diesel engine or gas turbine, to propulsion motor and power electronic converters that are switching at over kilo-Hz rate. Intricate dynamic interactions among subsystems, in the form of thermal dynamic, electrical, mechanical, and chemical, often dictate the dynamic performance and operational integrity of the overall system. When the system is undergoing transients, managing the inter-connectivity of the power network and leveraging the interactions among diverse power plants/loads become a critical task for the shipboard power management systems. Along with the opportunities ushered in by the IPS systems, the inter-connectivity and complexity of the IPS represent a major system design and optimization challenge, calling for the development of effective analytical frameworks and numerical tools.

This dissertation focuses on the modeling, analysis, and control of a DC Hybrid Power System (DHPS). However, it is unrealistic to build a full scale DHPS in a university setting. Therefore, in order to address the challenges imposed by coordinating

control of multiple power converters of the DHPS, such as the wide range of operating conditions, the requirements for fast power response and load following and the stringent constraints of high system reliability, it is necessary to develop a testbed to facilitate system level analysis, optimization and control. Such a testbed should have: (1) fully digital simulation capability as a preliminary analysis tool to support the modeling and control development effort, (2) adequate hardware resources for controlling a complex dynamic system, (3) necessary hardware, including power sources, power converters and loads, to verify analysis, modeling and evaluation results. Finally, it should have control rapid prototyping capability to ensure quick implementation of advanced control algorithms for system performance evaluation and design validation. In this chapter, a DHPS testbed which has the aforementioned functions will be presented.

2.1 DHPS Testbed Development

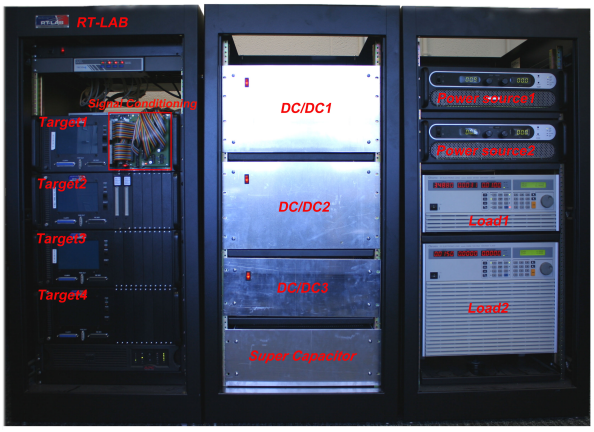

Figure 2.1: DC hybrid power system testbed setup.

Fig.2.1 shows the experimental setup of the DHPS. The entire system is comprised of a real-time simulation and rapid control prototyping platform (RT-LAB® system),

two isolated unidirectional FBCs, a bidirectional DABC, two programmable power sources, two programmable electronic loads and a super-capacitor based energy storage bank. The configuration of the power stage of the DHPS testbed is shown in Fig.2.2 while the major component parameters are shown in Table.2.1.

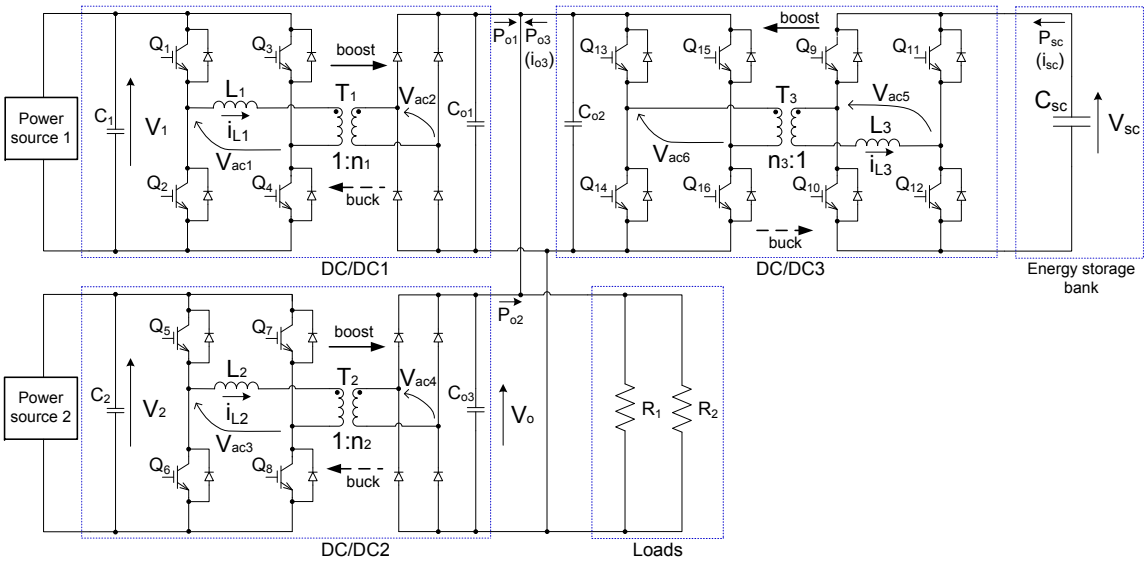

Figure 2.2: Configuration of the power stage of a DHPS with energy storage bank.

Table 2.1: Parameters of the testbed prototype

Item	Parameter
Inductor L_1	$10.4\mu H$
Inductor L_2	$9.8\mu H$
Inductor L_3	$10.8\mu H$
Capacitor C_{o1}, C_{o2}, C_{o3}	$705\mu F$
Energy storage bank C_{SC}	$4F/10.2F/14.2F(75V)$
Transformer turn ratio n_1, n_2, n_3	2
Switching period T	$100\mu s$

The DHPS has multiple power converters which contain many high frequency power switches. These switches are highly nonlinear and time consuming to simulate. Building a simulator for such an electrical system is always a challenge, under the constraints of system cost, required simulation accuracy and desired flexibility.

In contrast with an analog simulator, which achieves real-time simulation by using scaled down analog models of actual components, a digital simulator is becoming popular due to its low maintenance cost and flexibility. Many offline simulation packages including MATLAB/Simulink®, PLECS®, SABER®, etc., can perform offline simulation, but they either can't interact with external hardware or their simulation speed is too slow for large scale system simulation. Real-time digital simulators are a promising approach since they avoid those drawbacks. In comparison with DSP and FPGA based real-time simulators, the PC cluster based simulation system would be a better choice considering the low hardware cost, high simulation performance as well as the flexibility provided by the modular system architecture. RT-LAB® is a PC-cluster based expandable real-time simulator which is compatible with Matlab/Simulink®, thereby allowing effective leverage of commercially available MATLAB/Simulink® toolsets, such as control system design and analysis toolboxes,code generation toolboxes, and Physical Modeling toolboxes. Specialized tools such as ARTEMIS® and RT-Events® support multi-rate fixed-time-step real-time simulation of power systems with dramatically improved computation speed and accuracy [7].

Fig.2.3 shows the configuration of the real-time simulation platform while its hardware is shown in Fig.2.1 (left rack). This system has 8 CPUs allocated in 4 physically separated targets. The CPUs in the same target exchange information through the shared memory while the different targets communicate through infiniband switch with 10Gb/s speed. There are three host PCs which can talk with each target via 1Gb/s Ethernet switch. The targets can interact with the external hardware through 32bits PCI Bus I/O interfaces. Combining the FPGA event detection with specialized real-time interpolation algorithms toolbox RT-Events®, the effective precision of the I/O could be better than 1μs. The I/O interface provides a platform for data

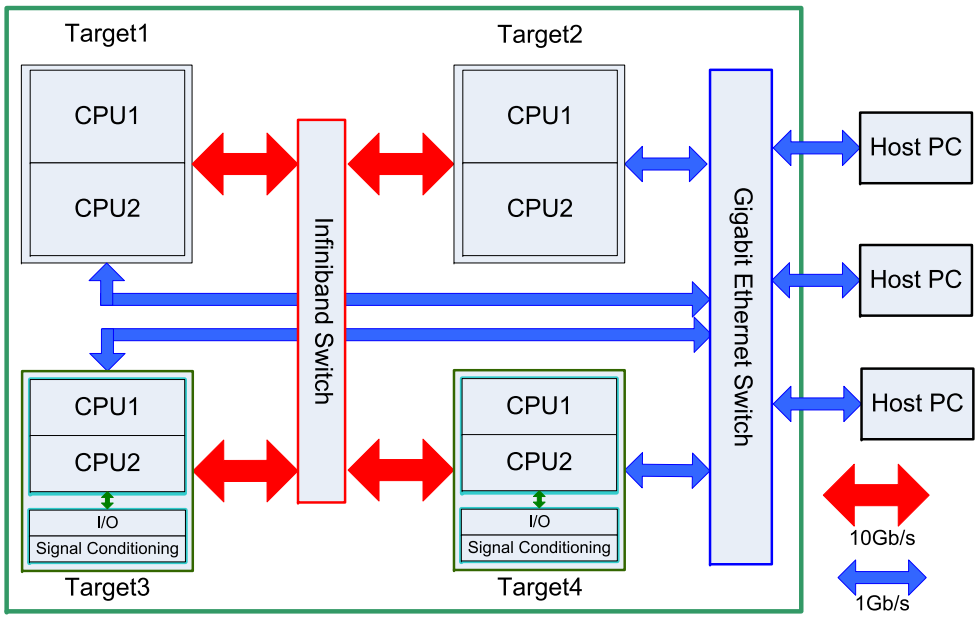

Figure 2.3: RT-Lab real-time simulation system configuration.

acquisition and signal conditioning modules that enable the implementation of high frequency analog/digital I/O, event capture, and event generation. All of the targets and CPUs are synchronized either by software or by hardware. Thus all of the CPUs can synchronously interact with the analog and digital I/O. This feature makes it possible for the system to implement physical components for hardware-in-the-loop simulation or to perform control prototyping experiments. In addition, the synchronized targets can run real-time simulations at different time steps, making it very flexible to distribute the complex model to different targets or CPUs within the simulation platform. This real-time simulator also can interact with other stand alone RT-Lab targets through Ethernet. For our testbed, the RT-LAB® system serves the following three functions: (1) as a real-time simulator to simulate power source models and to control programmable power supplies to emulate the characteristics of a specified power source; (2) as an embedded controller for which the C code generated in a host PC can be downloaded and executed in target CPUs to control power con-

verters; (3) as a data acquisition device to sample and store experimental data for feedback control and detailed offline analysis.

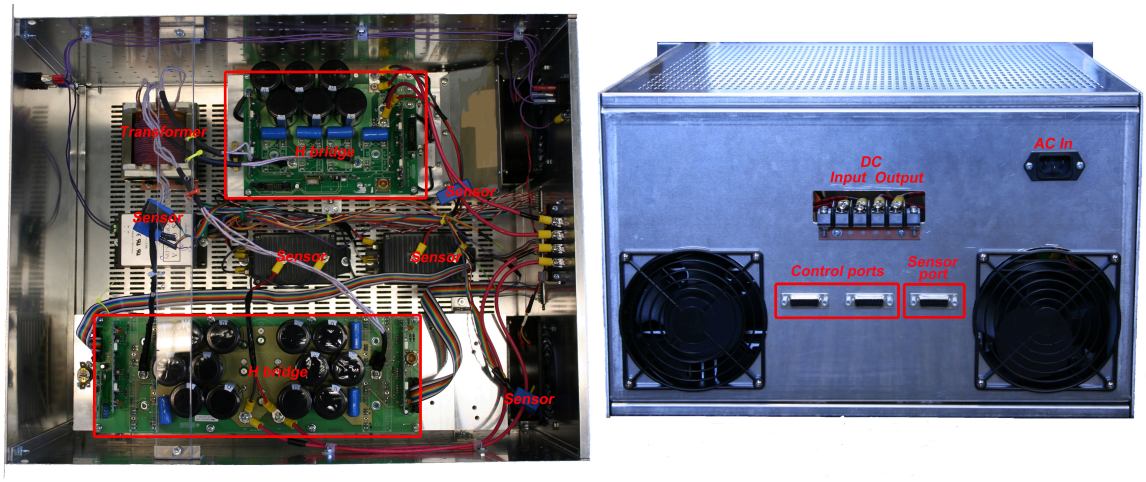

Figure 2.4: Bidirectional DC/DC converter.

The two programmable power supplies are the Sorensen® SGA 100A/100V 10KW AC/DC power supply. The output voltage of the programmable power supplies can be controlled through an analog signal. Therefore, one can use RT-LAB® target to simulate a power source model and then to control the power supplies through the RT-LAB® target analog interface so that the power supplies emulate the characteristics of DC power sources. The two programmable electronics loads are Chroma® 63202 5A/50A 125V/500V 2.6KW DC load and Chroma® 63204 10A/100A 125V/500V 5.2KW DC load, respectively. Similarly, the two DC electronic loads can also be controlled by RT-LAB® targets to emulate different types of loads.

The two unidirectional DC/DC converters (marked as DC/DC1 and DC/DC2 respectively in Fig.2.2) are the FBCs while the bidirectional DC/DC converter (marked as DC/DC3 in Fig.2.2) shown in Fig.4.3 is the DABC. The FBC and DABC were initially proposed in previous studies [54], [55] for both high power density and high power applications. They are very attractive because of their zero voltage switching, low component stresses, and high power density features. Moreover, their high fre-

quency transformer prevents fault propagation and enables a flexible output/input voltage ratio. Therefore, with a FBC or a DABC as the power conditioning system, the low voltage high current power source such as the fuel cell power system and energy storage device can be applied to high DC voltage applications, such as the DC zonal electrical distribution system of an all electric ship [93].

The energy storage bank is composed of two branches of super-capacitors. One branch includes five BOOSTCAP® BPAK0020-15V modules which are connected in series and offer total $4F$ capacitance. The other branch has five BOOSTCAP® BPAK0052-15V modules, therefore it provides $10.2F$ capacitance. Both the two branches have a $75V$ working voltage. Moreover, they can be connected in parallel to provide $14.2F$ capacitance. Therefore, the energy storage bank can be reconfigured for different applications.

While the RT-LAB system enables the control rapid prototyping of the DHPS which has multiple power converters, its multi-target multi-rate structure facilitates realtime simulation of a large scale system, such as the IPS of an AES. In parallel with hardware construction, a modularized simulation model of an IPS is developed and will be introduced in Chapter 3.

2.2 Summary

In this Chapter, a DHPS testbed is introduced. The testbed is built at the University of Michigan and has all of the necessary functions specified in the first paragraph of this chapter, thereby facilitating optimization and power management strategy development for the DHPS. Leveraging the realtime simulation capability of the testbed, a modularized simulation model for an IPS of an AES is developed and the realtime simulation results will be presented in the next chapter.

Chapter 3

Modeling and Simulation of an Integrated Power System for an All Electric Ship

In this chapter, a modularized model for an Integrated Power System (IPS) of an All Electric Ship (AES) is developed. All major subsystems of the model are first introduced. Then, the model integration and distribution method is presented. Finally, the graphical user interface is demonstrated, followed by the simulation results for scenarios such as failure emulation, power flow path reconfiguration and energy management.

3.1 Modeling of IPS

Since the IPS is a large scale power system containing many high frequency power switches or other components whose simulation is very resource demanding, it is time consuming to simulate and debug such a large system offline. On the other hand, parameter tuning of this complex system as a whole is a daunting, if not impossible, task. Furthermore, many of the subsystems in Zonal Electrical Distribution System (ZEDS) are similar and can be reused. Therefore, our effort is focused on developing

a modularized IPS model for AES application. We split the whole IPS into three subsystems, namely the Power Generation Module (PGM) including a gas turbine and fuel cell power system, Electric Propulsion Module (EPM), and ZEDS. ZEDS, by itself, consists of many power conversion modules and electric loads.

3.1.1 Gas Turbine Module

While many different types of power systems are used for shipboard applications, gas turbine/generator sets are quite often used as the shipboard prime mover. A combination of first principles and empirical relationships have been used for the gas turbine model development [102]. The schematic of the gas turbine model developed for the ship-board power system is shown in Fig. 3.1.

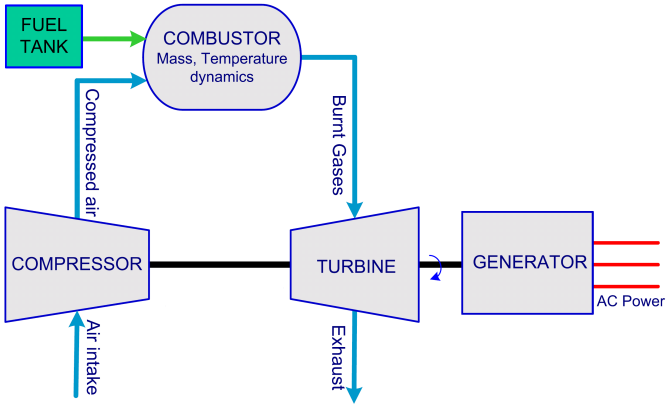

Figure 3.1: Schematic of the gas turbine/generator system.

The gas turbine model captures the dynamic characteristics of compressor, turbine, combustor and the coupling between turbine and compressor. The combustor mass and temperature dynamics along with turbocharger rotational dynamics are considered, while the compressor and turbine air mass flows and efficiencies are modeled as empirical relations. The input to the gas turbine is assumed to be $JP5$ fuel flow injected into combustor, and the torque input on the turbocharger shaft, reflect-

ing the power demand, is the disturbance to the turbine operation. The variables and parameters used in GT model are defined in Table 3.1. The following standard [102] assumptions have been made for the gas turbine model.

- The heat loss in the compressor is negligible.
- Compression and expansion process are adiabatic.
- Fuel injector dynamics are faster as compared to the burner temperature and mass dynamics and are neglected.
- Perfect combustion occurs inside the burner.
- The generator is modeled as an efficiency transfer function from mechanical power input to electrical power output.

Under these assumptions, the equations representing the dynamics can be derived using first principles, such as energy, mass and power balance and curve fitting as follows:

Compressor and Turbine

The compressor and turbine mass flow and the isentropic efficiency (*Appendix A*) are obtained by curve fitting the performance maps scaled from an automotive application [103] using the techniques suggested in [104], [105]. They are functions of pressure ratio ($\frac{p_b}{p_{amb}}$), combustor temperature (T_b) and the turbocharger speed (ω_{tc})

The compressor power is determined using the first law of thermodynamics and is given by

$$P_c = W_c c_p (T_{c,out} - T_{amb}), \tag{3.1}$$

Table 3.1: GT Modeling Nomenclature

Variable	Description (Unit)
$c_{p,air}$, $c_{p,f}$, $c_{p,gas}$	Specific heat at constant pressure of air, fuel and burnt gas (kJ/kg K).
$c_{v,b}$	Constant volume specific heat for burner material (kJ/kg K).
J_I	Gas turbine rotor, shaft, generator rotor inertia (kgm^2)
m_b	Mass inside burner (kg),
$M_{b,in}$	Molecular mass of air-fuel mixture inside burner (kg/mole)
p_{amb}, p_b	Ambient and combustor pressure (Pa)
P_c, P_t	Compressor and turbine power (kw)
Q_{LHV}	$JP5$ lower heating value (kJ/kg)
R	Universal gas constant (kJ/K mol),
T_{amb}, T_{ref}, $T_{c,out}$, $T_{t,out}$, T_b	Ambient, reference, compressor outlet, turbine outlet, combustor temperature (K)
V_b	Burner volume (m^3)
W_f, W_t, W_c	Fuel flow, compressor, turbine air flow (kg/s)
τ_{dem}, ω_{tc}	Load torque (N-m), Shaft rotational speed (rad/s)
γ	Specific heat ratio
η_m	Turbine mechanical efficiency (%)
$\eta_{is,c}$, $\eta_{is,t}$	Compressor and turbine isentropic efficiency (%)

where the compressor exit temperature $T_{c,out}$ is given as

$$T_{c,out} = T_{amb}\left[1 + \frac{1}{\eta_{is,c}}\left(\left(\frac{p_b}{p_{amb}}\right)^{\frac{\gamma-1}{\gamma}} - 1\right)\right]. \tag{3.2}$$

Similarly the turbine power is given by

$$P_t = W_t c_p (T_b - T_{t,out}), \tag{3.3}$$

where

$$T_{t,out} = T_b\left[1 - \eta_{is,t}\left(1 - \left(\frac{p_{amb}}{p_b}\right)^{\frac{\gamma-1}{\gamma}}\right)\right]. \tag{3.4}$$

Combustor

The burner mass is determined using the mass balance and is given by

$$\dot{m}_b = W_f + W_c - W_t \tag{3.5}$$

and the temperature is determined using energy balance as

$$\begin{aligned}\dot{T}_b = \frac{1}{m_b c_{v,b}} \big((W_c c_{p,air} + W_f c_{p,f})(T_{c,out} - T_{ref}) \\ + W_f Q_{LHV} - W_t c_{p,gas}(T_b - T_{ref})) - \\ c_{v,b}(T_b - T_{ref})\dot{m}_b\big)\,.\end{aligned} \tag{3.6}$$

The burner pressure p_b is derived using the ideal gas law:

$$p_b = \frac{m_b}{M_{b,in} V_b}(RT_b). \tag{3.7}$$

Output Shaft Speed

The shaft speed is determined using the power balance on the shaft given by

$$\dot{\omega}_{tc} = \frac{1}{J_I}\left(\frac{\eta_m P_t - P_c}{\omega_{tc}} - \tau_{dem}\right). \tag{3.8}$$

The gas turbine drives the power generation device which converts mechanical power to electrical power and generates three-phase AC power with $4160V$ line to line voltage and 60Hz frequency. For the particular system modeled in this platform, the total power output is between 255 KW to 1.4 MW. The open loop simulations for step changes in power demand are shown in Fig. 3.2 and the gas turbine has a rapid response that can be captured by a second order dynamical system.

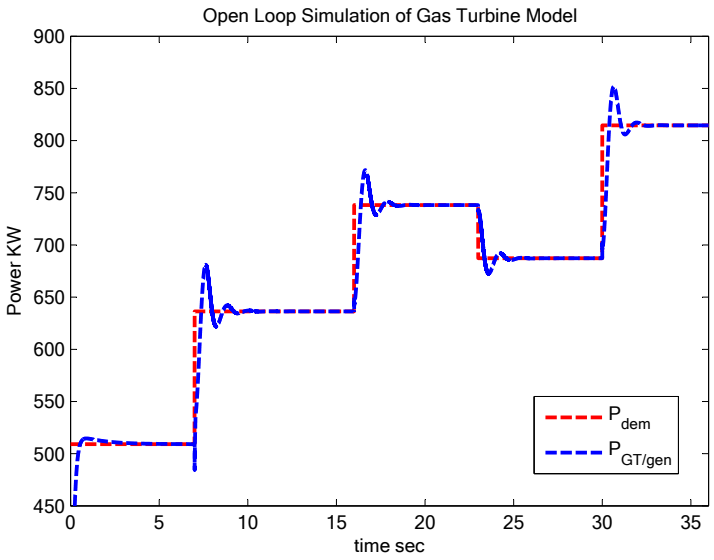

Figure 3.2: Open loop simulations of gas turbine: demand Vs. generated power.

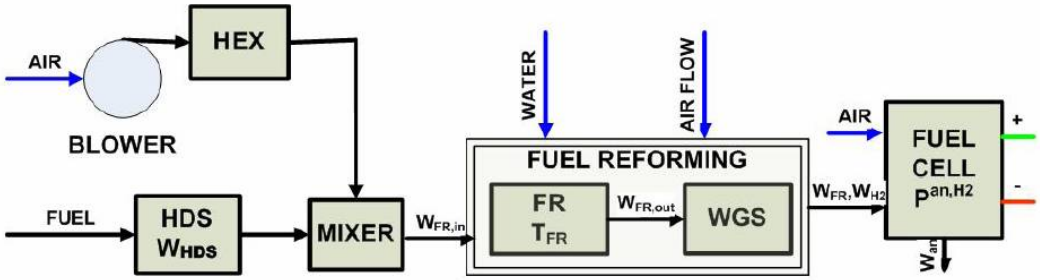

Figure 3.3: Schematic of fuel processing system

3.1.2 Fuel Cell and Reforming Unit Module

The Fuel Cell (FC), which is clean and highly efficient, is considered as an auxiliary power source for the IPS. We consider a Polymer Electrolyte Membrane (PEM) fuel cell along with a fuel processing system (FPS). The FPS+FC (Figure 3.3) system consists of a hydro desulphurizer (HDS), heat exchanger (HEX), mixer (MIXER), fuel reformer (FR), water gas shift reactor (WGS) and fuel cell anode dynamics. A detailed 10 state model of the FPS+FC system has been developed in [106]. The effort here was to develop a reduced order model that still captures the system dynamics

as well as operating constraints such as fuel starvation. Based on the linear analysis of the 10 state model around different operating points, we found that the dominant modes corresponded to the FR temperature, HDS and the anode hydrogen partial pressure. Therefore our reduced order model has three states. The inputs to the FPS+FC are fuel and air flow, while the stack current is considered as a disturbance. The variables and parameters used in FC model are defined in Table 3.2. The following assumptions were made for the simplified FC+FPS model.

- Due to the relatively large volume of the reformer, we assume that the dynamics associated with the fuel path are slower than those with the air path. Consequently, the cathode dynamics are neglected.
- WGS reactions are fast and perfectly controlled and hence the dynamics are neglected.
- The temperature inside the fuel cell is assumed to be controlled to remain constant.

Since the stack current (I_{st}) is measured, the fuel and air flow are determined by a static feedforward map to control the steady state fuel utilization (U_{H_2}) to 0.8 as given in [106].

Hydro Desulphurizer

The HDS is represented as a large volume and is simplified as a first order lag with a slow time constant ($\tau_{HDS} = 5sec$) that reflects the slow dynamics of the linearized model given in [106]. The other two states representing slow dynamics in [106] are the FR temperature and the anode hydrogen partial pressure.

Table 3.2: FC Modeling Nomenclature

Variable	Description (Unit)
$c_{p,FR}$	Ratio of constant specific heat of FR material (kJ/kg K)
E	Open circuit fuel cell voltage
h_{in}, h_{out}	Specific enthalpy (J/kg) of inlet and outlet FR flows
m_{FR},	Mass inside the reformer unit (kg)
M_{an}, M_{H_2}	Molecular mass of anode material and hydrogen(kg/mol)
n_c	Number of fuel cells in the stack
N_{in}, N_{out}	Molar flow rates in and out of the FR (mol/s)
p_{an},$p_{H_2,an}$	Anode total and hydrogen partial pressure (Pa)
R	Universal gas constant (J/K mol)
T_{FR}, T_{an}	FR and anode temperature (K)
v_{ohm}, v_{act}, v_{conc}	Ohmic, activation and concentration loss respectively (volt)
V_{an}	Anode volume (m^3)
$W_{FR,in}$ W_{FR,H_2}, $W_{FR,out}$	Total flow into the FR (kg/s) Hydrogen and total flow out of FR (kg/s)
$W_{H_2,react}$	Reacted hydrogen inside anode (kg/s)
$W_{H_2,an}$, W_{an}	Hydrogen and total anode exit flow (kg/s)

Fuel Reformer

The FR model is developed in [106] and is summarized here. The temperature dynamics using energy balance is given by

$$\frac{dT_{FR}}{dt} = \frac{1}{m_{FR}c_{p,FR}}\left[N_{in}h_{in} - N_{out}h_{out}\right] \tag{3.9}$$

where the inlet flow consists of the fuel and air flow and the outlet flow includes the following species: CH_4, CO, CO_2, H_2, H_2O, N_2.

Anode

The anode partial pressure dynamic using mass balance is given by

$$\frac{dp_{H_2,an}}{dt} = \frac{RT_{an}}{M_{H_2}V_{an}}(W_{FR,H_2} - \chi^{an}_{H_2}W_{an} - W_{H_2,react}),$$
$$\chi^{an}_{H_2} = \left(\frac{M_{H_2}}{M_{an}}\right)\left(\frac{p_{H_2,an}}{p_{an}}\right), \tag{3.10}$$

where W_{FR,H_2} is the hydrogen flow from the reformer, W_{an}, $W_{H_2,react}$ are the anode outlet flow and reacted hydrogen. The anode outlet flow is given by the orifice equation as,

$$W_{an} = W_{0,an}\sqrt{\frac{p_{an} - p_{amb}}{\Delta p_0}},$$

where Δp_0 is the pressure drop across the orifice with $\Delta p_0 = 600Pa$ as given in [106]. The hydrogen consumed is given by the electrochemistry principle as follows:

$$W_{H_2,react} = M_{H_2}\frac{ncI_{st}}{2F}.$$

where n is the number of cells (1000) and F is Faraday constant. The air supply is assumed to be instantaneous and the cathode pressure follows the anode pressure.

Stack Voltage Model

The stack voltage is a function of the fuel cell temperature and pressure and is given by $v_{st} = n_c(E - v_{act} - v_{ohm} - v_{conc})$ and further details of this model can be obtained from [106].

The output of the FC system is connected to the DC-Link in PCM4 through a DC/DC converter. For the particular system modeled, the total power output of the

FC-FPS is between 80 KW and 330 KW.

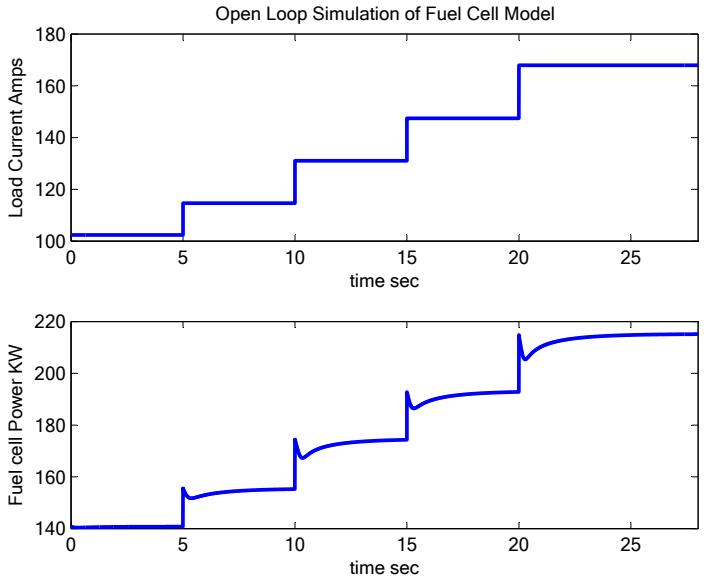

Figure 3.4: Open loop simulations of fuel cell: current demand and generated power.

The open loop simulations for step changes in fuel cell load current are shown in Figure 3.4. It can be seen that the fuel cell has a slower response, compared to that of the gas turbine/generator set. The hydrogen starvation in the fuel cell due to the slow reformer dynamics is reflected in the instantaneous increase followed by a dip in the power output.

3.1.3 ZEDS Module

Fig.1.1 in Chapter 1 shows the diagram of a two-zone IPS which has PGM, EPM, ESM and ZEDS. Since DC zonal architecture has many advantages over AC zonal architecture [4] for shipboard application, DC ZEDS was targeted in our modeling effort. The key components of DC ZEDS are vital/non-vital loads and power conversion modules. The models for individual components are discussed briefly in the sequel.

Power Conversion Module1 (PCM1)

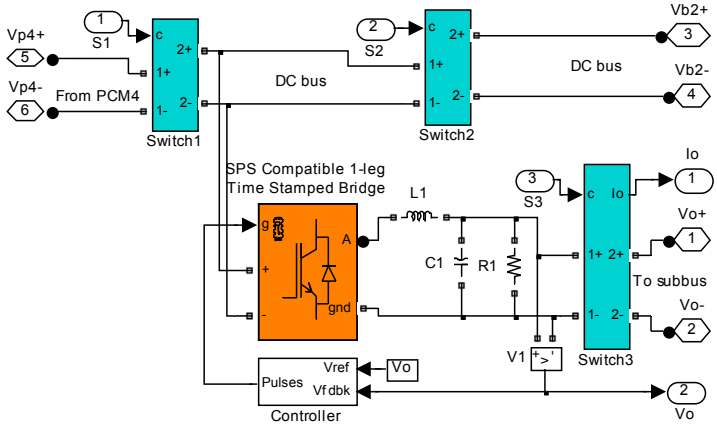

Figure 3.5: SimPowerSystems/ARTEMIS model of PCM1 in ZEDS.

Fig.3.5 shows the model of PCM1. PCM1 is a step down DC/DC converter with three reconfigurable switchboards. The step down DC/DC converter is modeled with the 1-leg Time-Stamped Bridge of the ARTEMIS® toolbox while other components are modeled with SimPowerSystems® toolbox. Manipulating the three switchboards can reconfigure the power flow path of each electric zone. DC bus failure and recovery emulation also can be achieved by the manipulation of switchboards. The output voltage of PCM1 is 900VDC which is 200V less than the main bus. The loads of PCM1 are one nonvital load and one vital load under normal situations. One vital load will be added if the opposite main bus or PCM4/PCM1 is down because of either equipment failure or battle damage.

PCM2/5 (DC/AC inverter for vital load)

Fig.3.6a shows the diagram of PCM2/5. PCM2/5 is a DC/AC inverter which is modeled with SimPowerSystems® Compatible 3-leg Time-Stamped Bridge of the ARTEMIS® toolbox. Since they energize the vital load which shouldn't lose power

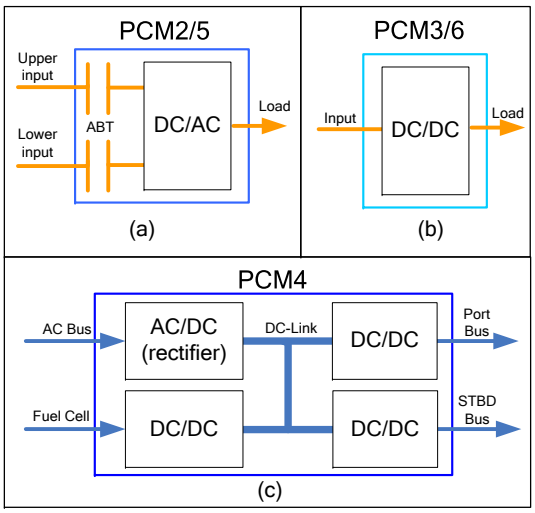

Figure 3.6: Diagram of PCMs in ZEDS.

by any chance, there is an Auto Bus Transfer (ABT) circuit which can automatically select power input port between the upper input and lower input. Usually the upper input has higher priority than the lower one and will be dropped only when its voltage decreases to 100V lower than the lower input. However, to balance load for the two DC buses, the upper input will take over again if its voltage is recovered to 50V higher than the lower input.

PCM3/6 (DC/DC converter for non-vital load)

Fig.3.6b shows the diagram of PCM3/6 which also is DC/DC converter. In comparison with PCM1, PCM3/6 doesn't have switchboards for load redirection. PCM3/6 is modeled with the 1-leg Time-Stamped Bridge of the ARTEMIS® toolbox too. There is no ABT in PCM3/6 given the nonvital nature of the loads connected to it. The nonvital load will directly lose its power if the main bus or sub-bus on its side is down.

PCM4

Fig.3.6c is the diagram of PCM4 which conventionally is an AC/DC converter converting three-phase AC power to DC power by controlling the rectifier firing angle. For our model, PCM4 has hybrid power sources, AC main bus and fuel cell, the output of AC/DC was connected with output of the DC/DC converter of fuel cell model through DC-Link. The proportion of power drawn from AC bus and fuel cell respectively can be dynamically managed by splitting the desired current to the two input converters. To get well regulated DC voltage on the port bus and starboard bus, there are starboard side and port side output DC/DC converters drawing power from DC-Link and regulating the voltage on the two DC buses to 1100VDC. The modeling of the two output DC/DC converters is similar to the DC/DC converter in PCM1, the buck converter topology is adopted and modeled with SimPowerSystems® compatible 1-leg Time-Stamped Bridge of the ARTEMIS® toolbox. Both of the output converters are regulated by their dedicated PI controller.

Loads

Vital/nonvital loads were modeled as constant power loads. All of the loads can draw a certain amount of power from the DC bus according to commands from the energy management module. More detailed load models such as those for DC motor or AC motor also could be modeled and integrated in the future.

3.1.4 Propulsion Module

Electric Propulsion System Model

The electric propulsion system model is a three-phase AC/DC/AC variable speed transmission system with the low speed, high torque Permanent Magnet Synchronous

Motor (PMSM) driving the propeller. The AC/DC rectifier is modeled with SimPowerSystems® toolbox Universal Bridge. There is also a braking chopper on the DC-Link to absorb the regenerated energy by the motor at the crash stop situation. The DC/AC inverter which works as the frequency converter and drives the propulsion PMSM is modeled with Time-Stamped Bridge of the ARTEMIS toolbox and controlled by a close loop speed controller. Other than the three-phase AC/DC/AC propulsion system, other AC propulsion technologies such as cyclo-convertor [10], matrix converter [14] and high temperature superconductor (HTS) motor [15] also can be modeled and integrated into the propulsion module in the future.

Ship Dynamic Model

The load torque to the eletric propulsion motor is determined by the ship dynamic model, which calculates the ship speed and propeller speed according to hydrodynamics. The ship model given in [16] is adapted. It includes the added mass and hydrodynamic forces and moments acting on the ship. Given a desired ship speed, the desired motor speed and torque are calculated in this module and fed to the propulsion motor control unit.

3.2 Model Integration, Distribution and Preliminary Simulation

3.2.1 Model Integration and Distribution

There are two stages for the IPS model integration. First of all, the ZEDS module and propulsion module are integrated and tested respectively. As we discussed in the previous sections, the key components of ZEDS, loads and PCMs, are separately

developed and tested. After that, all of the PCMs and loads are interconnected to form the two zones of the ZEDS. The integration of ship dynamic model and propulsion model is quite straightforward too. The desired propeller torque and speed signals which are calculated by ship dynamic model are sent to the motor in the propulsion model. Then ZEDS and propulsion modules are connected with the power generation module.

The IPS is a large scale system which has many subsystems with different characteristics. For example, the dynamics of G/T and FC are relatively slow, and sampling at 1ms time step is sufficient. On the other hand, PCMs have high frequency power switches, the subsystem time step is 50μs in our case which is much shorter than PGMs'. To get a relatively balanced computation task distribution among all CPUs for better simulation performance, one has to distribute the model properly into the 8-CPU simulator. There are several considerations that need to be taken into account in allocating resources: (1) The subsystems assigned to each CPU should assume that no overruns will result, otherwise simulation performance will be compromised; (2) Since real-time communication between targets is a resource demanding process, it is advantageous to assign a modularized subsystem as one entity to one CPU instead of splitting the subsystem into several parts to reduce the number of signals to be exchanged between targets; (3) Each CPU can run real-time simulation with one sampling rate, subsystems with slow sampling speed can be grouped with the subsystem with fast sampling speed. Given these constraints, we assign one CPU for subsystems PGM(Gas Turbine), PGM(Fuel Cell) and EPM while splitting the ZEDS into two subsystems with two associated CPUs.

Another challenge for model distribution is that all of the distributed subsystems exchange information through the RT-LAB block-OpComm, which is only compatible with arrowlines. Arrowline indicates the unidirectional signal flow and is

the default connection for Simulink® as well as many Simulink® compatible toolbox blocks. However, the power conversion and propulsion subsystems developed with SimPowerSystems® toolbox use stublines by default. The stubline passes signals bidirectionally just as a physical wire would do. The incompatibility between SimPowerSystems® sub models and OpComm blocks is resolved by DC and AC bus models which convert the signals flow on the stubline into signals flow on the arrowline. These bus models are incorporated to appropriate locations where it is necessary to split the model and assign different CPUs to the subsystems.

Based on the integrated model, simulations were performed which will be discussed in the following subsection.

3.2.2 Preliminary Simulations

To validate the IPS model of an AES, realtime simulation was performed on the RT-LAB system. The IPS has a main power generation system, namely a gas turbine generator set, which can deliver power up to 1.4MW. The auxiliary power generation system is a fuel cell power system which can provide up to 330KW power for the ship service loads. The rated power of the electrical propulsion system is 1.3MW which can drive the model ship with a ten-knot speed. The goals of the simulations are to validate the transient response, failure emulation and power flow path reconfiguration capability of the IPS model.

Fig.3.7 shows power consumed by loads during a failure and reconfiguration process where four scenarios are represented. Scenario 1: the port bus or local PCM1/PCM4 is down, the non vital load loses its power while the vital load draws power from the STBD bus. Scenario 2: the port bus is reconfigured or the PCM1/PCM4 is recovered, all loads draw equally 40KW power from both buses. Scenario 3: the STBD bus is down which leads to the STBD side nonvital load losing its power. The vital load

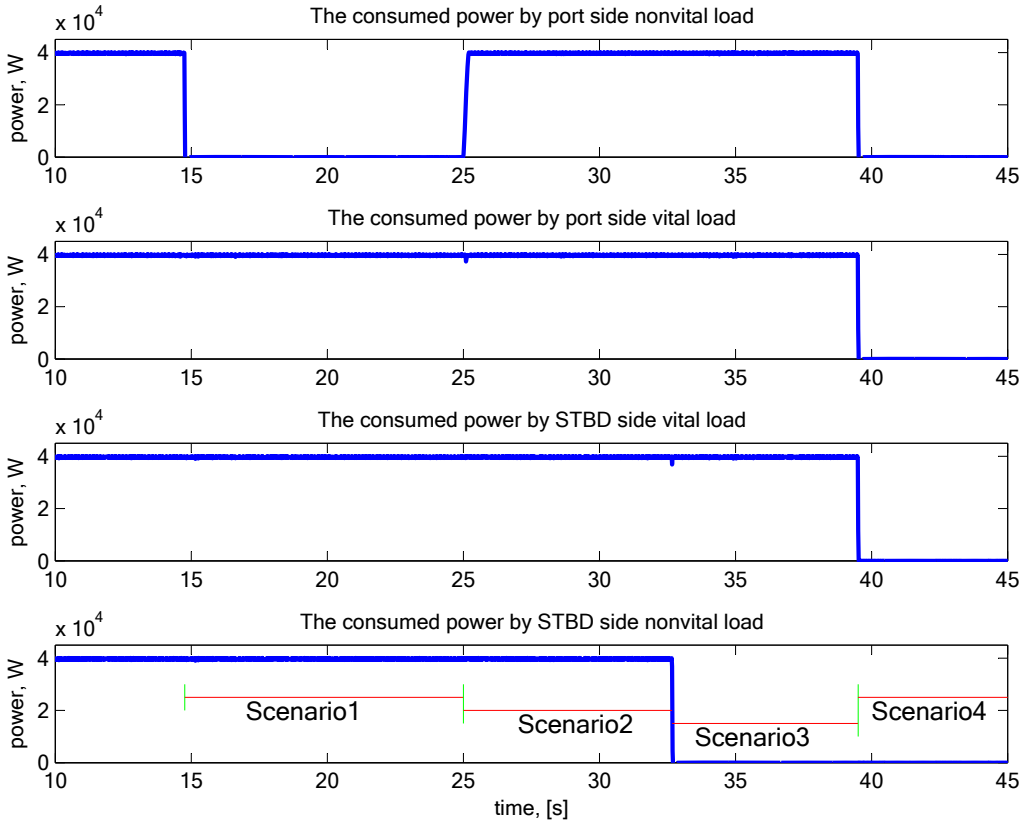

Figure 3.7: Power consumed by loads at failure and reconfiguration scenarios.

works fine since it is switched to draw power from the port bus. Scenario 4: both buses are down, consequently all of the loads lose their power. This testing verified the failure emulation and reconfiguration capability of the ZEDS model, which is critical to enable the algorithm development of intelligent reconfiguration of ZEDS in the future.

Fig.3.8 shows the transient response of the propulsion motor when the ship speed is accelerated from 0 knot to 8 knots. To accelerate the propeller speed, the actual torque is significantly larger than the desired torque during the starting up period. Both the actual torque and speed curves match with the desired curves very well after that, which confirms that the propulsion model captures the ship dynamic model as

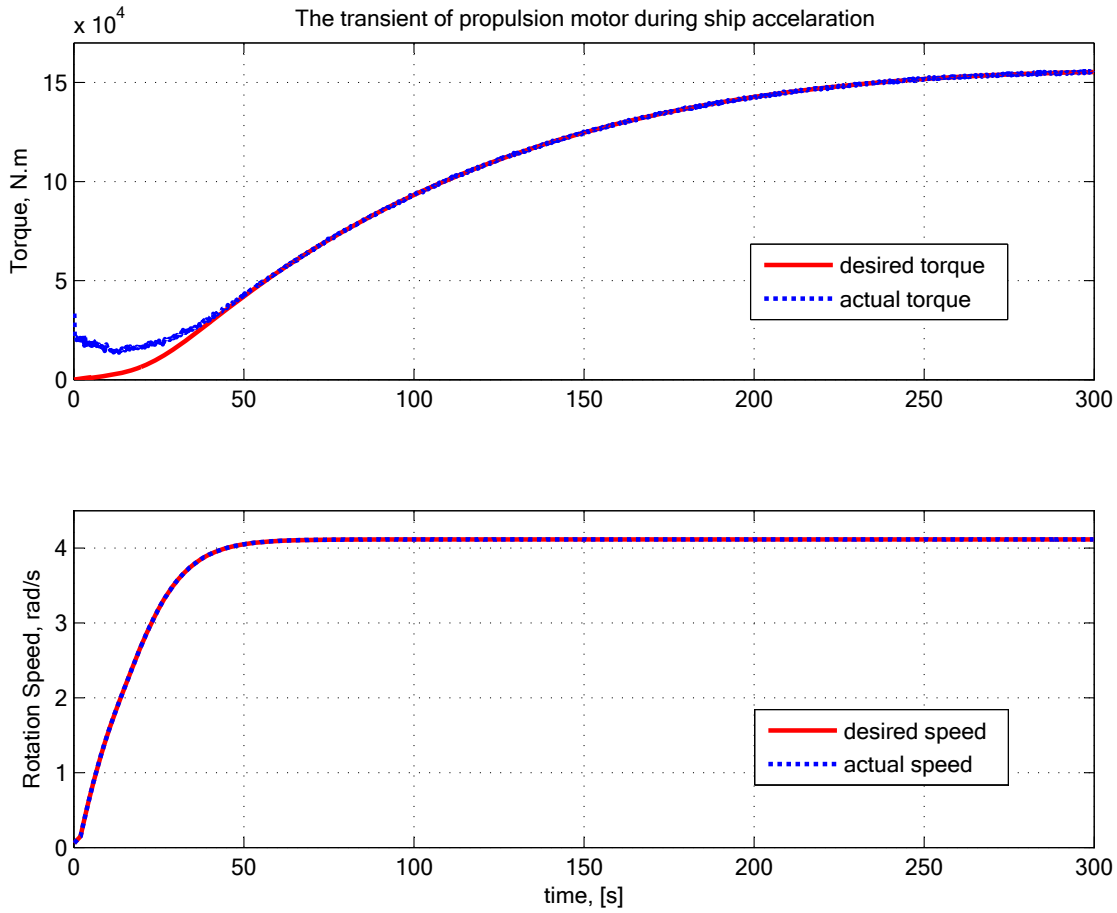

Figure 3.8: Propulsion motor transient.

required.

3.3 Graphical User Interface (GUI) Development

Since the system is very complicated and many signals have to be sent to the console on the host PC, a single window console is too busy to be used to monitor the signals during the simulation. On the other hand, we have to interact with the model during realtime simulation to operate the reconfigurable switches in the PCM1. So a GUI is necessary to create an engineering environment where one can monitor and manipulate the simulation.

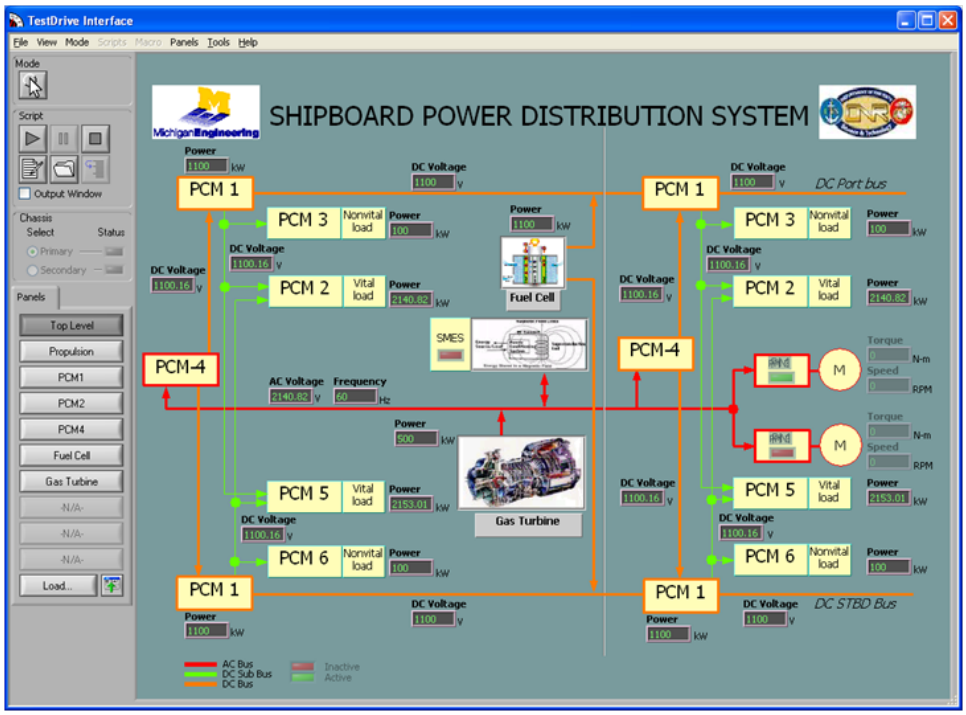

Figure 3.9: The top level GUI of the IPS.

We developed the GUI based on Testdrive® V2.1.3 which is compatible with both MATLAB/Simulink® and LabVIEW®. The GUI has a multi-level structure. The top level GUI is shown in Fig.3.9 and is similar to the structure shown in Fig.1.1, where the displayed signals can be used to indicate the health and status of the system. We are also able to navigate to each of the sub-level GUIs for different subsystems by clicking on their respective buttons. In the sub-level GUI, data acquisition and control signals of the subsystem are displayed.

As an example, the Failure, Reconfiguration, Operation and Drive Scenarios, a sub-level GUI for power management, is given in Fig.3.10. The Failure, Reconfiguration, Operation and Drive Scenarios GUI is the one which can set the ship speed, emulate PCM or DC bus failure and reconfigure the power flow path. The buttons on the GUI, corresponding to Switch1, Switch2 and Switch3 of PCM1 in Fig.3.5, can be pushed on or off to emulate bus crashing or to redirect the power flow. Numeric

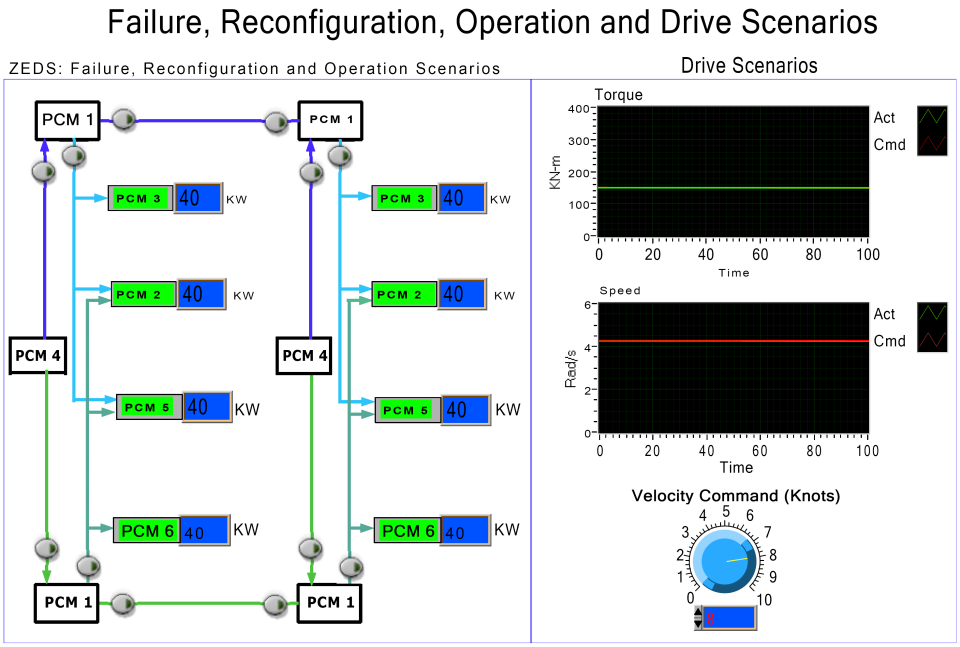

Figure 3.10: Failure, reconfiguration, operation and drive scenarios GUI.

boxes next to the PCMs allow manual inputs to change the loads associated with corresponding PCMs. The ship velocity command knob controls ship speed. The two waveform charts display the desired and actual speed and torque for the propeller.

3.4 Summary

In this chapter, a simulation model for the IPS of an AES is developed. The model integration and distribution strategy on a multi-rate multi-node realtime simulation platform is discussed. The LabVIEW based graphic user interface is introduced. The preliminary simulation results verify that the IPS model can perform simulations for scenarios such as failure emulation, power flow path reconfiguration and energy management.

As discussed in this chapter, the IPS of an AES has a gas turbine, a fuel cell power system, two electric propulsion systems, and a Zonal Electrical Distribution System

(ZEDS) which, by itself, has many power conversion modules and loads. Both the gas turbine/generator and the fuel cell power system energize the ZEDS DC bus, forming an isolated DC Hybrid Power System (DHPS) which has multiple FBCs and a DABC as the power conditioning devices. However, for the isolated hybrid power system, the wide range of operating conditions, the requirements for fast power response and load following, coupled with the stringent constraints of high power quality and system reliability, have imposed challenges for control of the power converters whose dynamic characteristics are highly nonlinear. Motivated by the challenges and importance of the DC Hybrid Power System (DHPS) control, analysis, modeling and control of power converters for the DHPS will be presented in the following several sections.

Chapter 4

Power Flow Characterization of the Dual Active Bridge Converter

The Dual Active Bridge Converter (DABC) is a bidirectional DC/DC converter which is used to charge and discharge the energy storage bank of the DHPS. In this chapter, we will illustrate that the power flow model of a DABC given by [54, 55], albeit simple, can not be used for effective power flow control design. Therefore, a novel power flow model for the DABC is developed. The fundamental phenomena are first introduced. After that, the conventional power flow analysis is introduced. Then, the effects of minor parameter such as the power semiconductor voltage loss and dead time are investigated. Based on the analysis, a new power flow model is then developed. The model can accurately predict the power flow over a wide operating range. The experimental results confirmed the effectiveness of the new model.

4.1 Fundamental Phenomena of DABCs

Fig.4.1 shows the configuration of the DABC, where $Q_9 - Q_{16}$ are the power switches, L_3 is the leakage inductor of the transformer with turn ratio n_3, and C_{sc} and

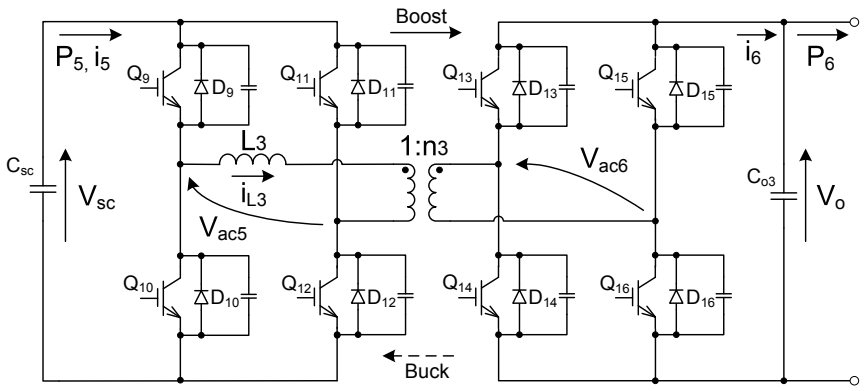

Figure 4.1: Dual active bridge DC/DC converter topology.

C_{o3} are the capacitors connected to the DC side of each bridge. The AC side of each bridge is connected to the transformer with corresponding primary voltage V_{ac5} and secondary voltage V_{ac6}, respectively. If we ignore the power semiconductors' voltage loss, V_{ac5} could equal V_{sc}, $-V_{sc}$ or 0 while V_{ac6} could equal to V_o, $-V_o$ or 0, depending on the DAB's operating mode, where V_{sc} and V_o are the voltages across the capacitors C_{sc} and C_{o3}, respectively. Unlike many bidirectional isolated DC/DC converters with asymmetrical topology [56–62], the DAB converter has two symmetrical full bridges. The DABC is typically modulated by the phase shift modulation strategy shown in Fig.4.2(a). Note that β_3 is the normalized phase shift between the two full bridges. It serves as the control input for manipulating the DAB converter, where $\beta_3 \in [0, 1]$ for the boost direction and $\beta_3 \in [-1, 0]$ for the buck direction. Note that since the parallel resistance and inductance are much greater than the series resistance and inductance, the equivalent circuit model of a high frequency transformer can be simplified as an ideal transformer with primary series inductor (leakage inductor). Therefore, the electrical connection between V_{ac5} and V_{ac6} shown in Fig.4.1 can be expressed by the diagram shown in Fig.4.3, where L_3 is the leakage inductance. By shifting the phase between the two full bridges, different combinations of V_{ac5} and V_{ac6} can be applied to shape the current i_{L3} and consequently to manipulate the direction

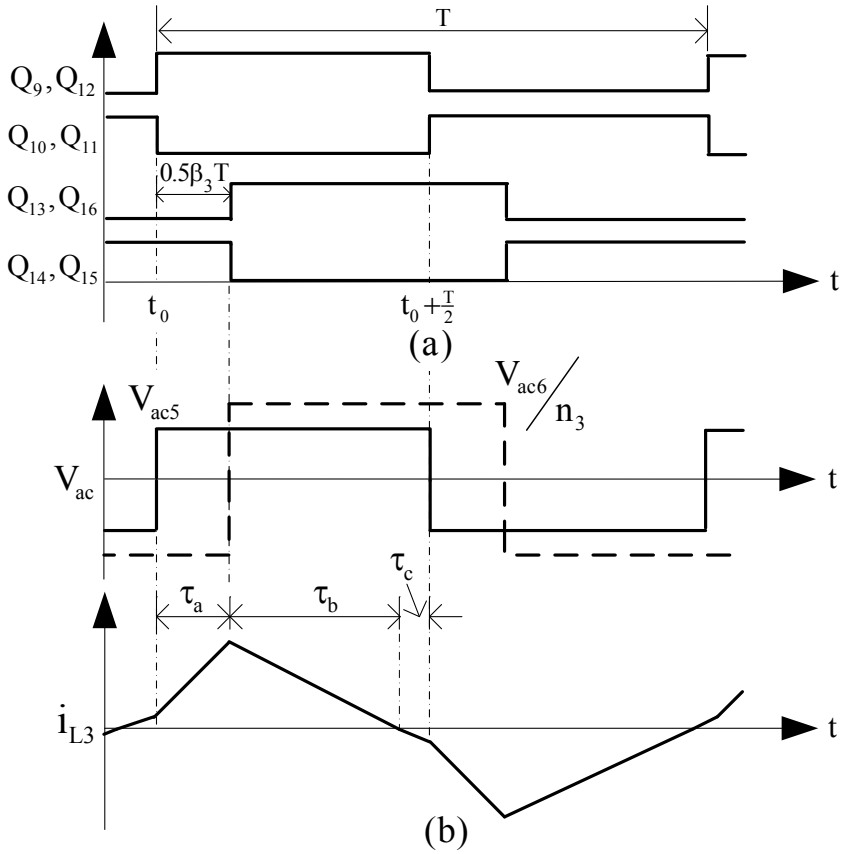

Figure 4.2: Phase shift modulation of DAB converter: (a) modulation sequence; (b) ideal voltage and current waveforms.

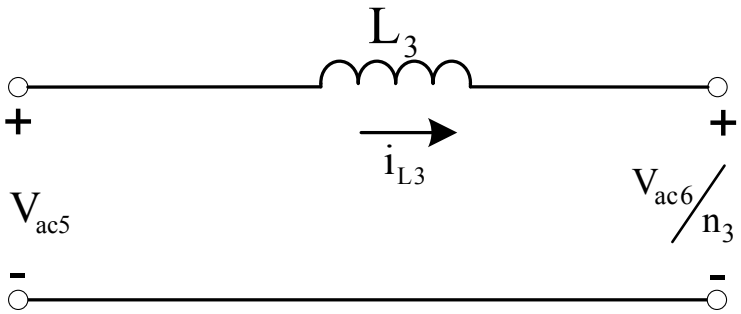

Figure 4.3: Simplified scheme of a dual active bridge DC/DC converter .

and magnitude of the power flow. For the boost direction, the power flow can be calculated as follows [54, 55]:

$$P_6 = \frac{TV_{sc}V_o\beta_3(1-\beta_3)}{2n_3L_3}. \tag{4.1}$$

For applications such as energy storage systems, DAB converters are expected to operate over a wide range of operating conditions without substantial performance degradation, especially for mobile applications. Our experiments revealed three phenomena that deteriorate the performance of the DABC and are not predicted by the conventional model [94, 95]. These phenomena are internal power transfer at zero phase shift, phase drift, and low system efficiency in certain operating ranges. We now describe each in detail.

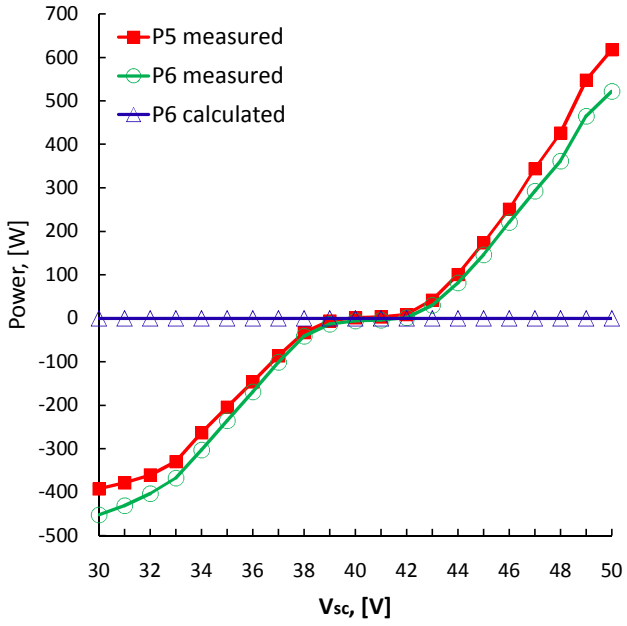

Figure 4.4: Internal power transfer for phase shift $\beta_3 = 0$.

The internal power transfer phenomenon refers to nonzero power transfer for zero phase shift. Fig.4.4 shows the measured power on both ports (P_5 and P_6) and the

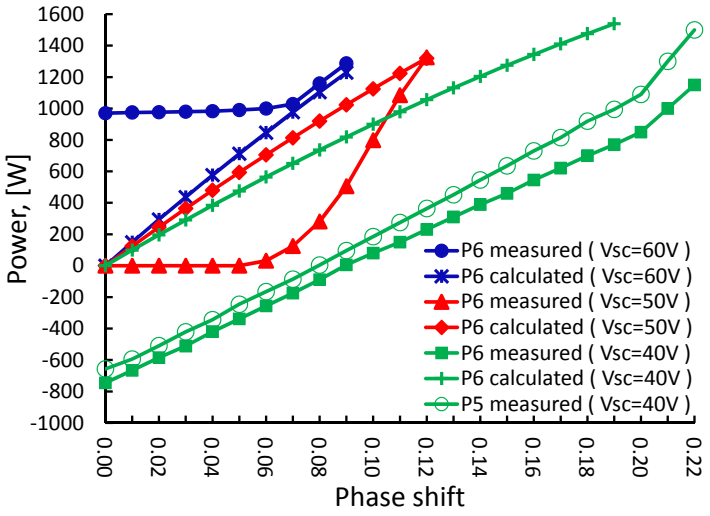

Figure 4.5: Power flow curves for $V_o = 80V$.

calculated P_6 using the conventional power transfer model [54], [55] for phase shift $\beta_3 = 0$. It should be noted that the difference between the measured power (P_5 and P_6) and the calculated power (P_6) is remarkable and that the difference increases as $|n_3 V_{sc} - V_o|$ increases. A similar phenomenon has been pointed out in [46], where it is referred to as the dead time[1] negative feedback effect. Moreover, Fig.4.5 compares the measured and the calculated power flow curves for different combinations of V_{sc} and V_o at different β_3. First of all, there are significant differences between the calculated and the measured power flow curves, especially when β_3 is small. Fig.4.5 suggests that the power flow model given by (4.1), albeit simple, can not be used for effective power flow characterization. Moreover, if $n_3 V_{sc} \neq V_o$, the output power is nonzero for $\beta_3 = 0$. For $n_3 V_{sc} > V_o$, the controllable output power is always larger than zero for $\beta_3 \in [0, 1]$. However, for better power management performance, it is desirable that the output power spans the entire operating range between zero and the maximum

[1]The dead time is a short time period between the modulation sequences of each pair of power switches on the same half bridge, e.g. between Q_9 and Q_{10}. The dead time is typically used to avoid short-through circuit instead of transferring power.

value. Finally, if $n_3 V_{sc} < V_o$, the power flow direction is reversed if β_3 is small. Under this condition, if we force $P_5 = 0$ (or $P_6 = 0$), we have $P_6 < 0$ (or $P_5 > 0$ respectively), leading to idling power (the DAB converter acts as an energy sink), and additional power loss.

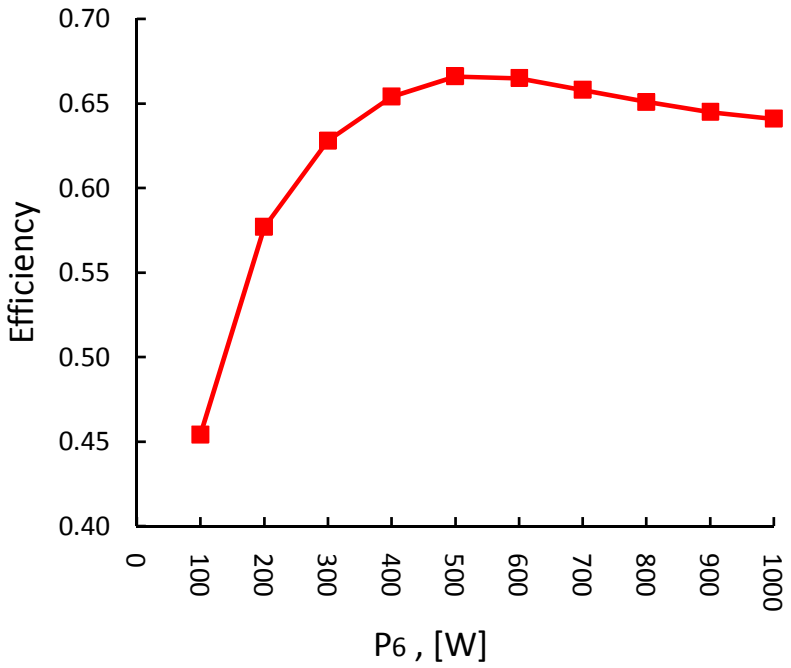

Figure 4.6: Measured efficiency curve for $V_{sc} = 30$.

Fig.4.6 shows the measured efficiency curve of the DABC operating with $V_{sc} = 30V$ and $V_o = 80V$. The maximum efficiency is less than 67% for this case. It is known that negative power leads to high conduction losses and therefore reduces the efficiency [36]. However, an analytical explanation of the conditions associated with the low system efficiency has not been fully explored yet.

In addition, the phase drift phenomenon has been observed in experimental tests when $n_3 V_{sc} \neq V_o$ and the commanded phase shift is zero. As shown in Fig.4.7, a phase drift can be identified in the transients between the voltage waveforms V_{ac5} and

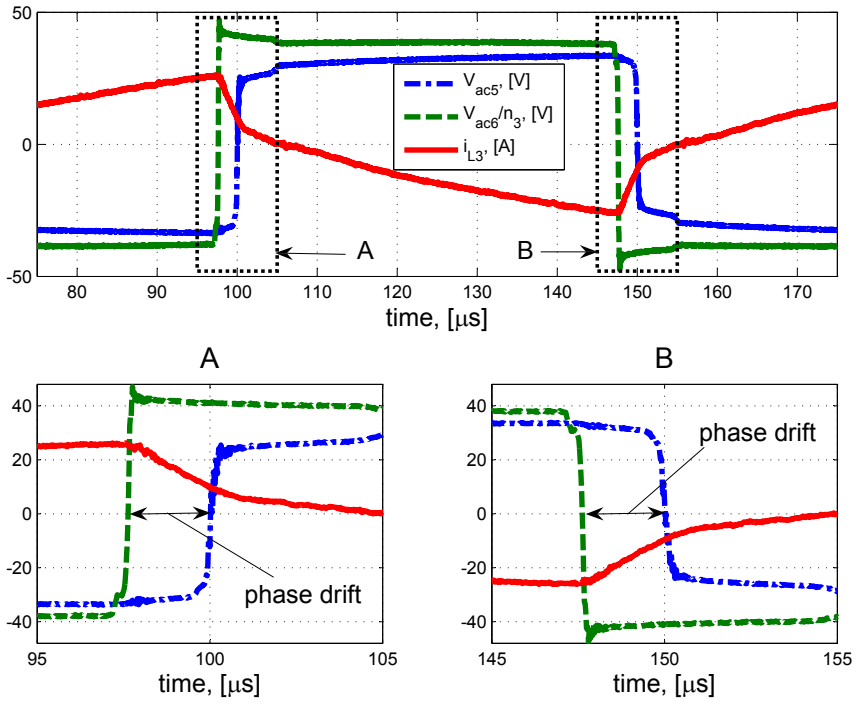

Figure 4.7: Phase drift phenomenon for $V_{sc} = 30$ and phase shift= 0 (The two plots at the bottom are zoomed in characteristics of the top one.).

V_{ac6}/n_3 while the desired phase difference is zero. The phase drift typically imposes a large voltage (with absolute value $\simeq V_{ac5} + V_{ac6}/n_3 \simeq V_{sc} + V_o/n_3$) across the inductor and significantly influences the inductor current i_{L3}, as shown in Fig.4.7. Therefore, it causes additional power transfer.

4.2 Conventional Power Flow Analysis

The goal of power flow analysis is to obtain an analytical power transfer equation that relates the power flow to the specified power circuit parameters and the phase shift [54], [55]. It is worthwhile to point out that the power flow analysis for both boost and buck directions is essentially the same because of the symmetric structure of the DAB converter. Therefore, for conciseness, only the boost direction will be

investigated in the subsequent analysis.

Since the dynamics of the capacitor voltages V_{sc} and V_o are much slower than that of the inductor current i_{L3}, we can assume that V_{sc} and V_o are constant over each switching period. Therefore, to compute the average power, we can define operating modes according to the evolution of i_{L3}. Whenever the inductor current i_{L3} either changes slope or crosses zero, the operating mode changes. Consider the case $nV_{sc} < V_o$ as an example. For the half switching period $[t_0, t_0 + \frac{T}{2}]$, there are three operating modes, namely $\mathcal{M}_1$, $\mathcal{M}_2$ and $\mathcal{M}_3$ with corresponding time intervals τ_a, τ_b and τ_c respectively as illustrated in Fig.4.2(b), where

$$\mathcal{M}_1 : t \in [t_0, t_0 + \tau_a];$$

$$\mathcal{M}_2 : t \in [t_0 + \tau_a, t_0 + \tau_a + \tau_b];$$

$$\mathcal{M}_3 : t \in [t_0 + \tau_a + \tau_b, t_0 + \tfrac{T}{2}].$$

Note that $\tau_a + \tau_b + \tau_c = T/2$. It is also worthwhile to point out that, for all waveforms of V_{ac}, i_{L3}, i_5 and i_6 presented in figures of this dissertation, the time-axis intersects the y-axis at $y = 0$.

If we ignore the difference between the input and output power and only consider the major parameters, namely V_{sc}, V_o, n_3, T and L_3, we have:

$$V_{ac5} - \frac{V_{ac6}}{n_3} = L_3 \frac{di_{L3}}{dt} = \begin{cases} V_{sc} + \frac{V_o}{n_3}, for\ \mathcal{M}_1; \\ V_{sc} - \frac{V_o}{n_3}, for\ \mathcal{M}_2\ and\ \mathcal{M}_3. \end{cases} \tag{4.2}$$

Given the symmetric structure of the DAB converter topology, at steady state, the average value of $i_{L3}(t)$ must be zero over one switching period T and $i_{L3}(t_0) = -i_{L3}(t_0 + \frac{T}{2})$.

Therefore,

$$i_{L3}(t_0 + \frac{T}{2}) = \frac{(n_3 V_{sc} - V_o)\tau_c}{n_3 L_3} = -i_{L3}(t_0), \tag{4.3}$$

$$i_{L3}(t_0 + \beta_3 \frac{T}{2}) = -\frac{(nV_{sc} - V_o)\tau_b}{n_3 L_3} = \frac{(n_3 V_{sc} + V_o)\tau_a}{n_3 L_3} + i_{L3}(t_0). \tag{4.4}$$

(4.3) and (4.4) lead to

$$\frac{(n_3 V_{sc} + V_o)\tau_a}{n_3 L_3} + \frac{(n_3 V_{sc} - V_o)\tau_b}{n_3 L_3} - \frac{(n_3 V_{sc} - V_o)\tau_c}{n_3 L_3} = 0. \tag{4.5}$$

Note that,

$$\tau_a = \frac{\beta_3 T}{2}, \tau_a + \tau_b + \tau_c = \frac{T}{2}. \tag{4.6}$$

Solving (4.5) and (4.6), we have

$$\tau_b = \frac{(n_3 V_{sc} - V_o) - 2n_3 V_{sc}\beta_3}{2(n_3 V_{sc} - V_o)} \frac{T}{2}, \tag{4.7}$$

$$\tau_c = \frac{(n_3 V_{sc} - V_o) + 2V_o\beta_3}{2(n_3 V_{sc} - V_o)} \frac{T}{2}. \tag{4.8}$$

With the assumption that the input and output voltages V_{sc} and V_o are constant over one switching period, the average output power P_6 can be calculated as:

$$\begin{aligned} P_6 &= \frac{2}{T}\int_{t_0}^{t_0+T/2} V_{sc} i_{L3}\, dt = V_{sc} \times \frac{2}{T}\int_{t_0}^{t_0+T/2} i_{L3}\, dt \\ &= \frac{2V_{sc}}{T}\left\{ \frac{i_{L3}(t_0 + \frac{T}{2})(\tau_c - \tau_a)}{2} + \frac{i_{L3}(t_0 + \beta_3\frac{T}{2})(\tau_a + \tau_b)}{2} \right\} \\ &= \frac{TV_{sc}V_o\beta_3(1-\beta_3)}{2n_3 L_3}. \end{aligned} \tag{4.9}$$

Remark 1 *At zero phase shift ($\beta_3 = 0, \tau_a = \frac{\beta_3 T}{2} = 0$), we have*

1. $\tau_b = \tau_c = \frac{T}{4}$;

2. *The slopes of* i_{L3} *are the same over the two modes* $\mathcal{M}_2$ *and* $\mathcal{M}_3$[2];

3. *The average current of* $\hat{i}_{L_3} = \frac{2}{T}\int_{t_0}^{t_0+\frac{T}{2}} i_{L3}\,dt = 0$, *therefore* $P_6 = 0$.

Note that for $n_3 V_{sc} \geq V_o$, the power flow expression is the same as (4.9) [54], [55].

Remark 2 *We define the power in the desired direction as the positive power and the power in the opposite direction as the negative power. (4.9) and Remark 7 suggest that, for zero phase shift, the positive power and the negative power are canceled over the half switching cycle if we only consider the major parameters. Therefore, the average output power is always zero. This conclusion contradicts with the experimental results shown in Fig.4.4, motivating an in-depth power flow analysis for the DAB converter (to be presented in the subsequent sections).*

4.3 Effects of Minor Parameters on Power Transfer of the DABC

Traditional power flow analysis for power converters only considers major parameters [65]. This is because most power converters use a dedicated inductor as the energy transfer element, and the input or output voltage is directly applied to the inductor. Therefore, the voltage loss of the power semiconductor is negligible. However, the DAB converter uses a μH or even nH level leakage inductor as the energy transfer element. The voltage applied to the inductor depends on $|V_{ac5} + V_{ac6}/n_3|$ and $|V_{ac5} - V_{ac6}/n_3|$ for different time intervals. For many applications [35], [36], $|V_{ac5} - V_{ac6}/n_3|$ is only several volts, which leads to the hypothesis that the power

[2]This property holds for all $\beta_3 \in [0, 1]$ by (4.2).

semiconductor voltage loss is not negligible for the power flow characterization of the DAB converter. On the other hand, the phase drift phenomenon and internal power transfer phenomenon are correlated to the dead time in experimental results. Dead time typically causes additional output voltage deviation and power loss for power converters [32, 66]. Therefore, an analysis of the dead time effect is necessary for understanding the phase drift phenomenon. In the following subsections, in addition to major parameters V_{sc}, V_o, L_3, T, n_3 and β_3 used in the conventional analysis, we investigate the effects of the minor parameters, namely power semiconductor voltage loss and dead time.

4.3.1 Power Semiconductor Voltage Loss Effect

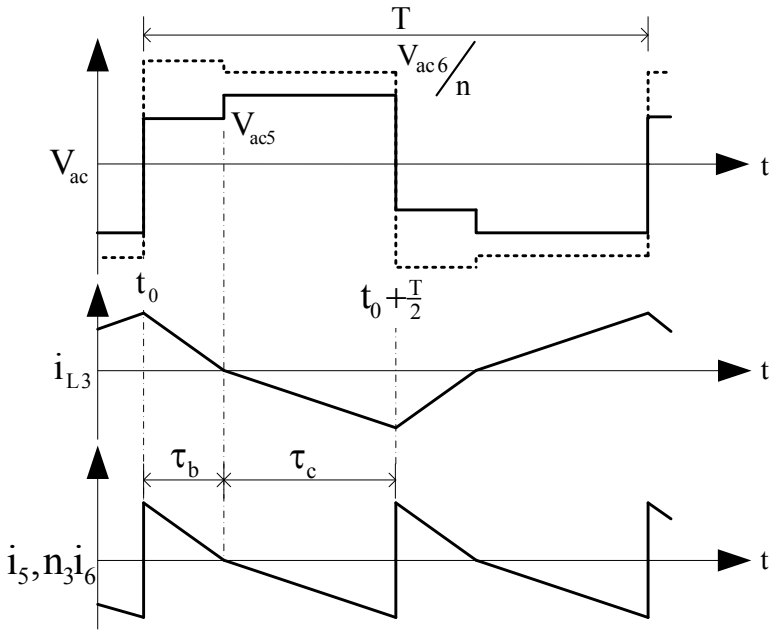

Figure 4.8: Ideal waveforms of DAB converter considering power semiconductor voltage loss.

To illustrate the effects of voltage loss across power switches, we again consider the case $n_3 V_{sc} < V_o$ and $\beta_3 = 0$. The ideal waveforms are shown in Fig.4.8. Let V_s

and V_d denote the voltage loss across the power switches $Q_9 - Q_{16}$ and anti-parallel diodes $D_9 - D_{16}$. Note that, for conciseness, we assume that the power switches and anti-parallel diodes of the primary full bridge have the same voltage loss as their corresponding counterparts of the secondary full bridge. In general, the voltage loss of a power semiconductor may not be constant for varying current. However, for a given operating range, it is reasonable to assume constant voltage loss because the conduction resistance of the power semiconductor is very small ($m\Omega$ level). We now proceed to characterize the power flow of the DAB converter as follows:

Define $\mathcal{M}_1$, $\mathcal{M}_2$ and $\mathcal{M}_3$ in the same way as in Section II (now $\tau_a = 0$ since $\beta_3 = 0$), where the voltages across the leakage inductor at different time intervals are given in Table.4.1:

Table 4.1: Voltage across the leakage inductor considering power semiconductors voltage loss

Operating mode	V_{ac5}	V_{ac6}
$\mathcal{M}_2$	$V_{sc} - 2V_s$	$V_o + 2V_d$
$\mathcal{M}_3$	$V_{sc} + 2V_d$	$V_o - 2V_s$

Given that $i_{L3}(t_0) = -i_{L3}(t_0 + T/2)$, we have

$$\frac{\tau_b}{\tau_c} = \frac{n_3 V_{sc} + 2nV_d - (V_o - 2V_s)}{n_3 V_{sc} - 2nV_s - (V_o + 2V_d)}. \tag{4.10}$$

(4.10) together with

$$\tau_a = 0, \tau_a + \tau_b + \tau_c = \frac{T}{2}. \tag{4.11}$$

will give,

$$\tau_b = \frac{n_3 V_{sc} - V_o + 2nV_d + 2V_s}{2n_3 V_{sc} - 2V_o - 2(n-1)(V_s - V_d)} \frac{T}{2}, \tag{4.12}$$

$$\tau_c = \frac{n_3 V_{sc} - V_o - 2nV_s - 2V_d}{2n_3 V_{sc} - 2V_o - 2(n-1)(V_s - V_d)} \frac{T}{2}. \tag{4.13}$$

Moreover,

$$i_5(t) = ni_6(t) = \begin{cases} i_{L3}(t),\ t \in [t_0, t_0 + \frac{T}{2}]; \\ -i_{L3}(t),\ t \in [t_0 + \frac{T}{2}, t_0 + T]. \end{cases} \tag{4.14}$$

$$i_{L3}(t_0 + \frac{T}{2}) = \frac{(n_3 V_{sc} - V_o + 2nV_d + 2V_s)\tau_c}{n_3 L_3}. \tag{4.15}$$

Therefore, the average power can be calculated as:

$$P_5 = \frac{2}{T}\int_0^{T/2} V_{sc} i_5 \, dt = \frac{2V_{sc}}{T}\left\{\frac{i_{L3}(t_0 + \frac{T}{2})(\tau_c - \tau_b)}{2}\right\}, \tag{4.16}$$

$$P_6 = \frac{2}{T}\int_0^{T/2} V_o i_6 \, dt = \frac{2V_o}{TV_{sc}}\int_0^{T/2} V_{sc}\frac{i_5}{n_3} \, dt = \frac{P_5 V_o}{n_3 V_{sc}}. \tag{4.17}$$

Remark 3 *At zero phase shift, the voltage loss of the power semiconductor can cause:*

1. $\tau_b \neq \tau_c$ *(as shown by (4.10));*
2. *The slope of* i_{L3} *is NOT the same for modes* $\mathcal{M}_2$ *and* $\mathcal{M}_3$*, since the voltage across the inductor* $V_{ac5} - V_{ac6}/n_3$*, calculated using data in Table.4.1, are different;*
3. $P_5 \neq 0$ *and* $P_6 \neq 0$ *as calculated in (4.16), (4.17).*

Therefore, the minor parameters V_s and V_d affect the distribution of positive power and negative power, leading to $P_5 \neq 0$ and $P_6 \neq 0$ at $\beta_3 = 0$. Taking this one step further, the effects of dead time will be considered in the next subsection.

4.3.2 Dead Time Effect

We now show that the existence of a dead time causes the phase drift phenomenon we noted in the Introduction. For continuity and simplicity, we consider again the

case with $n_3V_{sc} < V_o$ and $\beta_3 = 0$. Referring to the current and voltage waveforms plotted in Fig.4.9, suppose that the DAB is modulated by gating sequences V_g, with dead time T_d between transits at each half switching period. Given $n_3V_{sc} < V_o$, $i_{L3}(t)$ must be decreasing during $t_0 \leq t \leq t_0 + \frac{T}{2}$, since Q_9, Q_{12}, Q_{13} and Q_{16} are turned on and $V_{ac5} > 0$, $V_{ac6} > 0$. Given the symmetric structure of the topology, $i_{L3}(t_0) = -i_{L3}(t_0 + \frac{T}{2})$, we must have $i_{L3}(t_0) > 0$ and $i_{L3}(t_0 + \frac{T}{2}) < 0$, implying that i_5 has to pass through D_9 and D_{12} while i_6 passes through Q_{13} and Q_{16} during τ_c. At time $t = t_0 + \frac{T}{2}$, Q_9, Q_{12}, Q_{13} and Q_{16} are turned off, causing i_6 to be switched to D_{14} and D_{15} immediately while i_5 keeps passing through D_9 and D_{12}. This is equivalent to an undesired additional phase shift between V_{ac5} and V_{ac6} which enables i_5 passing the power devices Q_9/D_9 and Q_{12}/D_{12} during the dead time. We define the undesired phase shift as *phase drift*. If $i_{L3}(t_0 + \frac{T}{2})$ is not large enough, then $i_{L3}(t)$ will go to zero before $t = t_0 + \frac{T}{2} + T_d$ as shown in Fig.4.9a (Case I), meaning that there is a negative phase drift $\in [-2T_d/T, 0]$. Otherwise, i_5 keeps passing through D_9 and D_{12} until the dead time ends and Q_{10} and Q_{11} are turned on as shown in Fig.4.9b (Case II), leading to a negative phase drift $-2T_d/T$. Similarly, for the case $n_3V_{sc} > V_o$ and $d = 0$, there is a phase drift (lead) for the primary voltage V_{ac5} in comparison with the secondary voltage V_{ac6}.

Remark 4 *The phase drift only provides the freewheeling path for the inductor current i_{L3} and i_{L3} can reach zero but never can cross zero and be built up.*

We next derive expressions for the power flow that include the dead time as well as the voltage loss:

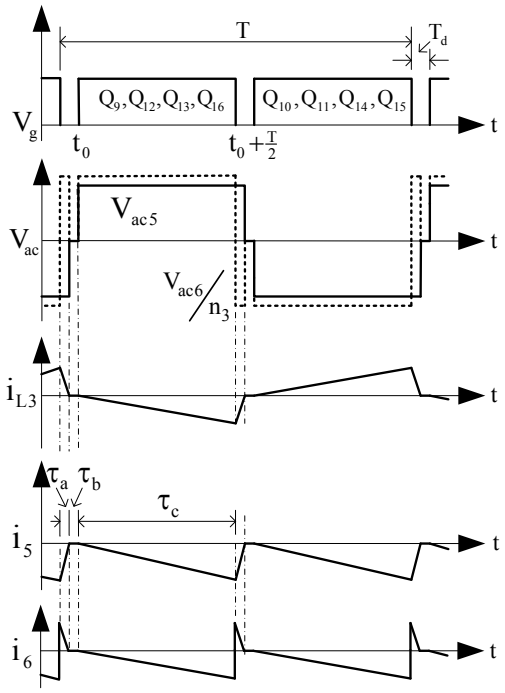

(a) *Case I*

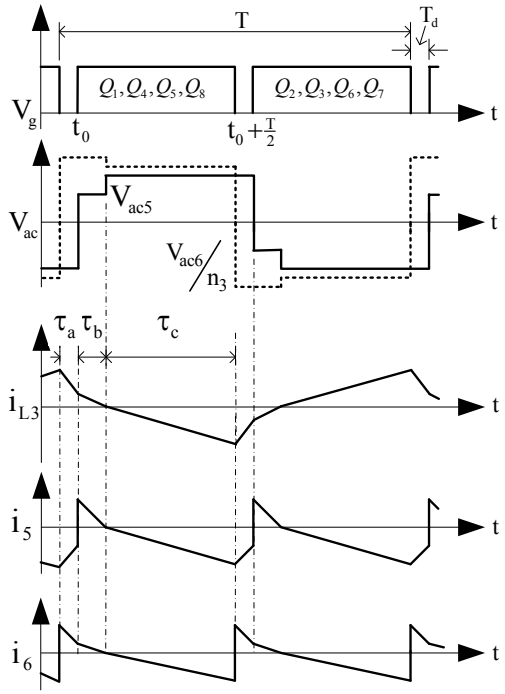

(b) *Case II*

Figure 4.9: Dead time effect of DAB converter.

Case I

If $|V_{ac5} - V_{ac6}/n_3|$ is not large enough to build large $|i_{L3}|$, then $|i_{L3}|$ reduces to zero before $t = t_0 + \frac{T}{2} + T_d$, which results in a phase drift $\in [-2T_d/T, 0]$. In this case, the ideal waveforms are shown in Fig.4.9a. Define $\mathcal{M}_1$, $\mathcal{M}_2$ and $\mathcal{M}_3$ in the same way as in Section II, where the voltages across the leakage inductor at different time intervals are shown in Table.4.2. Here, $\mathcal{M}_2$ is not considered given that $i_{L3} = 0$, $i_5 = 0$ and $i_6 = 0$ for $t \in \mathcal{M}_2$.

Table 4.2: Voltage across the leakage inductor for case I

Operating mode	V_{ac5}	V_{ac6}
$\mathcal{M}_1$	$-(V_{sc} + 2V_d)$	$V_o + 2V_d$
$\mathcal{M}_3$	$V_{sc} + 2V_d$	$V_o - 2V_s$

From Table.4.2 and

$$\tau_c = \frac{T}{2} - T_d. \tag{4.18}$$

we can derive,

$$\tau_a = \frac{n_3 V_{sc} - V_o + 2n_3 V_d + 2V_s}{n_3 V_{sc} + V_o + 2(n_3 + 1)V_d} \tau_c, \tag{4.19}$$

$$i_{L3}(t_0 + \frac{T}{2}) = \frac{(n_3 V_{sc} - V_o + 2n_3 V_d + 2V_s)\tau_c}{n_3 L_3}. \tag{4.20}$$

Moreover,

$$i_5(t) = \begin{cases} -i_{L3}(t), for\ t \in [t_0, t_0 + \tau_a]; \\ i_{L3}(t), for\ t \in [t_0 + \tau_a, t_0 + T/2 + \tau_a]; \\ -i_{L3}(t), for\ t \in [t_0 + T/2 + \tau_a, t_0 + T]. \end{cases} \tag{4.21}$$

$$i_6(t) = \begin{cases} \frac{i_{L3}(t)}{n_3}, for\ t \in [t_0, t_0 + T/2]; \\ -\frac{i_{L3}(t)}{n_3}, for\ t \in [t_0 + T/2, t_0 + T]. \end{cases} \tag{4.22}$$

Therefore, the average powers, P_5 and P_6, are

$$P_5 = \frac{2}{T}\int_0^{T/2} V_{sc} i_5\, dt = \frac{2V_{sc}}{T}\left\{\frac{i_{L3}(t_0 + \frac{T}{2})(\tau_a + \tau_c)}{2}\right\}, \tag{4.23}$$

$$P_6 = \frac{2}{T}\int_0^{T/2} V_o i_6\, dt = \frac{2V_o}{n_3 T}\left\{\frac{i_{L3}(t_0 + \frac{T}{2})(\tau_c - \tau_a)}{2}\right\}. \tag{4.24}$$

Note that, for Case I, $|i_{L3}|$ reduces to zero before $t = t_0 + \frac{T}{2} + T_d$. This fact implies $\tau_a + \tau_c \leq T/2$. Therefore, for $\tau_b = T/2 - \tau_a - \tau_c$, there is no power transfer ($i_{L3} = 0$).

Case II

If $|V_{ac5} - V_{ac6}/n_3|$ is large enough to build large $|i_{L3}|$ such that $i_{L3}(t_0 + \frac{T}{2} + T_d) \neq 0$, then the phase drift equals to $-2T_d/T$. In this case, the ideal waveforms are shown in Fig.4.9b. Defining $\mathcal{M}_1$, $\mathcal{M}_2$ and $\mathcal{M}_3$ as in Section II, the voltages across the leakage inductor at different time intervals are shown in Table.4.3.

Table 4.3: Voltage across the leakage inductor for case II

Operating mode	V_{ac5}	V_{ac6}
$\mathcal{M}_1$	$-(V_{sc} + 2V_d)$	$V_o + 2V_d$
$\mathcal{M}_2$	$V_{sc} - 2V_s$	$V_o + 2V_d$
$\mathcal{M}_3$	$V_{sc} + 2V_d$	$V_o - 2V_s$

Given Table.4.3 and

$$\tau_a = T_d, \tag{4.25}$$

$$\tau_a + \tau_b + \tau_c = \frac{T}{2}. \tag{4.26}$$

we can derive,

$$\tau_b = \frac{(n_3 V_{sc} - V_o + 2n_3 V_d + 2V_s)\frac{T}{2} + 2(V_o + V_d - V_s)T_d}{2n_3 V_{sc} - 2V_o - 2(n_3 - 1)(V_s - V_d)}, \tag{4.27}$$

$$\tau_c = \frac{(n_3 V_{sc} - V_o - 2V_d - 2n_3 V_s)\frac{T}{2} - 2n_3(V_{sc} + V_d - V_s)T_d}{2n_3 V_{sc} - 2V_o - 2(n_3 - 1)(V_s - V_d)}. \tag{4.28}$$

Moreover,

$$i_5(t) = \begin{cases} -i_{L3}(t), for\ t \in [t_0, t_0 + \tau_a]; \\ i_{L3}(t), for\ t \in [t_0 + \tau_a, t_0 + T/2 + \tau_a]; \\ -i_{L3}(t), for\ t \in [t_0 + T/2 + \tau_a, t_0 + T]. \end{cases} \tag{4.29}$$

$$i_6(t) = \begin{cases} \frac{i_{L3}(t)}{n_3}, for\ t \in [t_0, t_0 + T/2]; \\ -\frac{i_{L3}(t)}{n_3}, for\ t \in [t_0 + T/2, t_0 + T]. \end{cases} \tag{4.30}$$

$$i_{L3}(t_0 + T_d) = \frac{-(n_3 V_{sc} - V_o - 2V_d - 2n_3 V_s)\tau_b}{n_3 L_3}, \tag{4.31}$$

$$i_{L3}(t_0 + \frac{T}{2}) = -i_{L3}(t_0) = \frac{(n_3 V_{sc} - V_o + 2n_3 V_d + 2V_s)\tau_c}{n_3 L_3}. \tag{4.32}$$

Therefore, the average power P_5 and P_6 are

$$P_5 = \frac{2}{T}\int_0^{T/2} V_{sc} i_5\, dt = \frac{2V_{sc}}{T}\left\{\frac{i_{L3}(t_0 + \frac{T}{2})(\tau_a + \tau_c)}{2} + \frac{i_{L3}(t_0 + T_d)(\tau_b - \tau_a)}{2}\right\}, \tag{4.33}$$

$$P_6 = \frac{2}{T}\int_0^{T/2} V_o i_6\, dt = \frac{2V_o}{n_3 T}\left\{\frac{i_{L3}(t_0 + \frac{T}{2})(\tau_c - \tau_a)}{2} + \frac{i_{L3}(t_0 + T_d)(\tau_a + \tau_b)}{2}\right\}. \tag{4.34}$$

Similarly, for the case of $n_3 V_{sc} > V_o$ and $\beta_3 = 0$, a model for P_5 and P_6 can be derived in the same manner. Given the symmetric structure of the DAB converter,

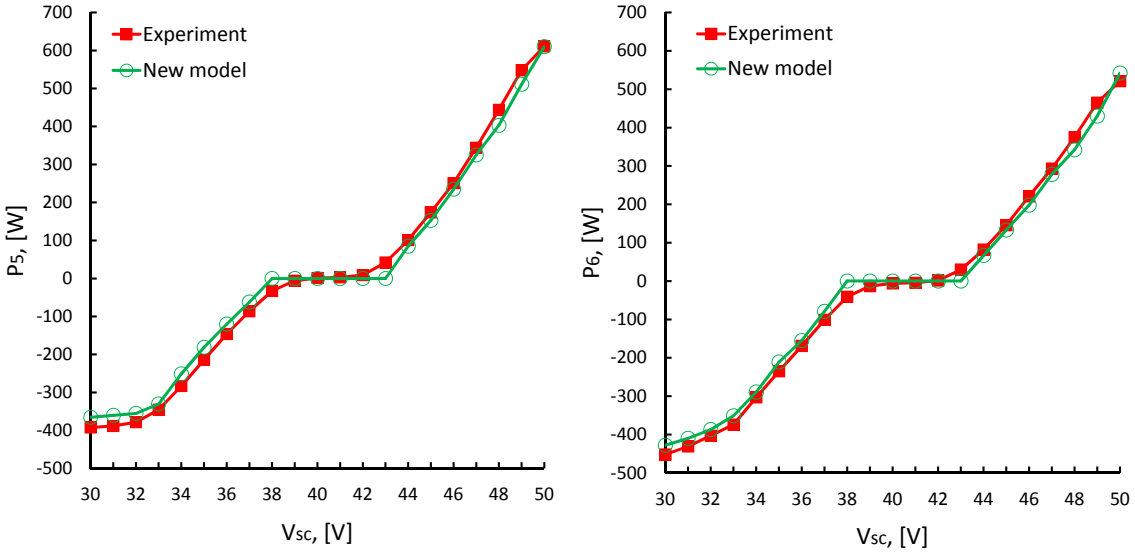

Figure 4.10: Power flow model validation for $V_o = 80V$ and $\beta_3 = 0$: (a) P_5; (b) P_6.

the analysis is also valid for the buck direction ($\beta_3 \in [-1, 0]$).

Note that for the case of $\beta_3 \neq 0$, *Case I* and *Case II* can be combined. This is because small β_3 can build up $|i_{L3}|$ such that $i_{L3}(t_0 + \frac{T}{2} + T_d) \neq 0$, resulting in a phase drift equal to $-2T_d/T$.

Remark 5 *The dead time effect analysis for $\beta_3 = 0$ can be extended to $\beta_3 \neq 0$. Let t_0 donate the time instance when the transformer primary voltage V_{ac5} changes polarity to positive. Then, if $i_{L3}(t_0 + \frac{T}{2}) \times i_{L3}(t_0 + \frac{T}{2} + \frac{\beta_3 T}{2}) > 0$, there is a phase drift between V_{ac5} and the transformer secondary voltage V_{ac6}. More specifically, if $i_{L3}(t_0 + \frac{T}{2}) < 0$, $i_{L3}(t_0 + \frac{T}{2}) \times i_{L3}(t_0 + \frac{T}{2} + \frac{\beta_3 T}{2}) > 0$ implies $i_{L3}(t_0 + \frac{T}{2} + \frac{\beta_3 T}{2}) < 0$. Therefore, i_{L3} can be immediately switched to different power devices at $t = t_0 + \frac{T}{2} + \frac{\beta_3 T}{2}$ while i_{L3} has to pass through the original devices at $t = t_0 + \frac{T}{2}$ until the end of the dead time, leading to a negative phase shift $\frac{-2T_d}{T}$; similarly, if $i_{L3}(t_0 + \frac{T}{2}) > 0$, there is a positive phase shift $\frac{2T_d}{T}$. Moreover, if the DAB converter operates in a small β_3 region, then*

there is a phase drift because a small β_3 *leads to* $i_{L3}(t_0 + \frac{T}{2}) \times i_{L3}(t_0 + \frac{T}{2} + \frac{\beta_3 T}{2}) > 0$. *Moreover, if* $i_{L3}(t_0 + \frac{T}{2}) \times i_{L3}(t_0 + \frac{T}{2} + \frac{\beta_3 T}{2}) < 0$, *there is no phase drift between* V_{ac5} *and* V_{ac6}. *This is because* i_{L3} *can be immediately switched to different power devices at* $t = t_0 + \frac{T}{2}$ *and* $t = t_0 + \frac{T}{2} + \frac{\beta_3 T}{2}$ *if* $i_{L3}(t_0 + \frac{T}{2}) \times i_{L3}(t_0 + \frac{T}{2} + \frac{\beta_3 T}{2}) < 0$.

Fig.4.10 shows that the calculated P_5 and P_6 based on the analysis presented in this section are very close to the experimental results. Therefore, the minor parameters V_s, V_d and T_d affect the slope of i_{L3} and the length of the time intervals τ_a, τ_b and τ_c, and consequently influence the distribution of positive power and negative power and the average power P_5 and P_6. The effectiveness of the results for $\beta_3 = 0$ (Fig.4.10) and the extension of dead time effect analysis to $\beta_3 \neq 0$ (Remark 5) motivate the authors to explore power flow characterization of the DAB converter over a wide operating range, which will be discussed in the next section.

4.4 Power Flow Characterization of the DABC over a Wide Operating Range

We now derive a general characterization for the power flow of the DAB converter. To do so, we consider three different cases, namely $n_3 V_{sc} < V_o$, $n_3 V_{sc} = V_o$ and $n_3 V_{sc} > V_o$, because $V_{ac5} + V_{ac6}/n_3 \simeq V_{sc} + V_o/n_3$ and $V_{ac5} - V_{ac6}/n_3 \simeq V_{sc} - V_o/n_3$ determine the shape of i_{L3}. For each case, we divide the operating range $\beta_3 \in [0, 1]$ of the converter into several regions, defined as illustrated in Fig.4.11 and described in detail below. For different operating regions, Fig.4.12 shows the corresponding ideal waveforms of the DAB converter, while Table.4.4 lists all necessary equations for deriving the boundaries and the power flow equations for different regions. The

following intermediate variables are defined in order to present Table.4.4:

$$K_1 = n_3 V_{sc} - V_o + 2n_3 V_d + 2V_s, \tag{4.35}$$

$$K_2 = n_3 V_{sc} - V_o - 2n_3 V_s - 2V_d, \tag{4.36}$$

$$K_3 = 2n_3(V_{sc} + V_d - V_s), \tag{4.37}$$

$$K_4 = 2(V_o + V_d - V_s), \tag{4.38}$$

$$K_5 = n_3 V_{sc} + V_o - 2(n_3 + 1)V_s, \tag{4.39}$$

$$K_6 = n_3 V_{sc} + V_o + 2(n_3 + 1)V_d, \tag{4.40}$$

$$K_7 = 2n_3 V_{sc} - 2V_o - 2(n_3 - 1)(V_s - V_d), \tag{4.41}$$

$$K_8 = 2n_3 V_{sc} - 2V_o - 2(n_3 + 1)(V_s - V_d), \tag{4.42}$$

$$i_7 = i_{L3}(t_0), \tag{4.43}$$

$$i_8 = i_{L3}(t_0 + \tau_a), \tag{4.44}$$

$$i_9 = i_{L3}(t_0 + \tau_a + \tau_b). \tag{4.45}$$

We now describe each of these regions in detail.

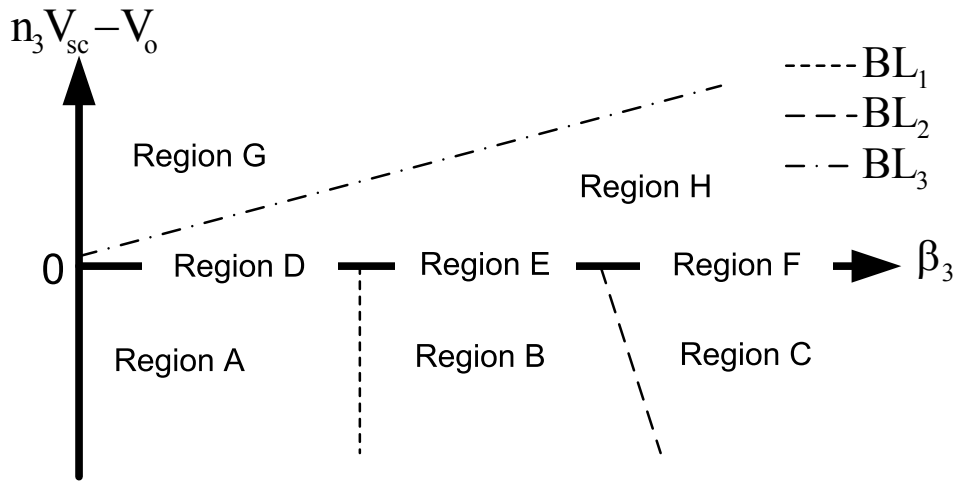

Figure 4.11: Operating region separation.

For $n_3V_{sc} < V_o$, referring to Fig.4.12A/B and Table 4.4 (Region A/B), $i_{L3}(t_0) > 0$ while $i_{L3}(t_0 + \frac{T}{2}) < 0$ if the converter operates in a small β_3 region. Moreover, $i_{L3}(t_0 + \frac{T}{2} + \frac{\beta_3 T}{2}) < 0$ for a small β_3. Therefore, following Remark 5, there is a phase drift $\delta = -\frac{2T_d}{T}$ over a certain range of β_3. So, the DAB converter will be operating with three different regions in this case. The first region (Region A) is $0 \leq \beta_3 \leq \frac{2T_d}{T}$, wherein $\beta_3 + \delta$ is less than zero due to the phase drift. Let BL_1, defined as $\{(V_{sc}, V_o, \beta_3) | \beta_3 = \frac{2T_d}{T}, n_3V_{sc} - V_o \leq 0\}$, represents the boundary line between Region A and Region B. In Region B, the phase drift phenomenon still exists, but the actual phase shift is larger than zero. However, referring to Fig.4.12B and Table 4.4 (Region B), τ_c decreases as β_3 increases. If $\beta_3 = \frac{-(n_3V_{sc} - V_o - 2V_d - 2n_3V_s)}{2(V_o + V_d - V_s)} + 2\frac{T_d}{T}$, $i_{L3}(t_0 + \frac{T}{2}) = 0$ ($\tau_c = 0$). Let BL_2, defined as $\{(V_{sc}, V_o, \beta_3) | \beta_3 = \frac{-(n_3V_{sc} - V_o - 2V_d - 2n_3V_s)}{2(V_o + V_d - V_s)} + 2\frac{T_d}{T}, n_3V_{sc} - V_o \leq 0\}$, denotes the boundary line between Region B and C, $i_{L3}(t_0 + \frac{T}{2}) > 0$ if the converter operates at the right side of the boundary line BL_2. Moreover, $i_{L3}(t_0 + \frac{T}{2} + \frac{\beta_3 T}{2}) < 0$ in that case, so the current in both bridges can be immediately switched. Therefore, there is no phase drift, leading to the third region (Region C).

For $n_3V_{sc} = V_o$, there is a phase drift $\delta = -\frac{2T_d}{T}$ for small β_3 by as discussed in Remark 5. This is because the DABC works with Discontinuous Current Mode (DCM) for small β_3 such that $i_{L3}(t_0 + \frac{T}{2}) < 0$ and $i_{L3}(t_0 + \frac{T}{2} + \frac{\beta_3 T}{2}) < 0$. Moreover, there is no power transfer if $\beta_3 \leq \frac{2T_d}{T}$ since $i_{L3}(t_0 + \frac{T}{2}) \simeq 0$ and the phase drift only provide freewheeling path for i_{L3} and can not build up inductor current (Remark 4). The DABC operates with Continuous Current Mode (CCM) ($i_{L3}(t_0 + \frac{T}{2}) > 0$) for large β_3, and there is no phase drift. Therefore, three regions are defined in this case. The first region (Region D) is defined by $0 \leq \beta_3 \leq \frac{2T_d}{T}$, where there is no power transfer. The DABC operates with DCM mode in the second region (Region E) wherein $\delta = -\frac{2T_d}{T}$. For $\beta_3 = \frac{(2V_d + 2n_3V_s)}{2(V_o + V_d - V_s)} + 2\frac{T_d}{T}$, referring to Fig.4.12E and Table 4.4 (Region E), we have $i_{L3}(t_0 + \frac{T}{2}) = 0$ ($\tau_c = 0$). Since $n_3V_{sc} = V_o$, we can use

the same boundary line BL_2 to represent the boundary line separating Region E and F. If the converter operates at the right side of the boundary line BL_2, we have $i_{L3}(t_0 + \frac{\beta_3 T}{2}) > 0$ and $i_{L3}(t_0 + \frac{T}{2} + \frac{\beta_3 T}{2}) < 0$, leading to the third region (Region F) wherein phase drift $\delta = 0$.

For $n_3 V_{sc} > V_o$ and small β_3, the phase drift is $\delta = \frac{2T_d}{T}$ (Remark 5) because $i_{L3}(t_0 + \frac{T}{2}) > 0$ and $i_{L3}(t_0 + \frac{T}{2} + \frac{\beta_3 T}{2}) > 0$. Therefore, two regions are defined in this case. For the first region (Region G), the actual phase shift equals to $\beta_3 + \frac{2T_d}{T}$. If $\beta_3 = \frac{(n_3 V_{sc} - V_o - 2V_d - 2n_3 V_s)}{2n_3(V_{sc} + V_d - V_s)} - \frac{2T_d}{T}$, then $i_{L3}(t_0 + \frac{T}{2} + \frac{\beta_3 T}{2}) = 0$ ($\tau_b = 0$). Let BL_3, defined as $\{(V_{sc}, V_o, \beta_3) | \beta_3 = \frac{(n_3 V_{sc} - V_o - 2V_d - 2n_3 V_s)}{2n_3(V_{sc} + V_d - V_s)} - \frac{2T_d}{T}, n_3 V_{sc} - V_o > 0\}$, representing the boundary line between Region G and H. If the converter operates at the right side of the boundary line BL_3, we have $i_{L3}(t_0 + \frac{T}{2}) > 0$ and $i_{L3}(t_0 + \frac{T}{2} + \frac{\beta_3 T}{2}) < 0$, leading to the second region (Region H) with zero phase drift.

Note that for all of three cases, namely $n_3 V_{sc} < V_o$, $n_3 V_{sc} = V_o$ and $n_3 V_{sc} > V_o$, we assume that the operating mode of the DAB converter will transfer from the region with a phase drift (Region B, E or G) to the corresponding one without phase drift (Region C, F or H) immediately whenever β_3 acroses the boundary lines BL_2 and BL_3, respectively. But in reality, there will be a short interval wherein the phase drift phenomenon fades away gradually if β_3 acroses the boundary lines. Due to the symmetric structure of the converter, the analysis can be also applied for the buck direction operation.

The power flow analysis for different regions can be performed following the same procedure as presented in Section III. Note that there is no power transfer for Region D, and Regions F and H have the same power flow characterization as Region C. Therefore, only waveforms and equations of Region A, B, C, E and G are provided in Fig.4.12 and Table.4.4.

Remark 6 *For different operating regions depicted in Fig.4.11, the influence of the*

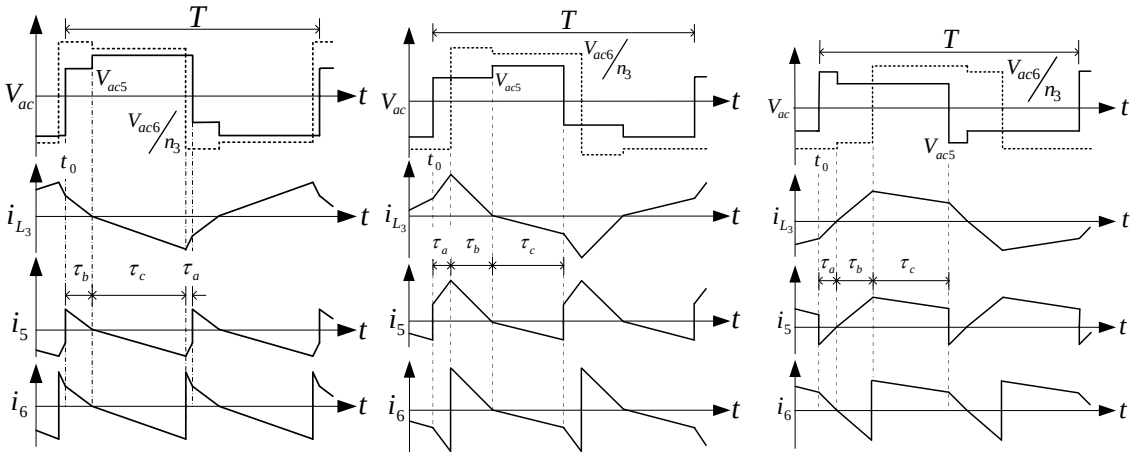

(a) Region A (b) Region B (c) Region C

(d) Region E (e) Region G

Figure 4.12: Ideal waveforms for DAB converter with phase shift modulation strategy.

Table 4.4: Power flow characterization table

Region	Mode	V_{ac5}	V_{ac6}	τ_a,τ_b,τ_c	i_7	i_8	i_9	P_5	P_6
A	$\mathcal{M}_1$	$-(V_{sc}+2V_d)$	V_o+2V_d	$T_d-d\frac{T}{2}$	$-\frac{K_1\tau_c}{n_3L_3}$	$-\frac{K_2\tau_b}{n_3L_3}$	0	$\frac{V_{sc}[i_4(\tau_b-\tau_a)-i_3(\tau_a+\tau_c)]}{T}$	$\frac{V_o[i_4(\tau_b+\tau_a)+i_3(\tau_a-\tau_c)]}{nT}$
	$\mathcal{M}_2$	$V_{sc}-2V_s$	V_o+2V_d	$\frac{K_1\frac{T}{2}+K_4\tau_a}{K_7}$					
	$\mathcal{M}_3$	$V_{sc}+2V_d$	V_o-2V_s	$\frac{K_2\frac{T}{2}-K_3\tau_a}{K_7}$					
B	$\mathcal{M}_1$	$V_{sc}-2V_s$	$-(V_o-2V_s)$	$d\frac{T}{2}-T_d$	$-\frac{K_1\tau_c}{n_3L_3}$	$-\frac{K_2\tau_b}{n_3L_3}$	0	$\frac{V_{sc}[i_4(\tau_a+\tau_b)+i_3(\tau_a-\tau_c)]}{T}$	$\frac{V_o[i_4(\tau_b-\tau_a)-i_3(\tau_a+\tau_c)]}{nT}$
	$\mathcal{M}_2$	$V_{sc}-2V_s$	V_o+2V_d	$\frac{K_1\frac{T}{2}-K_3\tau_a}{K_7}$					
	$\mathcal{M}_3$	$V_{sc}+2V_d$	V_o-2V_s	$\frac{K_2\frac{T}{2}+K_4\tau_a}{K_7}$					
C	$\mathcal{M}_1$	$V_{sc}+2V_d$	$-(V_o+2V_d)$	$\frac{K_2T/2+K_4dT/2}{K_8}$	$-\frac{K_6\tau_a}{n_3L_3}$	0	$\frac{K_5\tau_b}{n_3L_3}$	$\frac{V_{sc}[i_5(\tau_b+\tau_c)+i_3(\tau_a-\tau_c)]}{T}$	$\frac{V_o[i_5(\tau_c-\tau_b)-i_3(\tau_a+\tau_c)]}{nT}$
	$\mathcal{M}_2$	$V_{sc}-2V_s$	V_o-2V_s	$\frac{-K_2\frac{T}{2}+K_3d\frac{T}{2}}{K_8}$					
	$\mathcal{M}_3$	$V_{sc}-2V_s$	V_o+2V_d	$(1-d)\frac{T}{2}$					
E	$\mathcal{M}_1$	$V_{sc}-2V_s$	$-(V_o-2V_s)$	$d\frac{T}{2}-T_d$	0	$\frac{K_5\tau_a}{n_3L_3}$	0	$\frac{V_{sc}i_4(\tau_a+\tau_b)}{T}$	$\frac{V_oi_4(\tau_b-\tau_a)}{nT}$
	$\mathcal{M}_2$	$V_{sc}-2V_s$	V_o+2V_d	$-\frac{K_5\tau_a}{K_2}$					
	$\mathcal{M}_3$	$V_{sc}-2V_s$	V_o+2V_d	$\frac{T}{2}-\tau_a-\tau_c$					
G	$\mathcal{M}_1$	$V_{sc}+2V_d$	$-(V_o+2V_d)$	$d\frac{T}{2}+T_d$	$-\frac{K_1\tau_b}{n_3L_3}$	$\frac{K_2\tau_c}{n_3L_3}$	0	$\frac{V_{sc}[i_4(\tau_a+\tau_b)+i_3(\tau_a-\tau_c)]}{T}$	$\frac{V_o[i_4(\tau_a+\tau_b)+i_3(\tau_a+\tau_c)]}{nT}$
	$\mathcal{M}_2$	$V_{sc}+2V_d$	V_o-2V_s	$\frac{K_2\frac{T}{2}-K_3\tau_a}{K_7}$					
	$\mathcal{M}_3$	$V_{sc}-2V_s$	V_o+2V_d	$\frac{K_1\frac{T}{2}+K_4\tau_a}{K_7}$					

minor parameters on operating regions are summarized as follows:

1. *Dead time introduces negative phase drift in Regions A, B, D and E and positive phase drift in Region G. Dead time has no impact in Regions C, F and H. Moreover, in Regions A, B, and G, the converter operates with hard switching since it does not satisfy the soft-switching condition given by [54]. In addition, phase drift introduces additional negative power over each half switching period in Regions A, B, and G, leading to high conduction loss. Furthermore, for high power applications, since the dead time has to be chosen large enough to assure safe operation of the converter, the dead time effect will be significant if the converter operates in Region A, B and G. Therefore, the DAB converter should be designed such that the nominal operation point is outside Region A, B and G to achieve high system efficiency.*

2. *For all operating regions, the voltage loss of power devices affects the slope of i_{L3} and the distribution of positive power and negative power, and consequently influence the average power P_5 and P_6. Moreover, the voltage drop effect is more prominent for low voltage applications than that for high voltage applications, where an external inductor is often used as the energy transfer element and high voltage will be applied to the inductor in latter case.*

Fig.4.13 shows the power curves of the conventional model and the new model for $V_{sc} = 30V$, $V_o = 80V$, $V_s = 2V$, $V_d = 1V$ and $\beta_3 \in [0, 1]$. If the minor parameters are nonzero, from the power flow curves calculated by the new model, if $0 \leq \beta_3 < 0.078$, then $P_5 < 0$ and $P_6 < 0$, indicating that the power flow direction is opposite to the desired direction (*Reversed Power Flow*). For $0.078 \leq \beta_3 < 0.088$ or $0.96 \leq \beta_3 \leq 1$, $P_5 > 0$ and $P_6 < 0$, the DAB converter acts as an energy sink (*Energy Sink*), meaning that the converter draws power from both the P_5 and P_6 ports and the

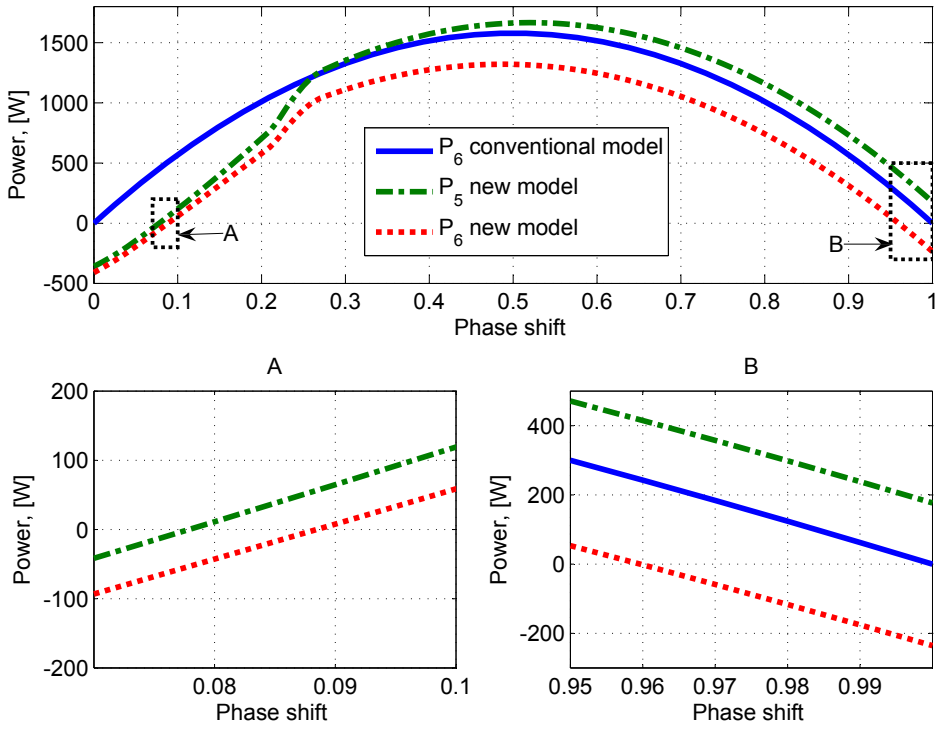

Figure 4.13: Power flow characteristics for $V_{sc} = 30V$, $V_o = 80V$, $V_s = 2V$, $V_d = 1V$ and $T_d = 2.5\mu s$.

energy is dissipated in the power devices. For $0.088 \leq \beta_3 \leq 0.96$, we have $P_5 > 0$ and $P_6 > 0$, illustrating that the DAB converter delivers power with the desired direction. Moreover, at $\beta_3 = 0.088$, the fact that $P_6 = 0$ suggests that the positive power and the negative power are canceled. So the efficiency is extremely low (*Extremely Low Efficiency*) if the DAB converter operates at the region close to $\beta_3 = 0.088$. Therefore, new characteristics such as *Reversed Power Flow* and *Energy Sink* can be analytically identified and the *Extremely Low Efficiency* phenomenon also can be explained by the new power flow model. Moreover, the DAB converter reaches the maximum output power at $\beta_3 = 0.5$. For the same output power, if the DAB converter operates in the $\beta_3 < 0.5$ region, the input power is less than that of the converter operating in the $\beta_3 > 0.5$ region, suggesting that the DAB converter should operate in the $\beta_3 < 0.5$ region to achieve high efficiency. Actually, many DAB converters operates in a small

β_3 region [46], where the effect of the minor parameters is more significant, justifying the technical contribution of this paper. It is worthwhile to point out that both P_5 and P_6 calculated by the new model are equal to P_6 calculated by the conventional model for the whole operating range if the minor parameters V_s, V_d and T_d are zero, suggesting that the new power flow model is consistent with the conventional analysis as described in Section II.

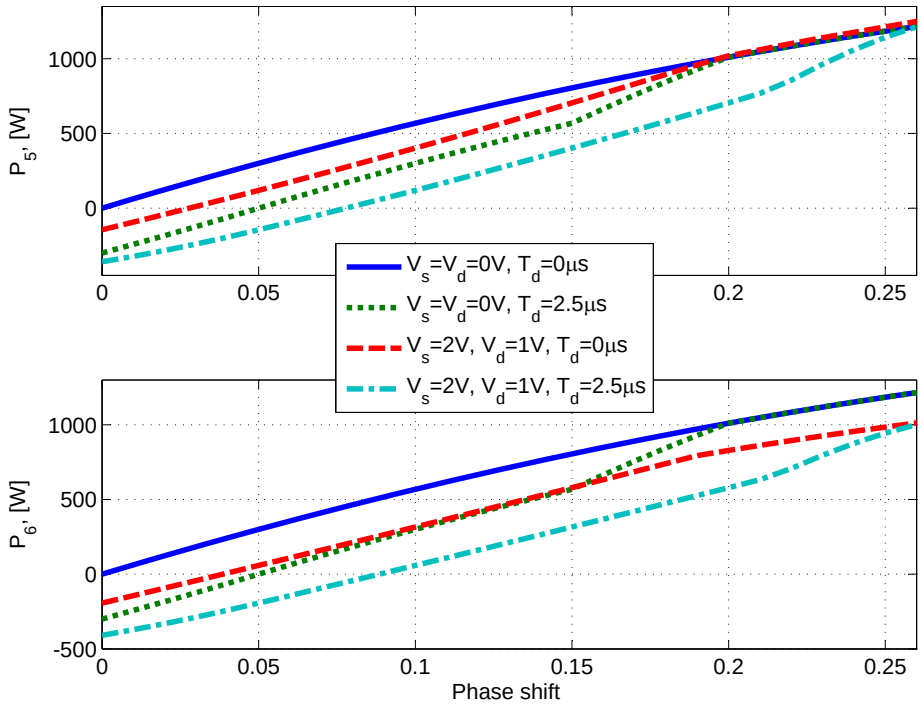

Figure 4.14: The minor parameters impact on power flow characteristics for $V_{sc} = 30V$ and $\beta_3 \in [0, 0.26]$.

Fig.4.14 compares the effect of the minor parameters for $V_{sc} = 30V$, $V_o = 80V$, $V_s = 2V$, $V_d = 1V$ and $0 \leq \beta_3 \leq 0.26$ ($0 \leq P_6 \leq 1000W$). It is obvious that the dead time effect is more significant than the one of the voltage loss for P_5 model. For P_6 model, the dead time effect is more prominent than the voltage loss for $\beta_3 < 0.152$ while the voltage loss is more significant than the dead time for $0.152 \leq \beta_3 \leq 0.26$. The voltage loss affects power flow for $\beta_3 \in [0, 1]$ while the dead time only influences

power flow for small phase shift β_3. Therefore, if we only consider the voltage loss, the power curves for both P_5 and P_6 converge to the curves with nonzero minor parameters. If we only consider the dead time, the power curves for both P_5 and P_6 converge to the curves with zero minor parameters.

To verify the effectiveness of the power flow model, experimental validation results will be presented in the next section.

4.5 Experimental Validation

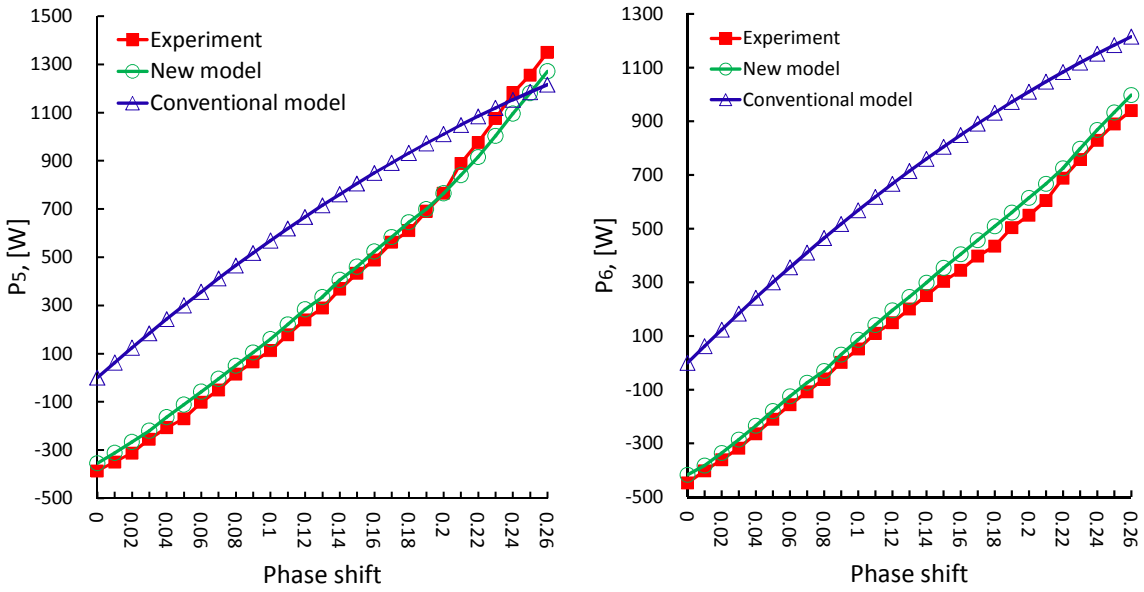

(a) P_5 (b) P_6

Figure 4.15: Power flow curve for $V_{sc} = 30V$.

Fig.4.15a shows the power curve of P_5 *vs.* β_3, while Fig.4.15b demonstrates the power curve of P_6 *vs.* β_3 for the DAB converter operating at $V_{sc} = 30V$ and $V_o = 80V$. The experimental results validate the new power flow equation while the conventional power flow equation (characterized by the conventional model) shows significant error.

Moreover, new characteristics *Reversed Power Flow* and *Energy Sink* captured by the new power flow model are also explicitly confirmed.

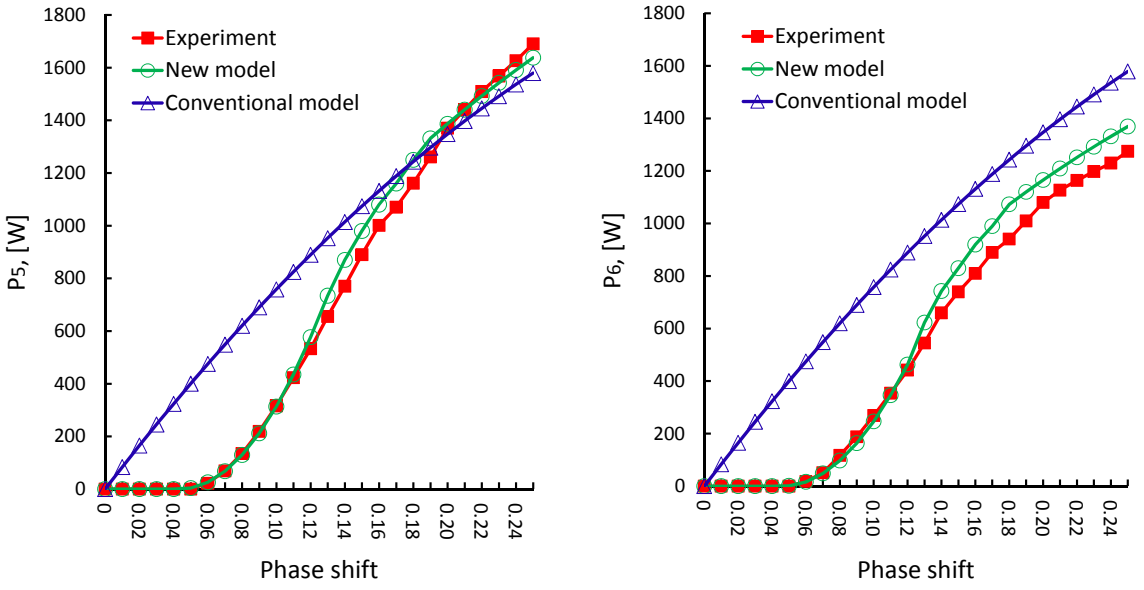

(a) P_5 (b) P_6

Figure 4.16: Power flow curve for $V_{sc} = 40V$.

Fig.4.16 demonstrates the power curve of the DAB converter operating at $V_{sc} = 40V$ and $V_o = 80V$. For this case, the DAB converter works at Region D for $0 \leq \beta_3 \leq 0.05$ and Region E for $0.05 \leq \beta_3 \leq 0.12$, respectively. The new power flow model is much more accurate than the traditional power flow equation (characterized by the conventional model) because the minor parameters significantly affect the power flow of the DAB converter for these two regions. Note that there is no power transfer when $0 \leq \beta_3 \leq 0.05$ (Region D) for the reason as stated in Section IV. Once $\beta_3 > 0.12$, the DAB converter operates at Region F (no phase drift). At this region, P_6 calculated by the conventional model is larger than P_6 but smaller than P_5 given by the new model. Therefore, the conventional power flow equation is a good approximation in this region although the new model is still more accurate than the conventional one

over a wide range of operating conditions.

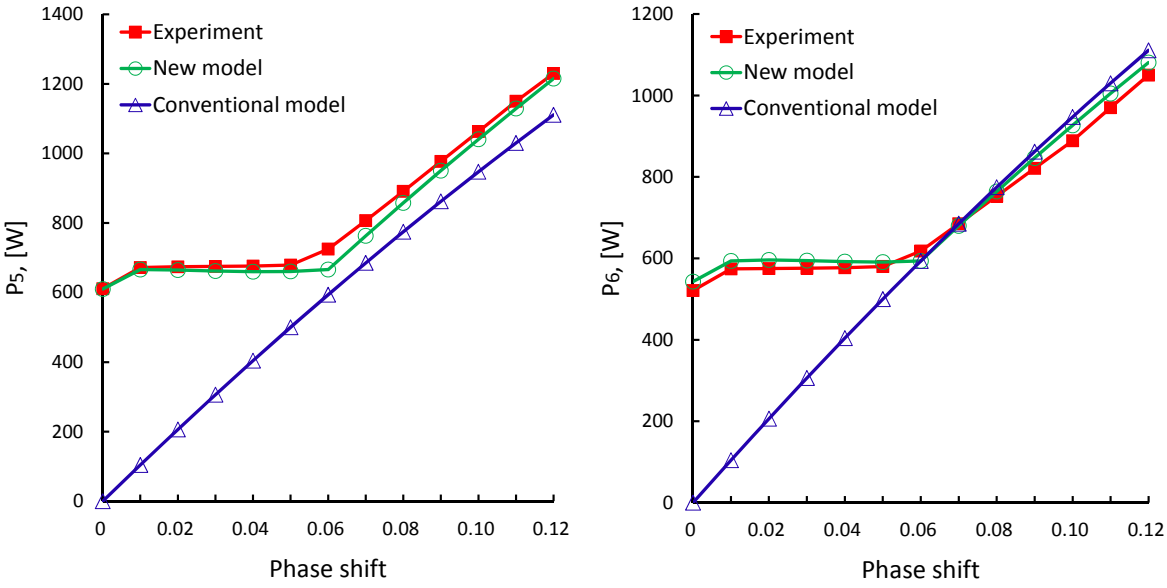

(a) P_5 (b) P_6

Figure 4.17: Power flow curve for $V_{sc} = 50V$.

Fig.4.17 shows the power curve of the DAB converter operating at $V_{sc} = 50V$ and $V_o = 80V$. For this case, the DAB converter works at Region G for $0 \leq \beta_3 \leq 0.05$ and Region H for $\beta_3 > 0.05$, respectively. The new power flow model is much more accurate than the traditional power flow equation (characterized by the conventional model) in Region G because of the significant impact of the minor parameters. In Region H, the new model is still more accurate than the conventional one although the latter is also a good approximation at this region.

Together with the validation results for the internal power transfer phenomenon presented in Section 4.3, we can draw the conclusion that the new power flow model is much more accurate than the conventional power flow model. The remaining difference between the new model predictions and the experiment results are likely due to unmodeled physical phenomena and modeled parameters uncertainties, that could be a target of future investigation.

4.6 Summary

This chapter presents a new power flow model for a DABC over a wide operating range based on in-depth short time scale process analysis. In addition to those major parameters used by conventional power flow analysis, this new model incorporates minor parameters, namely the power semiconductor voltage loss and dead time. The minor parameters are shown to be critical in explaining the observed phenomena, which are relevant to power flow characterization of the DAB converter. Therefore, the new model can serve as a research tool for optimal hardware design, operating range selection and power management strategy development. The experimental results illustrate the effectiveness of the new model.

In the process of developing the more accurate power flow characterization for the DABC, we identified the performance limitations of the converter for energy storage applications. It was also recognized that such limitations are due to the drawbacks of the modulation strategy. The subsequent effort in developing a new modulation strategy to overcome the limitations has led to a novel CM-PWM strategy described in the next Chapter.

Chapter 5

Development of a Current-Mode PWM Strategy for the Dual Active Bridge Converter

The new model developed in Chapter 4 provides more insight on the operation of the DABC and leads to the development of a Current-Mode PWM (CM-PWM) strategy proposed in this chapter. The new modulation strategy overcomes the drawbacks of the PSM strategy and improves the performance of the DABC for energy storage applications. The characteristics of the new strategy are analyzed, followed by experimental results that confirm the superior performance of the dual active converter modulated by the proposed new modulation strategy.

5.1 CM-PWM Strategy

To overcome the drawbacks of the DAB converter modulated by PSM, we propose the CM-PWM to achieve several goals, namely zero circulating current, soft-switching over a wide operating range, zero idling power, simple but accurate power flow characterization, and high power density but low component stress. Note that, given the symmetric structure of the DAB converter, the analysis and derivation are essentially

the same for both the boost and the buck direction. For conciseness, we only present the analysis and derivation for the boost direction. We now describe the CM-PWM in detail.

The modulation mechanism is demonstrated in Fig.5.1(a) while the ideal waveforms are shown in Fig.5.1(b). We define $\beta_3 \in [0, 1]$ as the pulse width of the inductor current, and $\alpha_1\beta_3$ and $\alpha_2\beta_3$ as the duty ratios for V_{ac5} and V_{ac6}, respectively. Note that since the voltage drops on the power semiconductor are relatively small in comparison with V_{sc} and V_o, $V_{ac5} \simeq V_{sc}$ and $V_{ac6} \simeq V_o$. To achieve zero current at both $t = t_0$ and $t = t_0 + \frac{\beta_3 T}{2} = t_3$, by the voltage-second balance equation for the inductor, it is easy to derive that

$$\alpha_1 = m\alpha_2. \tag{5.1}$$

where

$$m = \frac{V_o}{n_3 V_{sc}}. \tag{5.2}$$

Given the ideal waveforms shown in Fig.5.1(b), we have

$$i_5(t) = \begin{cases} i_{L3}(t), \ t \in [t_0, t_2]; \\ 0, \ t \in [t_2, t_4]. \end{cases} \tag{5.3}$$

$$i_6(t) = \begin{cases} 0, \ t \in [t_0, t_1]; \\ \frac{i_{L3}(t)}{n_3}, \ t \in [t_1, t_3]; \\ 0, \ t \in [t_3, t_4]. \end{cases} \tag{5.4}$$

By enforcing the pulse width constraint (7.2), we have $i_{L3}(t_0) = 0$ and $i_{L3}(t_3) = 0$. Therefore, Zero Current Switching (ZCS) at $t = t_0$ and $t = t_3$ are achieved. Moreover,

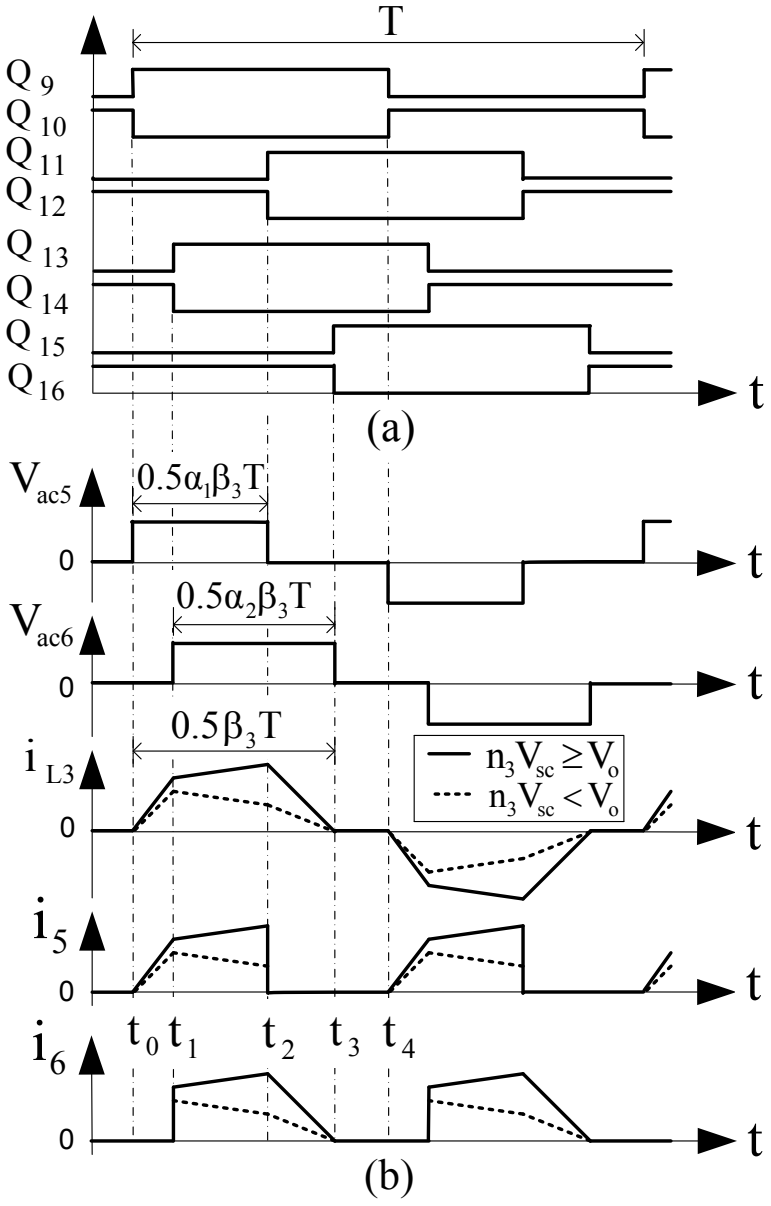

Figure 5.1: CM-PWM of the DAB converter (a) modulation sequence; (b) ideal waveforms.

$i_5(t) \geq 0$ and $i_6(t) \geq 0$ for $t \in [t_0, t_0 + \frac{T}{2}]$, meaning that the circulating current is eliminated.

Generally, the dynamics of V_{sc} and V_o are much slower than that of i_{L3}, thus one can assume that V_{sc} and V_o are constant over a switching period. Therefore, the average output power P_6 can be calculated as:

$$\begin{aligned} P_6 &= \frac{2}{T}\int_0^{T/2} V_{sc} i_5(t)\, dt = \frac{2}{T}\int_0^{T/2} V_o i_6(t)\, dt \\ &= \frac{V_o}{n_3}\left\{(i_{L3}(t_1) + i_{L3}(t_2))(t_2 - t_1) + i_{L3}(t_2)(t_3 - t_2)\right\}. \end{aligned} \tag{5.5}$$

Substituting

$$i_{L3}(t_1) = \frac{V_{sc}(1-\alpha_2)\beta_3 T}{2L_3}, \tag{5.6}$$

$$i_{L3}(t_2) = \frac{V_o(1-\alpha_1)\beta_3 T}{2n_3 L_3}, \tag{5.7}$$

$$t_2 - t_1 = \frac{(\alpha_1 + \alpha_2 - 1)\beta_3 T}{2}, \tag{5.8}$$

$$t_3 - t_2 = \frac{(1-\alpha_1)\beta_3 T}{2}, \tag{5.9}$$

into (5.5) yields

$$P_6 = \frac{\beta_3^2 V_{sc} V_o T}{4n_3 L_3}(2(1+m)\alpha_2 - (1+m+m^2)\alpha_2^2 - 1). \tag{5.10}$$

To achieve maximum output power, let

$$\frac{\partial P_6}{\partial \alpha_2} = 2(1+m) - 2(1+m+m^2)\alpha_2 = 0. \tag{5.11}$$

Equation (5.11) leads to:

$$\alpha_2 = \frac{1+m}{1+m+m^2}. \tag{5.12}$$

Given (7.2) and (5.12), we have:

$$\alpha_1 = \frac{m^2+m}{1+m+m^2}. \tag{5.13}$$

Therefore, for a given inductor current pulse width β_3, if duty ratio constraints α_1 and α_2, specified by (5.12) and (5.13), are applied to control the pulse width of V_{ac5} and V_{ac6}, we can achieve: (1) maximum output power for the converter with CM-PWM; (2) ZCS at $t = t_0$ and $t = t_3$; and (3) zero circulating current. For the DAB converter modulated by CM-PWM, the characteristics will be analyzed in the next section.

5.2 Power Converter Characteristics of DABC with CM-PWM

To understand the steady state characteristics of the DAB converter with CM-PWM, we analyze operation first in this section. The goal of this analysis is to obtain the power, current and switching characteristics of the power converters.

5.2.1 Power Flow Calculation

For the DAB converter modulated by the CM-PWM, the output power can be calculated by substituting (5.12) into (5.10) as:

$$P_6 = \frac{\beta_3^2 V_{sc}^2 V_o^2 T}{4L_3(n_3^2 V_{sc}^2 + n_3 V_{sc} V_o + V_o^2)}. \tag{5.14}$$

Therefore, zero idling power is achievable by enforcing $\beta_3 = 0$. Given (6.4), the maximum output power can be derived as

$$P_{6max} = \frac{V_{sc}^2 V_o^2 T}{4L_3(n_3^2 V_{sc}^2 + n_3 V_{sc} V_o + V_o^2)}. \tag{5.15}$$

If the DAB converter is modulated by PSM, the output power [54] is:

$$P_6' = \frac{T V_{sc} V_o \beta_3 (1 - \beta_3)}{2 n_3 L_3'}. \tag{5.16}$$

The maximum output power is:

$$P_{6max}' = \frac{T V_{sc} V_o}{8 n_3 L_3'}. \tag{5.17}$$

Moreover, with the same inductor ($L_3 = L_3'$),

$$\frac{P_{6max}}{P_{6max}'} = \frac{2 n_3 V_{sc} V_o}{n_3^2 V_{sc}^2 + n_3 V_{sc} V_o + V_o^2} \leq \frac{2}{3}. \tag{5.18}$$

This suggests that, with the same inductor, the maximum output power of the DAB converter modulated by CM-PWM is less than that of the converter modulated by PSM.

5.2.2 Current Stress

Given the inductor current shape shown in Fig.5.1, if the DAB converter is modulated with CM-PWM, the inductor peak current i_{pk} can be calculated as:

$$i_{pk} = \begin{cases} i_{L3}(t_1) = \frac{V_{sc}(1-\alpha_2)\beta_3 T}{2L}, for\ n_3 V_{sc} \leq V_o; \\ \\ i_{L3}(t_2) = \frac{V_o(1-\alpha_1)\beta_3 T}{2nL}, for\ n_3 V_{sc} > V_o. \end{cases} \tag{5.19}$$

By (5.19), when $\beta_3 = 1$, the DAB converter with CM-PWM delivers maximum output power for given V_{sc} and V_o. Under this condition, the maximum peak current i_{pkmax} is:

$$i_{pkmax} = \begin{cases} i_{L3}(t_1) = \frac{V_{sc}(1-\alpha_2)T}{2L_3}, for\ n_3 V_{sc} \leq V_o; \\ \\ i_{L3}(t_2) = \frac{V_o(1-\alpha_1)T}{2n_3 L_3}, for\ n_3 V_{sc} > V_o. \end{cases} \tag{5.20}$$

For the DAB converter modulated with PSM, the inductor peak current is:

$$i'_{pk} = \begin{cases} i_{L3}(t_1) = \frac{T(V_o - n_3 V_{sc} + 2n_3 V_{sc}\beta)}{4n_3 L'_3}, for\ n_3 V_{sc} \leq V_o; \\ \\ i_{L3}(t_2) = \frac{T(n_3 V_{sc} - V_o + 2V_o\beta)}{4n_3 L'_3}, for\ n_3 V_{sc} > V_o. \end{cases} \tag{5.21}$$

According to (5.16), if $\beta_3 = 0.5$, the DAB converter delivers maximum output power which introduces the maximum peak current:

$$i'_{pkmax} = \begin{cases} i_{L3}(t_1) = \frac{TV_o}{4n_3 L'_3}, for\ n_3 V_{sc} \leq V_o; \\ \\ i_{L3}(t_2) = \frac{Tn_3 V_{sc}}{4n_3 L'_3}, for\ n_3 V_{sc} > V_o. \end{cases} \tag{5.22}$$

If we choose

$$L_3 = \frac{2n_3 V_{sc} V_o L_3'}{n_3^2 V_{sc}^2 + n_3 V_{sc} V_o + V_o^2} < L_3'. \tag{5.23}$$

Then $i_{pkmax} = i'_{pkmax}$ and $P_{6max} = P'_{6max}$. Therefore, the power density of a DAB converter with CW-PWM can be designed the same as that of a DAB converter with PSM under the same component stress.

5.2.3 Soft-Switching Range

It is known that the switching loss will be minimized if the power converter operates with soft switching commutation. Therefore, it is desirable to understand the switching characteristics of the DAB converter with CM-PWM. Referring to Fig.5.1, using an analysis method similar to that presented in [46], the switching characteristics of the CM-PWM modulated DAB converter can be analyzed as follows:

1. $t = t_0 : Q_{10}$ turns off and Q_9 turns on. Since $i_{L3}(t_0) = 0$, Q_{10} is ZCS OFF while Q_9 is ZCS ON. After this transition, in B_1, i_{L3} passes through Q_9 and Q_{12} while in B_2, i_{L3} passes through Q_{14} and D_{16}.

2. $t = t_1 : Q_6$ turns off and Q_5 turns on. Since $i_{L3}(t_0) > 0$, Q_6 is ZVS OFF while Q_{13} is ZVS ON. After this transition, in B_1, i_{L3} passes through Q_9 and Q_{12} while in B_2, i_{L3} passes through D_{13} and D_{16}.

3. $t = t_2 : Q_{12}$ turns off and Q_{11} turns on. Since $i_{L3}(t_0) > 0$, Q_{12} is ZVS OFF while Q_{11} is ZVS ON. After this transition, in B_1, i_{L3} passes through Q_9 and D_{11} while in B_2, i_{L3} passes through D_{13} and D_{16}.

4. $t = t_3 : Q_{16}$ turns off and Q_7 turns on. Since $i_{L3}(t_0) = 0$, Q_{16} is ZCS OFF while Q_7 is ZCS ON. After this transition, Q_9 and Q_{11} in B_1 are on while Q_{13} and

Q_{15} in B_2 are on.

Therefore, ZCS/ZVS over the first half switching period is achieved. Similarly, ZCS/ZVS is also achievable over the second half switching period ($t \in [t_4, t_4 + \frac{T}{2}]$).

Remark 7 *Combining the conclusion from the previous section, we can summarize the following features achieved by the CM-PWM strategy:*

1. *zero circulating current that reduces conduction loss;*
2. *ZCS/ZVS over a wide operating range to minimize switching loss;*
3. *zero idling power to eliminate idle loss;*
4. *simple power flow characterization;*
5. *the same power density under the same current stress as the DAB converter with PSM.*

Therefore, the proposed CM-PWM strategy can improve the performance of the DAB converter over a wide operating range without compromising power density.

5.3 Experimental Validation

Fig.5.2 shows the experimental waveforms of the DAB converter with CM-PWM for $V_{sc} = 40V$, $V_o = 100V$ and $\beta_3 = 0.8$. The inductor current increases from zero to its maximum and then decreases to zero at the end of $\frac{\beta_3 T}{2}$. This confirms that ZCS/ZVS is achieved.

Fig.5.3 compares the calculated power flow curves using (6.4) and the measured power flow curves of the DAB converter with CM-PWM. The calculated curves match the measured curves very well, indicating the accuracy of the simple power flow equation (6.4) and the controllability of the output power between zero and its maximum.

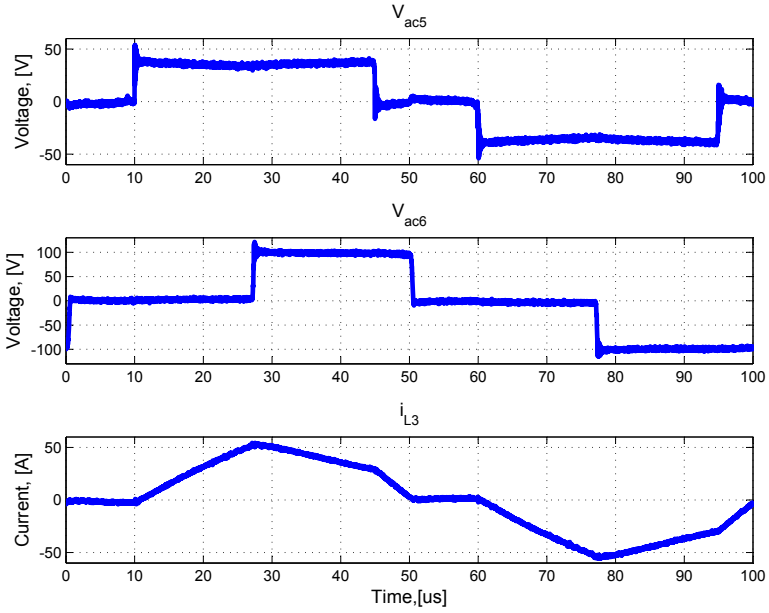

Figure 5.2: Experimental waveforms for $V_{sc} = 40$, $V_o = 100$ and $\beta_3 = 0.8$.

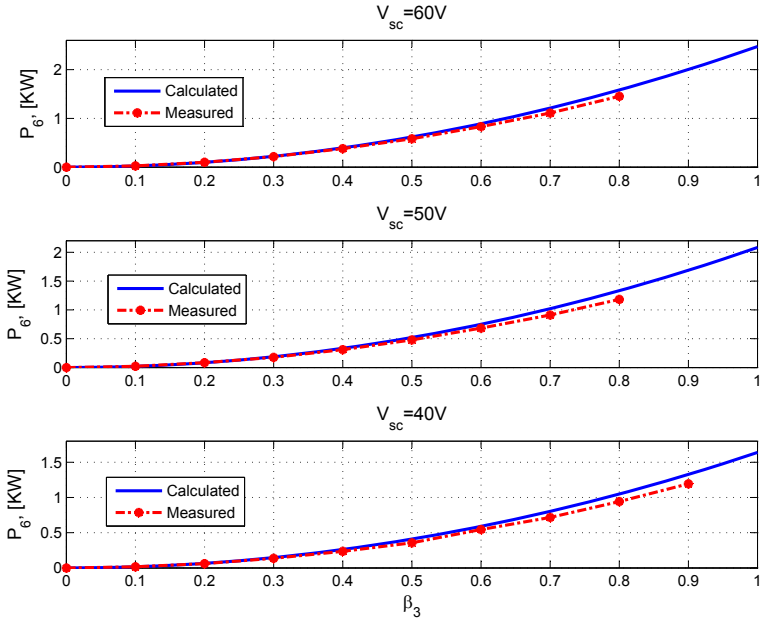

Figure 5.3: Power flow curves for $V_o = 100$.

Moreover, $P_5 = P_6 = 0$ and $i_{L3} = 0$ for $\beta_3 = 0$. Therefore, the idling power consumption of the DAB converter is eliminated.

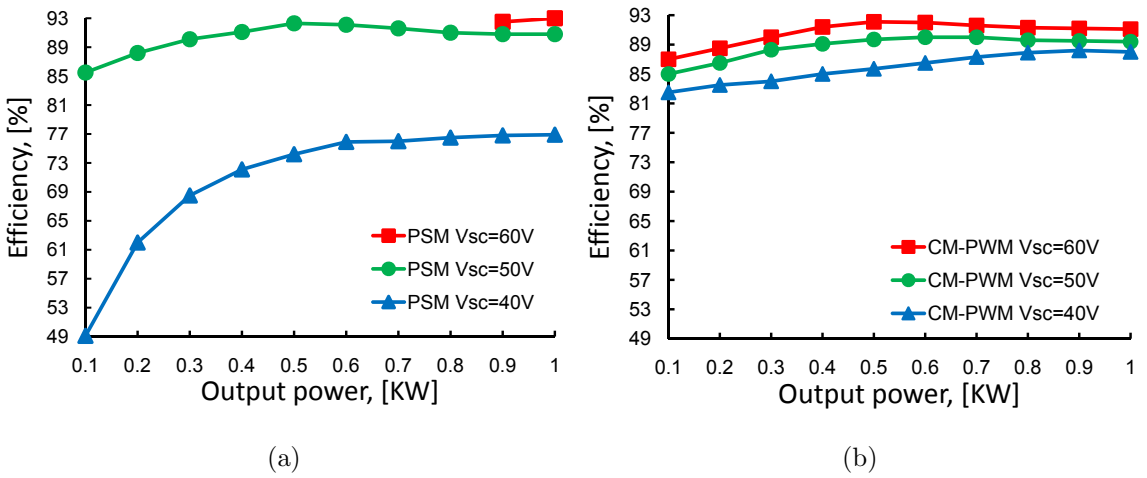

(a) (b)

Figure 5.4: The efficiency curves of the DAB converter: (a) with PSM; (b) with CM-PWM.

Fig.5.4a shows the efficiency curves of the DAB converter modulated by PSM while Fig.5.4b shows the efficiency curves of the DAB converter modulated by CM-PWM. For $V_{sc} = 40V$ and $V_o = 100V$ ($n_3 V_{sc} < V_o$), the efficiency of the DAB converter modulated by the proposed CM-PWM is much higher than that of the DAB converter modulated by the proposed PSM. This is because the CM-PWM eliminates the circulating energy and achieves ZCS/ZVS for the entire operating region.

5.4 Summary

In this chapter, a current-mode PWM modulation strategy for the DAB converter is proposed. In comparison to the conventional phase shift modulation strategy, the current-mode PWM proposed in this dissertation can achieve zero circulating current, soft-switching over the full operating range, zero idling power consumption,

wide range of controllability of output power, and simple and accurate power flow characterization. Moreover, the proposed modulation strategy enables the converter to achieve the same power density under the same current stress as the converter with conventional PSM. Therefore, the CM-PWM strategy enables us to achieve optimal power management of the DABC. The power management control algorithm for the entire DHPS will be presented in the next section.

Chapter 6

Experimental Validation of the DHPS

As discussed in Chapter 1, the DC Hybrid Power System (DHPS) typically requires an advanced power management algorithm to assure safe, reliable and effective operation of the system. Fig.6.1 shows the configuration of the power management scheme of the DHPS which has three power converters as power management actuators. The top level power management algorithm computes the desired output power P_{o1}^*, P_{o2}^* and P_{o3}^* while the power converter controllers calculate the control inputs β_1, β_2 and β_3 for the three power converters. Then, the modulation strategies translate the control inputs β_1, β_2 and β_3 into 16 channels of pulse signals to control DC/DC1, DC/DC2 and DC/DC3, respectively, where DC/DC1 and DC/DC2 are the unidirectional Full Bridge Converters (FBC) while DC/DC3 is the bidirectional Dual Active Bridge Converter (DABC).

As the power conditioning devices, the FBCs and DABC are the actuators to address power management problems for the DHPS. As presented in Chapter 4, there are several phenomena that deteriorate the performance of the DABC for energy storage system applications. The new model developed in Chapter 4, provides more insight on the operation of the DABC and leads to the development of a Current-Mode

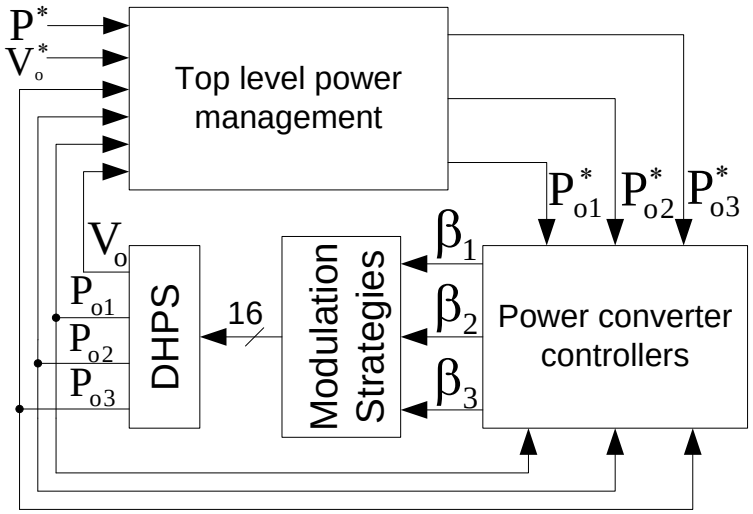

Figure 6.1: Configuration of the DHPS control scheme.

PWM (CM-PWM) strategy proposed in Chapter 5. The new modulation strategy overcomes the drawbacks of the PSM strategy and improves the performance of the DABC for energy storage applications. Assuming: (1) the FBCs are modulated with the phase shift strategy while the DABC is modulated with the CM-PWM strategy; and (2) the optimal desired output powers P_{o1}^*, P_{o2}^* and P_{o3}^* for the three power converters are given by the top level optimal power planner which is beyond the scope of this dissertation, a power converter controller is developed to track the optimal output power profile for each power converter in this chapter.

6.1 Power Converter Controller Development

For the DHPS under investigation, there are two FBCs which are almost identical. Fig.6.2 shows the configuration of the power converter controller for DC/DC1 (FBC). First, a feedforward controller is designed to achieve quick response. As discussed in [99], neglecting the power losses and minor parameter effects, the average output

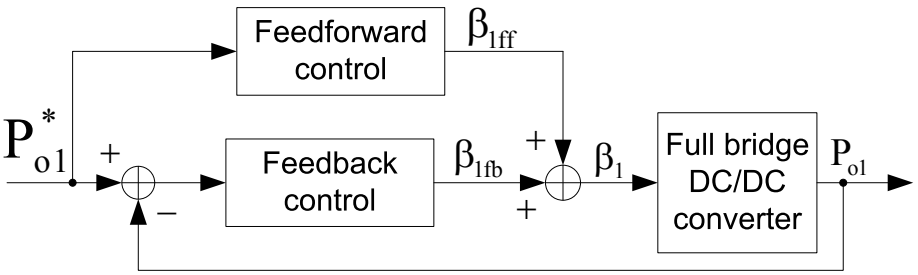

Figure 6.2: Configuration of the power management control scheme for a FBC.

power over the half switching cycle is

$$P_{o1} = \frac{\beta_1^2 T V_1 (n_1 V_1 - V_o)}{4 n_1 L_1}. \tag{6.1}$$

As a power converter with $10kHz$ switching frequency, the time constant of the FBC is at the millisecond level. Given that the time constant for a typical power system such as a fuel cell power system is about several seconds, there is a significant time scale separation between the dynamics of the power source and the power converter. This fact suggests that we can assume that the input voltage V_1 is constant over several switching periods. Moreover, we assume that the DC bus voltage V_o is regulated to V_o^* by the top level power management algorithm. Therefore, by substituting $P_{o1} = P_{o1}^*$ and $V_o = V_o^*$ into (6.1), a feedforward controller can be derived to drive the FBC to track P_{o1}^* given by the top level power management algorithm. The nonlinear feedforward controller can be expressed as:

$$\beta_{1ff} = \sqrt{\frac{4 n_1 L_1 P_{o1}^*}{T V_1 (n_1 V_1 - V_o^*)}}, \tag{6.2}$$

where $n_1 V_1 - V_o^* > 0$ since the FBC is an isolated buck converter.

The power flow model given by (6.1) neglects the minor parameter effects such as that of the dead time and neglects losses on the transformer, power semiconductors

and auxiliary circuitry. Therefore, a feedback control loop is designed to eliminate the steady error introduced by the modeling uncertainties:

$$\beta_{1fb} = \frac{K_{p1}s + K_{i1}}{s}(P_{o1}^{*} - P_{o1}), \tag{6.3}$$

where K_{p1} and K_{i1} are the proportional and integral gains, respectively, which can be chosen using criterions described in [107].

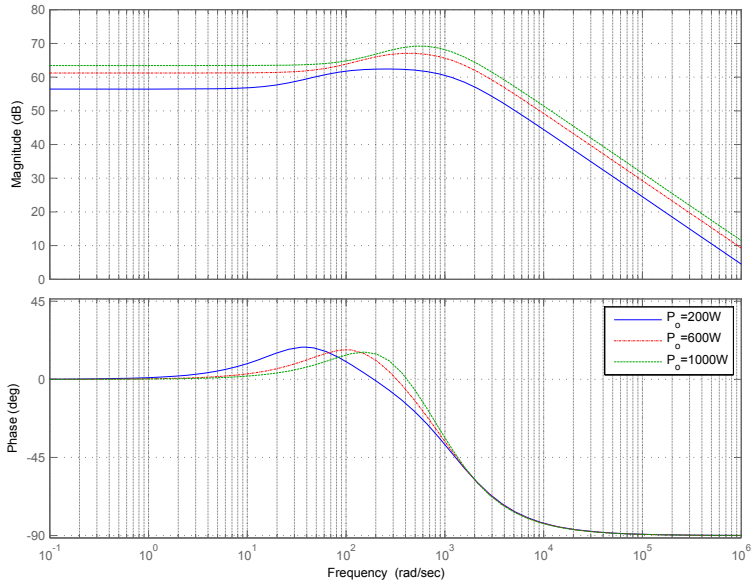

Figure 6.3: Open-loop Bode plot of the FBC at different values of output power.

For the FBC, an averaged dynamic model was developed in [99]. We can linearize the model and obtain the plant transfer function from phase shift to output power $G_{p\beta}(s)$ at different values of output power. Fig.6.3 shows the open loop Bode plots of the FBC for $P_o = 200, 600, \text{and } 1000W$, respectively. These plots illustrate that the frequency responses of the FBC are similar for different values of output power. Therefore, we can try to design one pair of K_{p1} and K_{i1} for the entire operating range.

Since the sampling time of the control system and the switching period of the FBC are $100\mu s$, the frequency of the ripple current and voltage is $20kHz$. On one

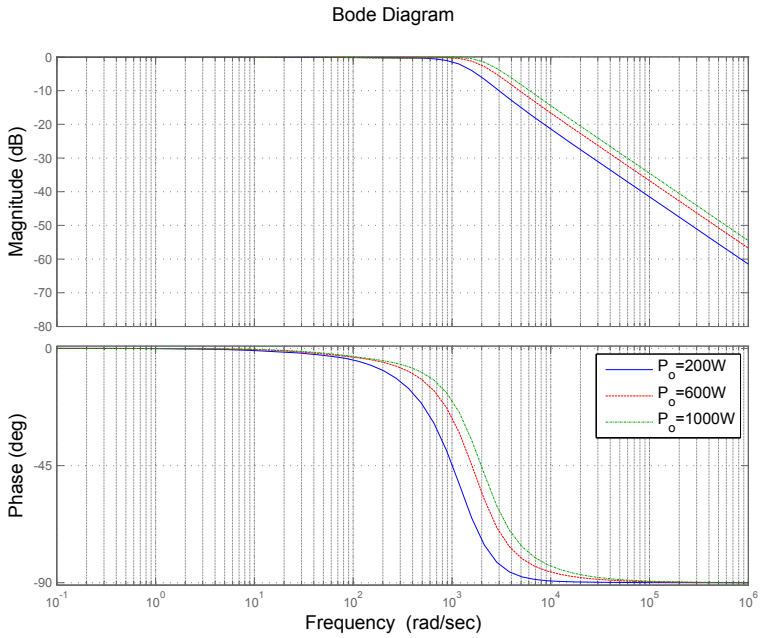

Figure 6.4: Closed-loop Bode plot of the FBC at different values of output power.

hand, it is desirable for the closed loop system to have a high bandwidth to achieve fast response. On the other hand, the bandwidth shouldn't be too high. Otherwise, the ripple noise will be propagated back to the closed loop system, imposing high component stress for the FBC. Therefore, we chose a $1kHz - 2kHz$ bandwidth for the closed loop system. Fig.6.4 demonstrates the closed loop frequency responses of the FBC for $K_{p1} = 0.0001$ and $K_{i1} = 0.3$ at different values of output power. These plots verify that the closed loop frequency response meet with the above criterions. Note that, for the DC/DC1, the control input is $\beta_1 = \beta_{1ff} + \beta_{1fb}$. Since DC/DC2 is also a FBC, the controller can be designed in the same manner.

For a DABC modulated with CM-PWM strategy, as discussed in Chapter 5, the average output power over the half switching cycle is

$$P_{o3} = \frac{\beta_3^2 V_{es}^2 V_o^2 T}{4L_3(n_3^2 V_{es}^2 + n_3 V_{es} V_o + V_o^2)}. \tag{6.4}$$

Note that the time constant of the DABC is at the millisecond level which is much smaller than that of the energy storage bank (about several seconds). The significant time scale separation suggests that we can assume that the output voltage of the energy storage bank V_{es} is constant over several switching periods. Therefore, for P_{o3}^* given by the top level power management algorithm, the nonlinear feedforward controller for the DABC can be expressed as:

$$\beta_{3ff} = \sqrt{\frac{4L_3(n_3^2 V_{es}^2 + n_3 V_{es} V_o^* + V_o^{*2})P_{o3}^*}{V_{es}^2 V_o^{*2} T}}. \tag{6.5}$$

Similarly, to eliminate steady tracking error introduced by the modeling uncertainties, a feedback control loop is designed as:

$$\beta_{3fb} = \frac{K_{p3}s + K_{i3}}{s}(P_{o3}^* - P_{o3}), \tag{6.6}$$

where K_{p3} is the proportional gain while K_{i3} is the integral gain.

For the DHPS under investigation, the energy storage bank voltage $V_{es} \in [35V, 75V]$ and output power $P_o \in [-500W, 500W]$. Fig.6.5 shows the open loop Bode plots of the DABC on the discharging mode for $P_o = 100, 300, \text{and } 500W$ at $V_{es} = 40V$ and $V_{es} = 70V$, respectively. Note that given the symmetric structure of the DABC, the frequency response on the charging mode is similar to that of the discharging mode. These plots illustrate that the frequency responses of the DABC are similar for different values of input voltage and output power. Therefore, we can try to design one pair of K_{p3} and K_{i3} for the entire operating range.

Similar to the FBC, we chose a $1kHz - 2kHz$ bandwidth for the closed loop system of the DABC. Fig.6.6 demonstrates the closed loop frequency responses of the DABC for $K_{p1} = 0.0002$ and $K_{i1} = 0.8$ at different values of input voltage and output power.

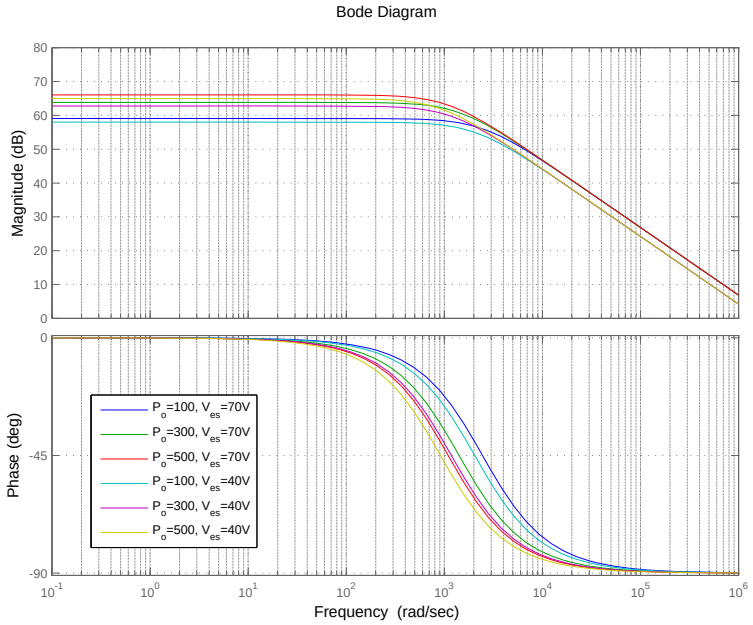

Figure 6.5: Open-loop Bode plot of the DABC at different values of input voltage and output power.

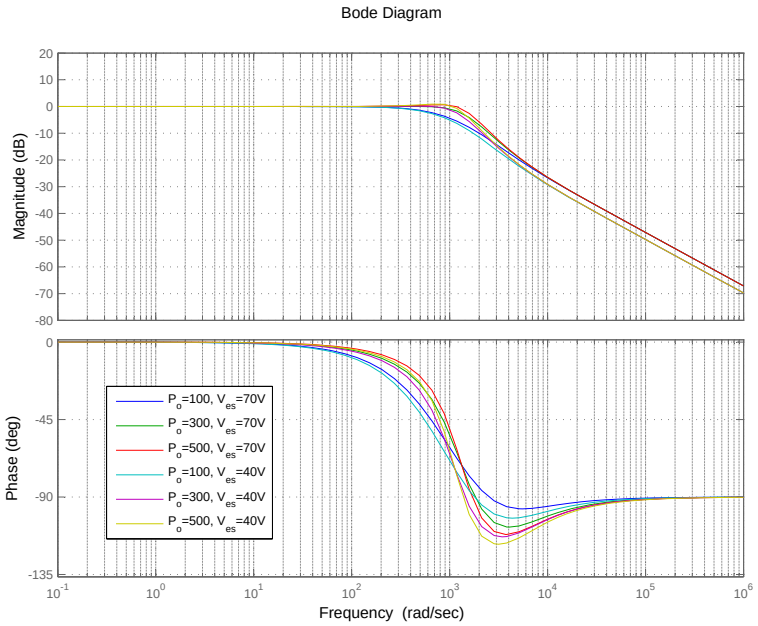

Figure 6.6: Closed-loop Bode plot of the DABC at different values of input voltage and output power.

These plots verify that the closed loop frequency response meet with the criterion.

Table6.1 summarizes the gains for the feedback controller of the three power converters.

Table 6.1: Feedback control gains of the power converters

	DC/DC1	DC/DC2	DC/DC3
K_p	0.0001	0.0001	0.0002
K_i	0.3	0.3	0.8

6.2 Experimental Results

The power converter control algorithm is implemented on the DHPS testbed described in Chapter 2. Suppose that there is a top level optimal power management algorithm to calculate the power profile for each power converter, the goal of this section is to verify whether the controller can quickly and accurately track the power profile for each power converter during both the charging and discharging modes of the energy storage system.

Fig.6.7 shows the experimental results of the charging mode when there is a step change for the power demands P_{o1}^* and P_{o2}^* while there is a constant $-400W$ power P_{o3} charging the energy storage bank. Both the power converters DC/DC1 and DC/DC2 track their power demands P_{o1}^* and P_{o2}^* with the milliseconds level settling time while only a small deviation for the P_{o3} is observed.

Fig.6.8 presents the experimental results in the presence of a step change for the power demand P_{o3}^*. Initial P_{o3}^* is $-400W$. A step-down change of the power demand P_{o3}^* is then applied to command the bidirectional DABC operating with the idling mode ($0W$ input/output power). Meanwhile, the output power of both DC/DC1 and DC/DC2 are reduced.

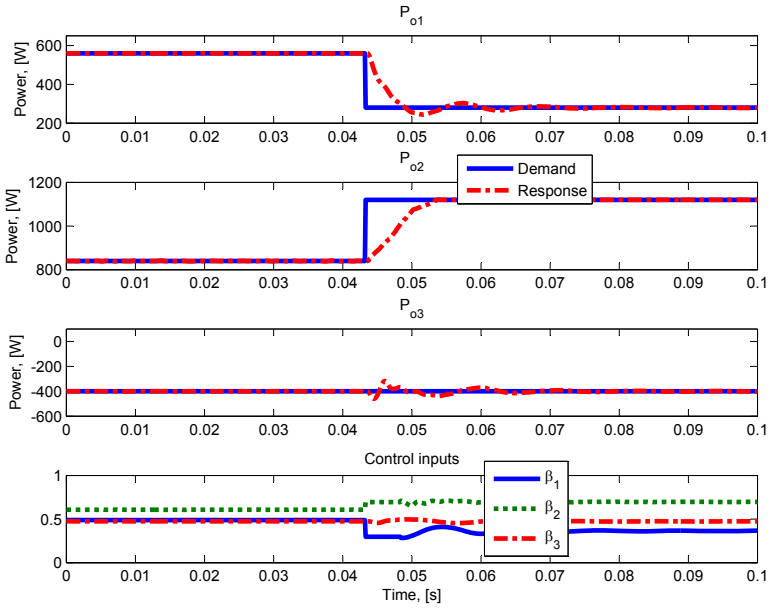

Figure 6.7: Experimental results of constant power charging mode.

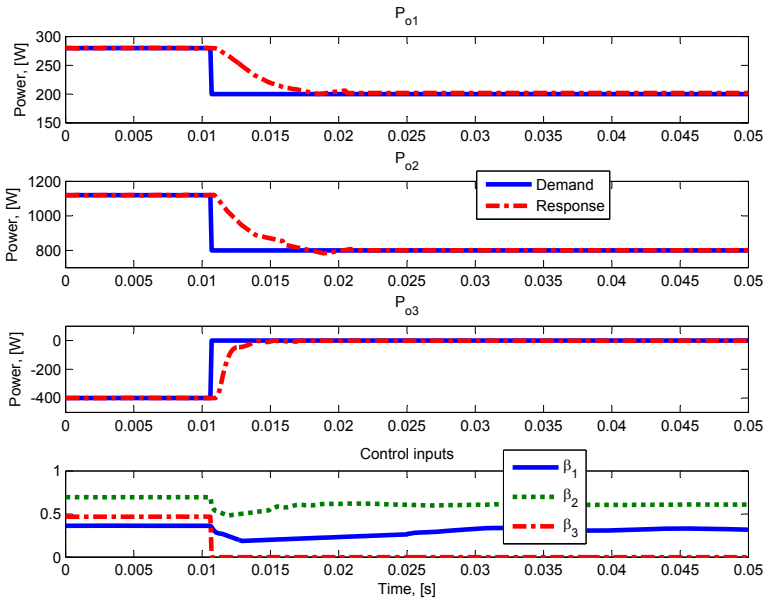

Figure 6.8: Experimental results of step-change power charging mode.

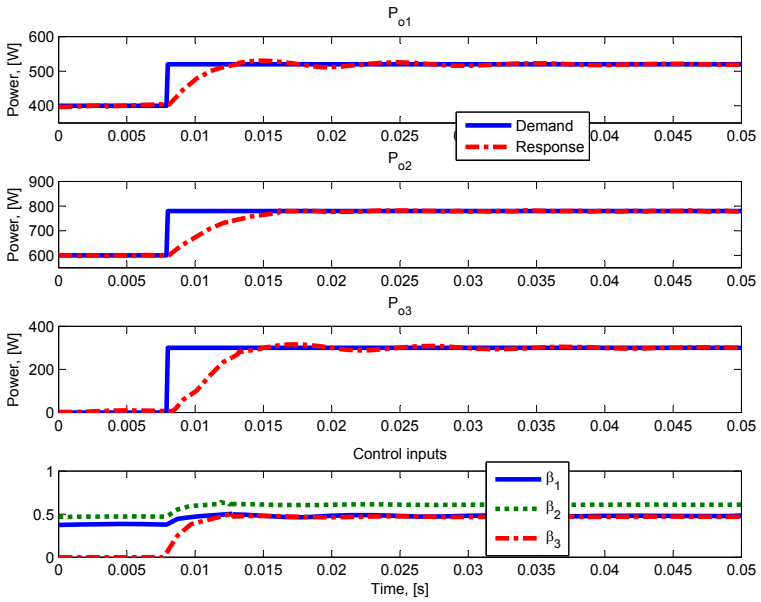

Figure 6.9: Experimental results of step-change power discharging mode.

Fig.6.9 demonstrates the experimental results for the DABC operating with the discharging mode. Initial P_{o3}^{*} is $0W$. The experimental results shows that both P_{in3} and P_{o3} are zero for the DABC operating with the idling mode. A step-up change of the power demand P_{o3}^{*} is then applied to command the bidirectional DABC to deliver $300W$ output power. Meanwhile, P_{o1} and P_{o2} also step up to deliver higher power. The actual output power of the two power converters tracks their corresponding power demand P_{o1}^{*} or P_{o2}^{*} closely. The experimental results verify that the output power of the three power converters can track their commands within $10ms$.

6.3 Summary

In this chapter, the power converter control algorithms for the DHPS are presented. These algorithms are designed to track the power profile provided by the optimal power planner. The experimental results reveal that, if the DABC is modulated by the CM-PWM strategy, the power converters track the power profiles quickly

and closely.

Although the experimental results verified the effectiveness of the controllers, it is a more challenging control problem to achieve control objectives without violating the physical constraints of the power converters. The MPC scheme which can be used to effectively handle constraints will be applied to a FBC in the next chapter.

Chapter 7

Model Predictive Control of the Full Bridge Converter

Motivated by the challenges of power converter control and recent development of advanced control and optimization algorithms, this chapter investigates the MPC schemes for the Full Bridge Converter (FBC) control. The control objective is to regulate the output voltage without violating peak current constraint. Moreover, since the FBC is a highly nonlinear system with a wide operating range and fast dynamics, it is interesting to compare the closed loop performance and computational time for the linear MPC and nonlinear MPC schemes. The inductor peak current constraint of the full bridge DC/DC converter will be first presented. Then an observer design for states and parameter estimation using a large signal dynamic model is introduced. After that, the voltage regulation problem is formulated as a MPC problem using either a linear or a nonlinear model to predict the future plant behavior, while the peak current protection requirement is formulated as a nonlinear constraint. Finally, the InPA-SQP solver is interpreted, followed by experimental results that confirm the effectiveness of the proposed MPC algorithm and compare the closed loop performance and computation time of the two MPC schemes.

7.1 Inductor Peak Current Constraint

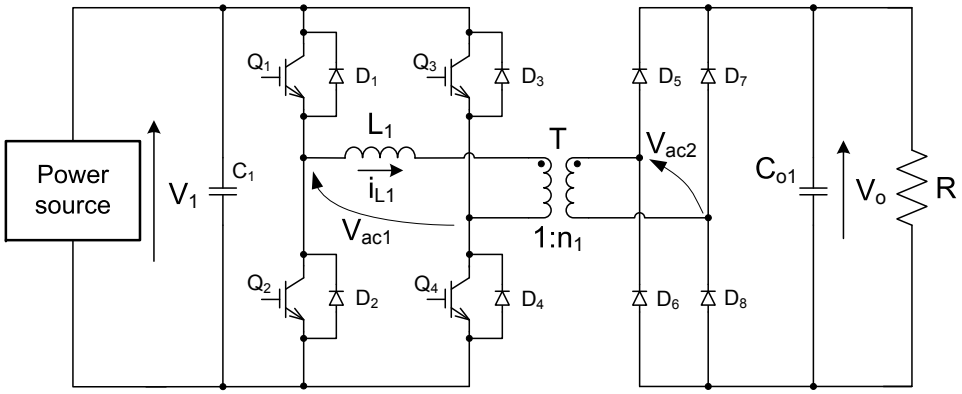

Figure 7.1: A full bridge DC/DC converter.

Fig.7.1 depicts the configuration of the power stage of a FBC, where $D_1 - D_4$ are the corresponding anti-parallel diodes of the power switches $Q_1 - Q_4$ while $D_5 - D_8$ form the output rectifier, L_1 is the leakage inductance of the transformer with turn ratio n_1, C_1 and C_{o1} are the input and output capacitor respectively, R is the load resistance, and V_1 and V_o are the input voltage and the output voltage, respectively. The AC side of each bridge is connected to the transformer with corresponding primary voltage V_{ac1} and secondary voltage V_{ac2}, respectively.

The FBC is typically modulated by the phase shift modulation signals $V_{Q_1} \sim V_{Q_4}$ shown in Fig.7.2(a) and Fig.7.3(a), where $\beta \in [0, 1]$ is the normalized phase shift between the two half bridges composed of Q_1/Q_2 and Q_3/Q_4, respectively. Note that since the parallel resistance and inductance are much greater than the series resistance and inductance, the equivalent circuit model of a high frequency transformer can be simplified as an ideal transformer with a primary series inductor (leakage inductor). Therefore, the electrical connection between V_{ac1} and V_{ac2} shown in Fig.7.1 can be expressed by the simplified diagram shown in Fig.7.4, where L is the leakage inductance. By shifting the phase between the two half bridges, different combinations of

V_{ac1} and V_{ac2} can be applied to shape the current i_{L1} and consequently to manipulate the power flow. Based on the shape of i_{L1}, there are two operation modes for the full bridge converter, namely the Discontinuous-Conduction-Mode (DCM) and the Continuous-Conduction-Mode (CCM). DCM refers to the case that the inductor current i_{L1} stays at zero for a certain period of time for each half switching cycle as shown in Fig.7.2(d). CCM means that the inductor current i_{L1} only crosses zero but never stays at zero for each half switching period as shown in Fig.7.3(d).

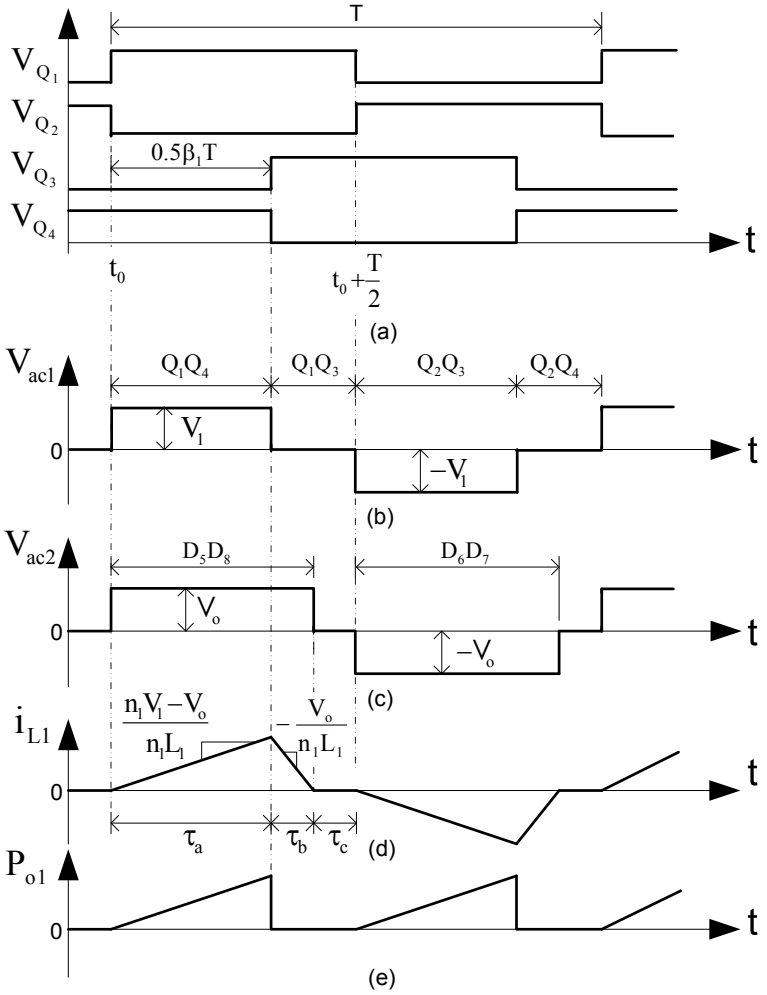

Figure 7.2: Modulation sequence and ideal waveforms of the full bridge DC/DC converter for DCM.

For a full bridge DC/DC converter operating with DCM, the ideal voltage wave-

forms of V_{ac1} and V_{ac2} are shown in Fig.7.2(b) and Fig.7.2(c). The voltage across the inductor is $V_{L1} = V_{ac1} - V_{ac2}/n_1$, leading to the ideal inductor current i_{L1} slope at each segment shown in Fig.7.2(d).

Given the inductor current slopes shown in Fig.7.2(d), the peak current ($i_{L1}(t_0 + \frac{\beta_1 T}{2})$) for DCM can be calculated as:

$$i_{L1}(t_0 + \frac{\beta_1 T}{2}) = \frac{(n_1 V_1 - V_o)\beta_1 T}{2 n_1 L_1}. \tag{7.1}$$

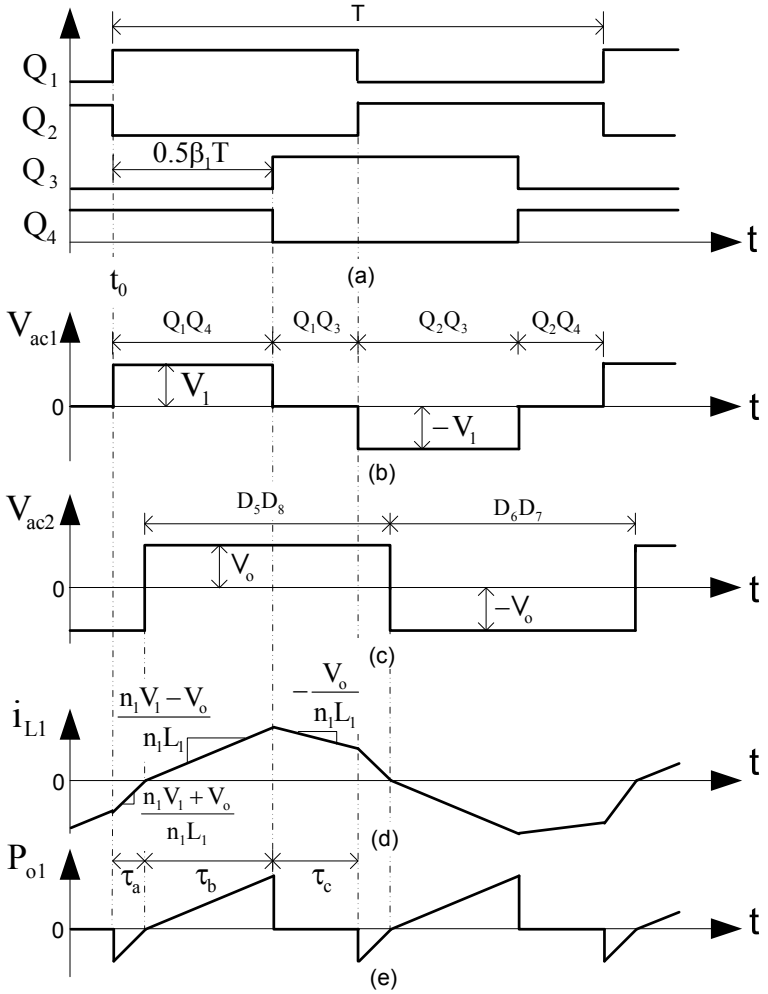

Figure 7.3: Modulation sequence and ideal waveforms of the full bridge DC/DC converter for CCM.

For a full bridge DC/DC converter operating with CCM, the voltage waveforms of V_{ac1} and V_{ac2} are shown in Fig.7.3(b) and Fig.7.3(c). The voltage across the inductor is $V_{L1} = V_{ac1} - V_{ac2}/n_1$, leading to the inductor current i_{L1} slope at each segment shown in Fig.7.3(d).

Similarly, the peak current ($i_{L1}(t_0 + \frac{\beta_1 T}{2})$) for CCM can be calculated as:

$$i_{L1}(t_0 + \frac{\beta_1 T}{2}) = \frac{(n_1 V_1 - V_o)(V_o + n_1 V_1 \beta_1)T}{8 n_1 L_1 V_1}. \tag{7.2}$$

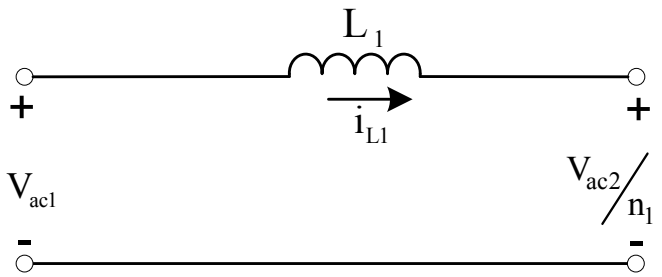

Figure 7.4: Simplified scheme of a full bridge DC/DC converter.

The operation mode of the DC/DC converter is determined by V_1, V_o and β_1. For different combinations of V_1 and V_o, the phase shift boundary line $L_{\beta_1 b}$ between the CCM and DCM can be calculated as follows if we set $\tau_c = 0$ for DCM:

$$L_{\beta_1 b} = \{(\beta_1, V_1, V_o) | \beta_1 = \frac{V_o}{n_1 V_1}\}. \tag{7.3}$$

Moreover, let i_{pk} denote the maximum tolerable peak current of the converter. Using (7.1) and (7.2), one can determine the limits on the phase shift to avoid over-peak-current. If the converter operates with CCM, the phase shift constraint curve $L_{\beta_1 c}$ can be calculated from (7.2) as follows:

$$L_{\beta_1 c} = \{(\beta_1, V_1, V_o) | \beta_1 = \frac{8 L_1 i_{pk}}{T(n_1 V_1 - V_o)} - \frac{V_o}{n_1 V_1}\}. \tag{7.4}$$

Similarly, if the converter operates with DCM, the phase shift constraint curve $L_{\beta_1 d}$ can be calculated from (7.1) as follows:

$$L_{\beta_1 d} = \{(\beta_1, V_1, V_o) | \beta_1 = \frac{2n_1 L_1 i_{pk}}{T(n_1 V_1 - V_o)}\}. \tag{7.5}$$

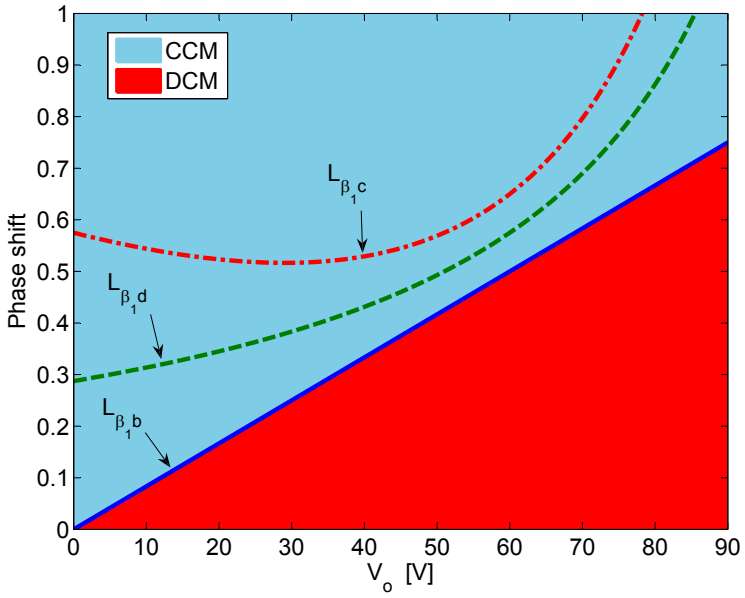

Figure 7.5: DCM/CCM boundary line $L_{\beta_1 b}$ and peak current constraint curves $L_{\beta_1 d}$ and $L_{\beta_1 c}$ for $V_1 = 60V$ and $i_{pk} = 75A$.

Fig.7.5 shows the phase shift boundary line $L_{\beta_1 b}$ and the peak current constraint curves $L_{\beta_1 d}$ and $L_{\beta_1 c}$ for $V_1 = 60V$ and $V_o = 0V \sim 90V$. Note that: (a) the full bridge DC/DC converter operates with the CCM if the phase shift is larger than the corresponding boundary value; (b) the peak current constraint curves $L_{\beta_1 d}$ and $L_{\beta_1 c}$ are calculated using equations (7.4) and (7.5) for $i_{pk} = 75A$. For our system with a nominal output power of $1000W$, the phase shift at the nominal operating point is 0.62 which is smaller than the boundary value 0.67. Therefore, the converter operates with the DCM at steady state for the nominal output power. From Fig.7.5, the DCM peak current constraint curve $L_{\beta_1 d}$ is always above the boundary line $L_{\beta_1 b}$,

so the peak current constraint will not be violated if the power converter operates with DCM at steady state. However, for the cases of starting process and overload, the power converter operates at CCM, where the CCM peak current constraint may be violated. Therefore, an active constraint enforcement mechanism needs to be incorporated to protect the converter.

7.2 Nonlinear Dynamic Model and Observer

Since the FBC is a highly nonlinear system with a wide operating range, it is desirable to employ a model based control design approach to achieve satisfactory closed loop system performance. Since the full bridge DC/DC converter has a wide operating range, it is necessary to derive a large signal dynamic model for the system to facilitate the model based control design. Using the analysis results presented in the previous section and following the same technique in [33], the dynamic model of the full bridge DC/DC converter was derived in [99] and can be written as:

$$\frac{d\bar{i}_{L1}}{dt} = \frac{\beta_1 V_1}{L_1} - \frac{4\bar{i}_{L1}\bar{V}_o}{\beta_1 T(n_1 V_1 - \bar{V}_o)}, \tag{7.6}$$

$$\frac{d\bar{V}_o}{dt} = \frac{\bar{i}_{L1}}{n_1 C_{o1}} - \frac{\bar{V}_o}{RC_{o1}}, \tag{7.7}$$

$$y = \bar{V}_o. \tag{7.8}$$

Note that: $\bar{i}_{L1}$ and $\bar{V}_o$ represent the average current and the average output voltage over a switching period.

For the dynamic system represented by (7.6)-(7.8), the implementation of advanced control strategies requires the information of the load resistance R and the average current $\bar{i}_{L1}$. The load resistance R is typically a bounded unknown parameter. However, it is necessary to estimate this parameter for the NLMPC scheme. Mean-

while, if we use a current sensor to obtain $\bar{i}_{L1}$, on the one hand, the current sensor must have high bandwidth to accurately reconstruct the current signal. On the other hand, due to electromagnetic interference, it is often necessary to use a low-pass filter to remove noise. However, a low-pass filter typically introduces additional phase lag for the closed loop system. To overcome these drawbacks, we treat the load resistance R as a state and use a nonlinear observer to estimate R and $\bar{i}_{L1}$ while keeping $\bar{V}_o$ as the only measured variable. The nonlinear observer is expressed as follows:

$$\frac{d\hat{\bar{i}}_{L1}}{dt} = \frac{\beta_1 V_1}{L_1} - \frac{4\hat{\bar{i}}_{L1}\hat{\bar{V}}_o}{\beta_1 T(n_1 V_1 - \hat{\bar{V}}_o)} + H_1(y - \hat{y}), \tag{7.9}$$

$$\frac{d\hat{\bar{V}}_o}{dt} = \frac{\hat{\bar{i}}_{L1}}{n_1 C_{o1}} - \frac{\hat{\bar{V}}_o}{RC_{o1}} + H_2(y - \hat{y}), \tag{7.10}$$

$$\frac{dR}{dt} = H_3(y - \hat{y}), \tag{7.11}$$

$$\hat{y} = \hat{\bar{V}}_o. \tag{7.12}$$

where H_1, H_2 and H_3 are the nonlinear observer gains which can be chosen to achieve fast convergence of the observer.

7.3 MPC Formulation

This section presents the formulation of the LMPC and NLMPC schemes for the FBC. The control objective is to regulate the output voltage without violating the peak current constraint. For a given inductor peak current i_{pk}, the CCM peak current (7.2) must satisfy

$$\frac{(n_1 V_1 - V_o)(V_o + n_1 V_1 \beta_1)T}{8 n_1 L_1 V_1} \leq i_{pk}. \tag{7.13}$$

If we define $x = [x_1, x_2]^T = [\bar{i}_{L1}, \bar{V}_o]^T$ and $u = \beta_1$, (7.13) can be rewritten in terms the state variables and control input as:

$$E_1(x, u) \leq 0. \tag{7.14}$$

where,

$$E_1(x, u) = \frac{(n_1 V_1 - x_2)(x_2 + n_1 V_1 u)}{8 n_1 L_1 V_1} - \frac{i_{pk}}{T}.$$

Then, the peak current protection requirement can be formulated as a mixed states and control input constraint for both LMPC and NLMPC schemes described in the following two subsections.

7.3.1 Offset-Free Linear MPC Formulation

The dynamic system represented by (7.6)-(7.8) can be easily linearized at the nominal operating point ($V_o = 80V$ and $P_o = 1KW$) with nominal value $x^o = [25, 80]^T$ and $u^o = 0.62$. Let $\tilde{x}_1 = \bar{i}_{L1} - 25$, $\tilde{x}_2 = \bar{V}_o - 80$ and $\tilde{u} = \beta_1 - 0.62$, the system can be transformed into its discrete-time version for a specific sampling time:

$$\tilde{x}(k+1) = f(\tilde{x}(k), \tilde{u}(k)) := A\tilde{x}(k) + B\tilde{u}(k), \tag{7.15}$$

$$\tilde{y}(k) = F\tilde{x}(k). \tag{7.16}$$

where $A \in \mathbb{R}^{n \times n}$, $B \in \mathbb{R}^{n \times m}$, $F \in \mathbb{R}^{m \times n}$. Note that $n = 2$ and $m = 1$ for the system under investigation.

The peak current constraint (7.14) can be rewritten as:

$$E_1(x(k),u(k)) = \frac{(n_1V_1 - (x_2^o + \tilde{x}_2(k)))(x_2^o + \tilde{x}_2(k))}{8nLV_1} + \frac{(n_1V_1 - (x_2^o + \tilde{x}_2(k)))n(u^o + \tilde{u}(k))}{8n_1L_1} - \frac{i_{pk}}{T}. \tag{7.17}$$

To eliminate the steady state error, the offset-free MPC has been developed in previous studies [82–85]. For this application, the plant model represented by (7.15)-(7.16) can be augmented with a constant disturbance model:

$$\tilde{x}(k+1) = A\tilde{x}(k) + B\tilde{u}(k) + B_d d(k), \tag{7.18}$$

$$d(k+1) = d(k), \tag{7.19}$$

$$\tilde{y}(k) = F\tilde{x}(k). \tag{7.20}$$

Based on the augmented model, the state and disturbance estimator can be designed as:

$$\begin{aligned} \hat{\tilde{x}}(k+1) = \quad & A\hat{\tilde{x}}(k) + B\tilde{u}(k) + B_d\hat{d}(k) \\ & + H_4(-F\tilde{x}(k) + F\hat{\tilde{x}}(k)), \end{aligned} \tag{7.21}$$

$$\hat{d}(k+1) = \quad \hat{d}(k) + H_5(-F\tilde{x}(k) + F\hat{\tilde{x}}(k)). \tag{7.22}$$

where H_4 and H_5 are observer gains which are designed to achieve fast convergence [83, 84].

The steady state values of the observer is

$$\begin{bmatrix} A-I & B \\ F & 0 \end{bmatrix} \begin{bmatrix} \hat{\tilde{x}}_s \\ \tilde{u}_s \end{bmatrix} = \begin{bmatrix} -B_d\hat{d}_s \\ 0 \end{bmatrix} \tag{7.23}$$

where $\tilde{u}_s$ is the steady state input while $\hat{\tilde{x}}_s$ and $\hat{d}_s$ are steady state of the observed state and disturbance, respectively.

Then the MPC online optimization problem can be formulated as follows: let $\Delta\tilde{x}(k) = \tilde{x}(k) - \hat{\tilde{x}}_s$ and $\Delta\tilde{u}(k) = \tilde{u}(k) - \tilde{u}_s$; at the time instant k, the state of the system, $\tilde{x}(k)$, is observed and the following optimal control problem $\mathscr{P}_N(\Delta\tilde{x}(k))$ is solved

$$\mathscr{P}_N(\Delta\tilde{x}(k)) : V_N^*(\Delta\tilde{x}(k)) = \min_{\Delta\tilde{\mathbf{x}},\Delta\tilde{\mathbf{u}}} \{V_N(\Delta\tilde{x}(k), \Delta\tilde{\mathbf{u}})\} \tag{7.24}$$

$$V_N(\Delta\tilde{x}(k), \Delta\tilde{\mathbf{u}}) = \sum_{j=k}^{k+N-1} G(\Delta\tilde{x}(j), \Delta\tilde{u}(j)) + \Phi(\Delta\tilde{x}(N))$$

subject to

$$\Delta\tilde{x}(j+1) = A\Delta\tilde{x}(k) + B\Delta\tilde{u}(k), \tag{7.25}$$

$$\Delta\tilde{x}(0) = \Delta\tilde{x}(k) \in \mathbb{R}^n; \tag{7.26}$$

$$E(\Delta\tilde{x}(\cdot), \Delta\tilde{u}(\cdot)) \leq 0,\ E : \mathbb{R}^{n+m} \to \mathbb{R}^l. \tag{7.27}$$

where,

$$\Delta\tilde{\mathbf{u}} = \{\Delta\tilde{u}(k), \Delta\tilde{u}(k+1), ..., \Delta\tilde{u}(k+N-1)\}, \tag{7.28}$$

is the control sequence,

$$\Delta\tilde{\mathbf{x}} = \{\Delta\tilde{x}(k), \Delta\tilde{x}(k+1), ..., \Delta\tilde{x}(k+N-1)\} \tag{7.29}$$

is the state trajectory,

$$\begin{aligned} G(\Delta\tilde{x}(j), \Delta\tilde{u}(j)) =& \Delta\tilde{x}(j)^T Q_1 \Delta\tilde{x}(j) + \Delta\tilde{u}(j)^T W_1 \Delta\tilde{u}(j), \\ & j = k, k+1, \cdots, k+N-1 \end{aligned} \tag{7.30}$$

and $\Phi(\Delta\tilde{x}(N))$ is the penalty for the final states. $Q_1 \in \mathbb{R}^{n\times n}$ and $W_1 \in \mathbb{R}^{m\times m}$ are the corresponding weighting matrices which are used to penalize the deviation of the output and the control input to their corresponding desired value, N is the prediction horizon, and $E(\Delta\tilde{x}(k), \Delta\tilde{u}(k))$ is the constraint matrix and can be written as follows with $l = 3$:

$$\begin{bmatrix} \Delta\tilde{u}(j) + \tilde{u}_s - (1 - u^o) \\ -\Delta\tilde{u}(j) - \tilde{u}_s - u^o \\ E_1(\Delta\tilde{x}(j) + \hat{\tilde{x}}_s, \Delta\tilde{u}(j) + \tilde{u}_s) \end{bmatrix}. \tag{7.31}$$

Note that the first two components are derived because of the boundedness of the phase shift ($\beta_1 \in [0, 1]$) and each component in (7.31) is bounded above by zero.

7.3.2 Nonlinear MPC Formulation

For the nonlinear dynamic system represented by (7.6)-(7.8), the nonlinear system can be transformed into its discrete-time version for a specific sampling time:

$$x(k+1) = f(x(k), u(k)), \tag{7.32}$$

$$y(k) = Fx(k). \tag{7.33}$$

The CCM peak current constraint (7.14) can be rewritten as:

$$E_1(x(k), u(k)) = \frac{(n_1V_1 - x_2(k))(x_2(k) + n_1V_1u(k))}{8n_1L_1V_1} - \frac{i_{pk}}{T}. \tag{7.34}$$

Then the MPC online optimization problem can be formulated as follows: at the time instant k, the state of the system, $x(k)$, is observed and the following optimal

control problem $\mathscr{P}_N(x(k))$ is solved

$$\mathscr{P}_N(x(k)) : V_N^*(x(k)) = \min_{\mathbf{x},\mathbf{u}}\{V_N(x(k),\mathbf{u})\} \tag{7.35}$$
$$V_N(x(k),\mathbf{u}) = \sum_{j=k}^{k+N-1} G(x(j),u(j)) + \Phi(x(N))$$

subject to

$$x(j+1) = f(x(j),u(j)),\ f : \mathbb{R}^{n+m} \to \mathbb{R}^n; \tag{7.36}$$

$$x(0) = x(k) \in \mathbb{R}^n; \tag{7.37}$$

$$E(x(\cdot),u(\cdot)) \leq 0,\ E : \mathbb{R}^{n+m} \to \mathbb{R}^l. \tag{7.38}$$

where,

$$\mathbf{u} = \{u(k), u(k+1), ..., u(k+N-1)\}, \tag{7.39}$$

is the control sequence,

$$\mathbf{x} = \{x(k), x(k+1), ..., x(k+N-1)\}, \tag{7.40}$$

is the state trajectory,

$$G(x(j),u(j)) = x(j)^T Q_2 x(j) + u(j)^T W_2 u(j), j = k, k+1, \cdots, k+N-1 \tag{7.41}$$

and $\Phi(x(N))$ is the penalty for the final states. $Q_2 \in \mathbb{R}^{n\times n}$ and $W_2 \in \mathbb{R}^{m\times m}$ are the corresponding weighting matrices which are used to penalize the deviation of the output and the control input from their corresponding desired value, N is the prediction horizon, and $E(x(k),u(k))$ is the constraint matrix and can be written as

follows with $l = 3$:

$$\begin{bmatrix} u(j) - 1 \\ -u(j) \\ E_1(x(j), u(j)) \end{bmatrix}. \tag{7.42}$$

Note that the first two components are derived because of the boundedness of the phase shift ($\beta_1 \in [0, 1]$) and each component in (7.42) is bounded above by zero.

Since the full bridge DC/DC converter has the millisecond level time constant, a rational choice of the sampling time is between $100\mu s$ and $400\mu s$ [101]. We choose $300\mu s$ as the sampling time for the controller. The length of the prediction horizon N is a basic tuning parameter for MPC controllers. However, we have to chose $N \geq 3$ to ensure that the prediction time length is no less than the time constant of the full bridge DC/DC converter. We will compare the closed-loop system performance with different prediction horizons for both the linear and nonlinear model based MPC algorithms. The weighting matrices Q_1, Q_2, W_1 and W_2 are the main tuning parameters of the quadratic cost functions (7.30) and (7.41) to shape the closed-loop response for desired performance. The closed loop performance criteria are defined as: (1) to achieve fast output response with small output overshoot; and (2) to avoid high frequency control input oscillations which might cause high slew rate for the inductor current and high stress for switching components. We evaluate the performance for different combinations of the weighting matrix using a virtual hardware for controller tuning. The virtual hardware is developed using MATLAB/Simulink/SimPowerSystems toolbox and has the same parameters as the real hardware. The preliminary evaluation results lead to the choice of $Q_1 = [0\ 0; 0\ 0.01]$, $Q_2 = [0\ 0; 0\ 0.2]$ and $W_1 = W_2 = 1$. Furthermore, we do not penalize the final states $x(N)$ and $\Delta\tilde{x}(N)$, meaning $\Phi(x(N)) = \Phi(\Delta\tilde{x}(N)) = 0$.

Given the fast dynamics of the converter, we have to apply fast algorithms to solve

the above optimization problem online in real-time. We employ a method, which we refer to as the InPA-SQP approach, to solve the nonlinearly constrained optimization problems for LMPC and NLMPC of the full bridge DC/DC converter.

7.4 InPA-SQP Algorithm

We now introduce a method, which we refer to as the Integrated Perturbation Analysis and Sequential Quadratic Programming (InPA-SQP) approach [90, 91], for the MPC implementation. It is worthwhile to point out that, for simplicity, we only interpret the InPA-SQP algorithm for the NLMPC case. For offset-free LMPC problem, one can simply replace $x(\cdot)$ and $u(\cdot)$ with their counterparts $\Delta\tilde{x}(\cdot)$ and $\Delta\tilde{u}(\cdot)$ and follow the same procedure to solve the nonlinearly constrained optimal control problem.

According to the MPC strategy, at the time instant k, the state of the system, $x(k)$, is observed and the optimal control problem $\mathscr{P}_N(x(k))$ defined by (7.35)−(7.38) is solved. The resulting optimal control sequence is

$$\mathbf{u}^*(x(k)) = \{u^*(k;x(k)), u^*(k+1;x(k)), ..., u^*(k+N-1;x(k))\}, \tag{7.43}$$

the optimal state trajectory is

$$\mathbf{x}^*(x(k)) = \{x^*(k;x(k)), x^*(k+1;x(k)), \cdots, x^*(k+N;x(k))\}, \tag{7.44}$$

where $x^*(k;x(k)) = x(k)$ and the model predictive control law at the time instant k is defined as:

$$h(x(k)) := u^*(k;x(k)). \tag{7.45}$$

According to InPA-SQP approach, the optimal solution at each time instant k for the observed state $x(k)$ is calculated using the optimal solution at the previous time instant, i.e., $k-1$. Given the optimal control sequence $\mathbf{u}^*(x(k-1))$, the updated optimal control sequence $\mathbf{u}^*(x(k))$ can be computed using perturbation analysis where the initial state is perturbed by $\delta x(k) = x(k) - x(k-1)$. If the variation $\delta x(k)$ in the initial state causes changes in the activity status of constraints, the variation is split into small variations, i.e., $\delta x^{(i)}(k),\ i = 1, 2, \cdots$, where for each incremental variation, only one constraint changes from active to inactive or vise versa. With these small variations, some intermediate points are identified along the line connecting $x(k-1)$ and $x(k)$. These intermediate points are denoted $x^{(0)}(k), x^{(1)}(k), \cdots, x^{(i_p)}(k)$ with $x^{(0)}(k) = x(k-1)$ and $x^{(i_p)}(k) = x(k)$, as shown in figure 7.6. Then the corresponding approximation of the optimal control sequence $\mathbf{u}^*(x^i(k)),\ i = 1, \cdots, i_p$, are calculated using perturbation analysis.

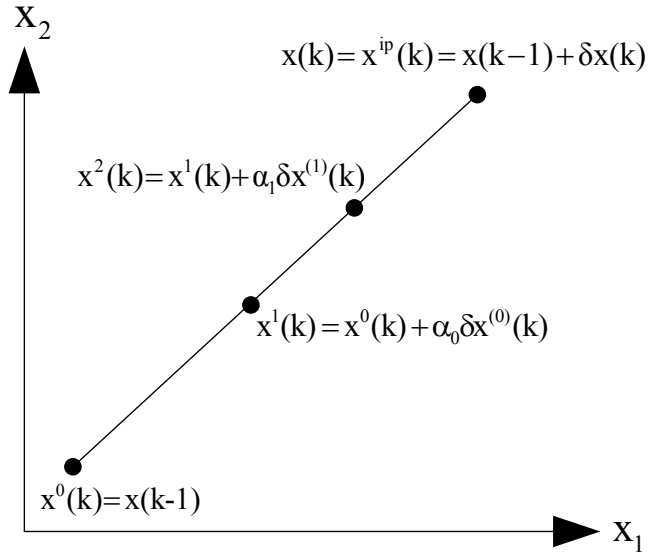

Figure 7.6: Intermediate initial conditions which handle the large perturbation.

Note that the control sequence provided by perturbation analysis at each intermediate point $x^i(k)$, i.e., $\mathbf{u}^*(x^i(k))$, is an approximation to the optimal control sequence.

Therefore, the error can accumulate and the optimality condition may be lost at these intermediate steps. To compensate for this error and maintain the optimality of the approximate solution, we use a special formulation of SQP with active set method to modify the perturbation analysis algorithm. This special formulation allows us to cast the solution of the SQP into a formula which is similar to that of the perturbation analysis, thereby facilitating the seamless integration of perturbation analysis and SQP to speed up the calculation of the optimal solution. The detailed algorithm is presented as follows for the general nonlinear MPC implementation:

At the time instant k, we need to solve $\mathscr{P}_N(x(k))$, given the solution of $P_N(x(k-1))$. We consider the general case where functions $G(x(\cdot), u(\cdot))$, $G : \mathbb{R}^{n+m} \rightarrow \mathbb{R}$, $\Phi(x(\cdot))$, $\Phi : \mathbb{R}^{n+m} \rightarrow \mathbb{R}$, $f(x(\cdot), u(\cdot))$, $E(x(\cdot), u(\cdot))$ are twice continuously differentiable with respect to x and u. Moreover, let us define the Hamiltonian function H at prediction time instants $k, k+1, \cdots, k+N-1$ as

$$\begin{aligned} H(j) :=& G(x(j), u(j)) + \lambda(j+1)^T f(x(j), u(j)) + \mu(j)^T E(x(j), u(j)), \\ & j = k, \cdots, k+N-1 \end{aligned} \tag{7.46}$$

where, $\mu(j)$ is the Lagrange multiplier associated with the inequality constraint (7.38) and $\lambda(j+1)$ is the Lagrange multiplier associated with equality constraint (7.36) at the prediction time instant j, where $j > k$.

Since we know the solution of $P_N(x(k-1))$ at the time instant k, by treating the initial state $x(k)$ as $x(k-1)$ plus its perturbation $\delta x(k) = x(k) - x(k-1)$, we go through the following steps to calculate the optimal solution for the initial state $x(k)$:

1. Measure $x(k)$ and assume $\mathbf{u}^*(x(k-1))$ and $x(k-1)$ are given from the previous time instant $k-1$.

2. Set $i = 0$, $\delta x^{(0)}(k) = x(k) - x(k-1)$, $x^{(0)}(j) = x^*(j; x(k-1))$, and $u^{(0)}(j) =$

$u^*(j; x(k-1))$, for $j = k, \cdots, k+N-1$.

3. Calculate the state and control variations $\delta x^{(i)}(j+1)$ and $\delta u^{(i)}(j)$, $j \in [k : k+N]$, for the initial state perturbation $\delta x^{(i)}(k)$, as follows:

$$\begin{aligned}
&\delta u^{(i)}(j) = -[I\ 0]K_0(j) \times \begin{bmatrix} Z_{ux}(j)\delta x^{(i)}(j) + f_u^T(j)T(j+1) + H_u(j) \\ E_x^a(j)\delta x^{(i)}(j) \end{bmatrix}, \\
&\delta x^{(i)}(j+1) = f_x(j)\delta x^{(i)}(j) + f_u(j)\delta u^{(i)}(j), \\
&\text{and } \delta x^{(i)}(k) \text{ given,}
\end{aligned} \tag{7.47}$$

where $H_u(j)$ is the partial derivative of the Hamiltonian function with respect to control u at the prediction time instant j, and

$$\begin{aligned}
Z_{uu}(j) &= H_{uu}(j) + f_u^T(j)S(j+1)f_u(j), \\
Z_{ux}(j) &= Z_{xu}(j)^T = H_{ux}(j) + f_u^T(j)S(j+1)f_x(j), \\
Z_{xx}(j) &= H_{xx}(j) + f_x^T(j)S(j+1)f_x(j),
\end{aligned} \tag{7.48}$$

with $S(j)$ being calculated by the following backward recursive equations

$$\begin{aligned}
&S(k+N) = \Phi_{xx}(k+N), T(k+N) = 0, \\
&S(j) = Z_{xx}(j) - [Z_{xu}(j)\ E_x^{aT}(j)]K_0(j)\begin{bmatrix} Z_{ux}(j) \\ E_x^a(j) \end{bmatrix}, \\
&T(j) = f_x^T(j)T(j+1) - [Z_{xu}(j)\ E_x^{aT}(j)]K_0(j)\begin{bmatrix} f_u^T(j)T(j+1) + H_u(j) \\ 0 \end{bmatrix},
\end{aligned} \tag{7.49}$$

and when the constraint is active, $K_0(\cdot)$ is given by

$$K_0(j) = \begin{bmatrix} Z_{uu}(j) & E_u^{aT}(j) \\ E_u^a(j) & 0 \end{bmatrix}^{-1}, \tag{7.50}$$

where $E^a(j)$ is a vector consisting of those elements of the vector $E(x(j), u(j))$ whose corresponding inequality constraints are active. If no constraint is active at the prediction time instant j,

$$K_0(j) = [Z_{uu}(j)]^{-1}, \ j = k, \cdots, k+N-1. \tag{7.51}$$

Moreover, when the constraint is active, calculate the optimal Lagrange multiplier variation $[\delta\mu^{(i)}(k), \delta\mu^{(i)}(k+1), \cdots, \delta\mu^{(i)}(k+N-1)]$ corresponding to initial state variation $\delta x^{(i)}(k)$ as follows:

$$\delta\mu^{(i)}(j) = -[0 \ I]K_0(j) \times \begin{bmatrix} Z_{ux}(j)\delta x^{(i)}(j) + f_u^T(j)T(j+1) + H_u(j) \\ E_x^a(j)\delta x^{(i)}(j) \end{bmatrix}. \tag{7.52}$$

All matrices are evaluated at $x^{(i)}(\cdot)$ and $u^{(i)}(\cdot)$.

4. Find the smallest α_i among α_{ik} such that the perturbation $\alpha_i \delta x^{(i)}(k)$ changes the status of the constraint at least at one instant, namely:

$$\alpha_i = \min_k \{\alpha_{ik}, k = 0, \cdots, N-1, \text{and } 0 \le \alpha_{ik} \le 1\}.$$

If for all $k \in [0 : N-1]$, either $\alpha_{ik} < 0$ or $\alpha_{ik} > 1$, set $\alpha_i = 1$.

5. If $\alpha_i = 1$, set

$$\begin{aligned} u^{i+1}(\cdot) &= u^i(\cdot) + \delta u^{(i)}(\cdot) \\ x^{i+1}(\cdot) &= x^i(\cdot) + \delta x^{(i)}(\cdot) \end{aligned} \tag{7.53}$$

and set the solution $\mathbf{u}^*(x(k)) = u^{(i+1)}(\cdot)$. Otherwise:

- If $\alpha_i = 0$, change the activity status of the corresponding constraint accordingly. That is, if α_i corresponds an active (inactive) constraint, set the constraint inactive (active). Go to step 2.
- If $\alpha_i < 1$ set

$$\begin{aligned} u^{i+1}(\cdot) &= u^i(\cdot) + \alpha_i \delta u^{(i)}(\cdot) \\ x^{i+1}(\cdot) &= x^i(\cdot) + \alpha_i \delta x^{(i)}(\cdot) \end{aligned} \tag{7.54}$$

and

$$\begin{aligned} &\delta x^{(i+1)}(k) = (1 - \alpha_i)\delta x^{(i)}(k), \\ &x^{i+1}(k) = x^i(k) + \alpha_i \delta x^{(i)}(k), \\ &i = i + 1. \end{aligned}$$

Go to step 3.

Fig.7.7 shows the flowchart of the InPA-SQP algorithm. The perturbed optimal control solution corresponding to the large perturbation $\delta x(k)$ can be approximated by augmenting the nominal solution with the intermediate ones as:

$$u^*(j; x(k)) + \sum_i \delta u^{(i)}(j), \ j = k, \cdots, k + N - 1.$$

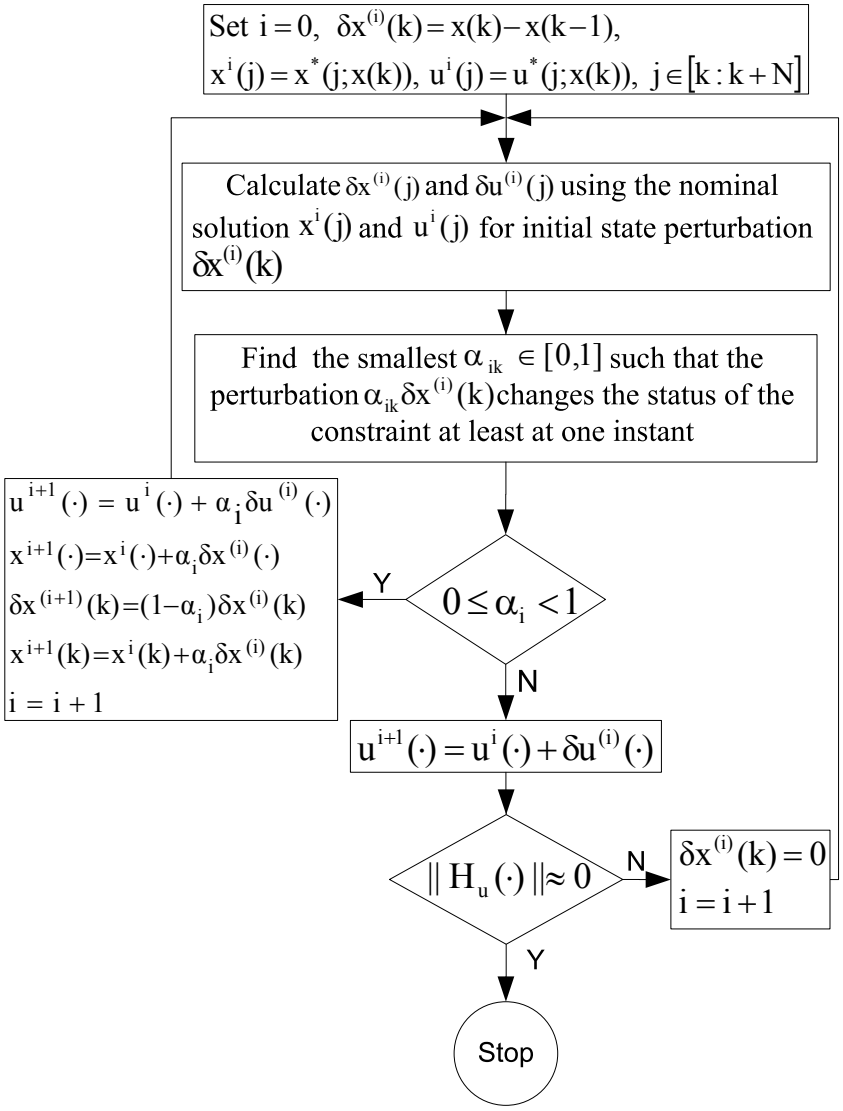

Figure 7.7: Flowchart of the InPA-SQP algorithm.

If at the point $x(k) + \delta x(k)$, $\sum_{j=k}^{k+N-1} \|H_u(j)\|$ is not small enough, the prescribed procedure goes on with zero initial state perturbation $\delta x^{(i)}(k) = 0$ until the optimal solution with $\sum_{j=k}^{N+k-1} \|H_u(j)\| \simeq 0$ is achieved.

The InPA-SQP synergistically combines the solutions derived using perturbation analysis and SQP to solve the optimization problem with mixed input and state constraints. It is shown in [90] that it can significantly improve the computational efficiency while effectively handling the nonlinear constraints, making the MPC feasible for power electronics systems with fast dynamics. With the introduction of the InPA-SQP solver, we now proceed to implement the MPC on our hardware.

7.5 Experimental Validation

The goal of this section is to present the experimental results to compare the LMPC and NLMPC schemes using the InPA-SQP as the optimization solver. Both the LMPC and NLMPC schemes are implemented on a full bridge DC/DC converter which is the DC/DC1 as described in [99].

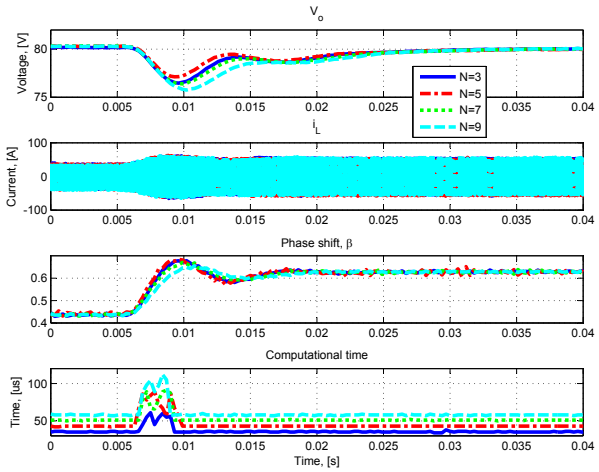

Figure 7.8: Performance comparison of LMPC with different prediction horizon for a step-down change of R from 12.8Ω to 6.4Ω.

Table 7.1: Performance summarization of the LMPC

	N=3	N=5	N=7	N=9
Settling time	20ms	20ms	20ms	20ms
Voltage drop	3.4V	2.9V	3.4V	4.2V
Computational time	$61\mu s$	$89\mu s$	$91\mu s$	$112\mu s$

First, we compare the closed-loop performance for LMPC with different prediction horizon N in the presence of a large step change in the load resistance R in Fig.7.8. Initial R is 12.8Ω (500W output power). A step-down change of the load resistance R is then applied to deliver 1000W output power, which is the rated output power of the converter. The settling times of the LMPC for different prediction horizons N are similar. However, when $N = 5$, the transient voltage drop is the smallest. At both load conditions, the output voltage is regulated to the desired value for all selected prediction horizons. For different prediction horizons, the computation time increases as the prediction horizon increases. The closed loop performance and computational time of the LMPC is summarized in Table.7.1.

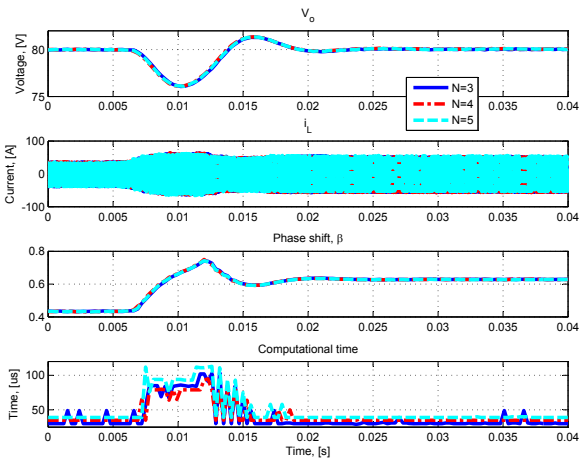

Figure 7.9: Performance comparison of NLMPC with different prediction horizon for a step-down change of R from 12.8Ω to 6.4Ω.

Fig.7.9 compares the waveforms for a step-down change of R when the NLMPC algorithm with $N = 3, 4$ and 5 is applied to control the full bridge DC/DC converter.

Table 7.2: Performance summarization of the NLMPC

	N=3	N=4	N=5
Settling time	13ms	13ms	13ms
Voltage drop	3.9V	3.9V	3.9V
Computational time	$102\mu s$	$105\mu s$	$113\mu s$

A step-down change of the load resistance R from 12.8Ω to 6.4Ω is then applied to deliver $1000W$ rated output power. At both load conditions, the output voltage is regulated to the desired value for all selected prediction horizon. The performance of NLMPC for $N = 3, 4$ and 5 are essentially the same while the computation time increases as the prediction horizon increases. Therefore, it is desirable to choose $N = 3$ to reduce computation time. The closed loop performance and computational time of the NLMPC is summarized in Table.7.2.

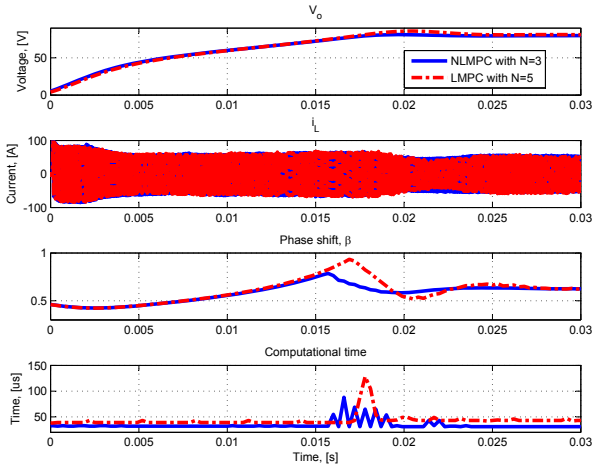

Figure 7.10: Comparison of the LMPC and NLMPC schemes during the starting process.

Fig.7.10 shows the experimental waveforms of LMPC and NLMPC of the full bridge DC/DC converter during the starting process with rated $1KW$ load. For both the LMPC and NLMPC schemes, the peak currents are limited within the maximum tolerable value $75A$ although the peak current is slightly higher than $75A$ during the first $300\mu s$. The maximum output voltage is 86V for the LMPC scheme while, for the

NLMPC scheme, it is 81.2V. The maximum computation time for the LMPC scheme is 128μs which is 40μs longer than the NLMPC scheme's 88μs.

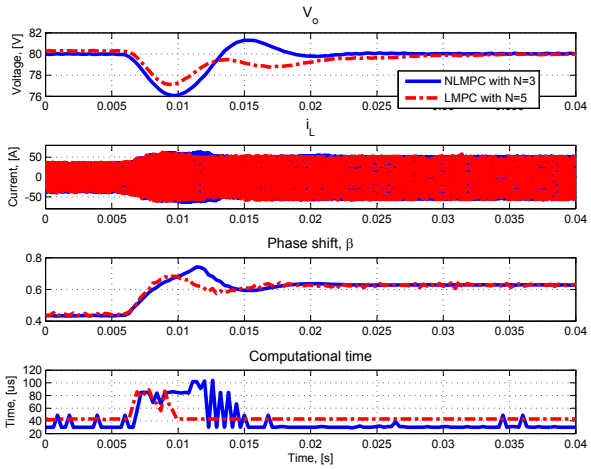

Figure 7.11: Comparison of the LMPC and NLMPC schemes for a step-down change of R from 12.8Ω to 6.4Ω.

Fig.7.11 shows the waveforms of LMPC and NLMPC of the full bridge DC/DC converter under a step-down change of R. The LMPC scheme has $N = 5$ while the NLMPC scheme has $N = 3$. We define the voltage regulation error as $e_v = \int_0^{0.04} |V_o - 80|\, dt$. For the LMPC scheme, $e_v = 0.025$ while, for the NLMPC scheme, $e_v = 0.023$. Moreover, from Fig.7.11, the settling time of the NLMPC scheme is shorter than that of the LMPC scheme. However, the maximum voltage drop of the LMPC scheme is 2.8V which is 1.1V lower than that of the NLMPC scheme. The maximum computation time for the LMPC scheme is 89μs while that of the NLMPC scheme is 104μs.

Finally, Fig.7.12 shows the experimental waveforms for LMPC and NLMPC of the full bridge DC/DC converter under the overload operation condition. The power converter is initially operating with 1KW load ($R = 6.4\Omega$). The load resistance R is then reduced to 2Ω. For both the LMPC and NLMPC schemes, the responses are similar. At the steady state after the transient, the peak current is limited within

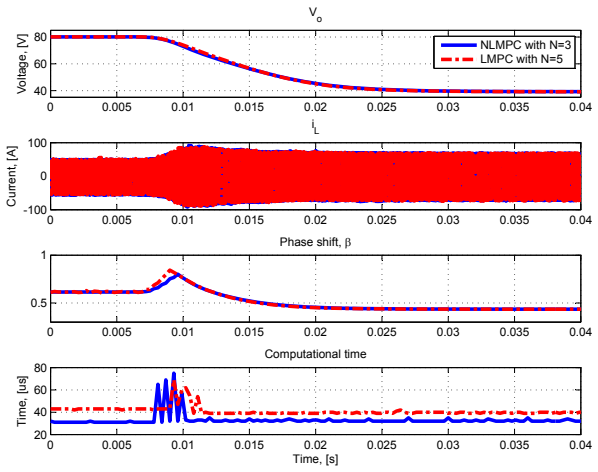

Figure 7.12: Comparison of the LMPC and NLMPC schemes under overload operation condition.

the maximum tolerable value $75A$ except that the peak current is slightly higher than $75A$ during the transient. This is partially due to the fact that we do not use a current sensor in the control schemes. The output voltage drops from $80V$ to $40V$ during the transient since i_{L1} is constrained. The maximum computation time for the LMPC scheme is $69\mu s$ which is $6\mu s$ shorter than that of the NLMPC scheme.

7.6 Summary

In this chapter, the LMPC and NLMPC schemes are proposed to control a FBC of the DHPS. The control objective is to regulate the output voltage without violating the peak current constraint. A linear or a nonlinear dynamic model is used for future behavior prediction while the peak current protection requirement was formulated as a mixed input and state constraint for both the MPC schemes. The computation time and closed loop system performances for the LMPC and NLMPC of the FBC under three operating conditions are compared. The InPA-SQP method is employed to solve the nonlinearly constrained optimal control problems with a

sub-millisecond level sampling time. The experimental results reveal that both the LMPC and NLMPC schemes successfully achieved voltage regulation and peak current protection. In comparison with the LMPC scheme, the NLMPC scheme achieves better performance during the starting process and load step-change process and has the similar performance under the overload operation condition. In terms of computation time, the LMPC scheme has slightly shorter one during the load step-change process and overload operation condition. However, the NLMPC scheme has a much shorter computation time than the LMPC scheme during the starting process. In addition, the implementation of the LMPC scheme requires an offset-free algorithm to eliminate the steady state error, complicating the control design. Therefore, considering the algorithm complexity, the closed loop performance and the necessary computation time, the NLMPC scheme is more desirable than the LMPC scheme for this application.

Chapter 8

Conclusions and Future Work

This dissertation has focused on the modeling, analysis, and control of a DC hybrid power system with multiple power converters, aiming at all electric ship as the application platform. At the system level, tools are developed to facilitate the research described in this dissertation, including the DHPS testbed (Chapter 2) and the IPS model of an AES (covered in Chapter 3). At the device level, in-depth analysis and design are performed for DC/DC converters which will serve as the critical enablers for the DHPS power management system. New modulation strategy is also developed to overcome the low efficiency of conventional PSM. Advanced control methodology, namely the model predictive control, is implemented for the full bridge DC/DC converter to handle physical constraints and achieve voltage regulation objective (Chapter 7).

8.1 Conclusions

The main work and results of this dissertation are summarized as follows:

- *Developed a testbed for DC hybrid power system*

  In Chapter 2, a DC hybrid power system testbed is introduced. The testbed

includes a realtime simulation and control rapid prototyping platform, three isolated DC/DC converters, two programmable power sources, two programmable electronics loads, and a supercapacitor based energy storage bank. This testbed has: (1) fully digital simulation capability as a preliminary analysis tool to support the modeling and control development effort, (2) adequate hardware resources for controlling complex dynamic system, (3) necessary hardware, including power sources, power converters and loads, to verify analysis, modeling and evaluation results, and (4) control rapid prototyping capability to ensure quick implementation of advanced control algorithms for system performance evaluation and design validation. Therefore, this testbed can facilitate optimization and power management strategy development for the DHPS.

- *Developed a modularized simulation model for the IPS of an AES*

  The IPS model has power generation modules including a gas turbine and fuel cell, an electric propulsion module and a zonal electric distribution system which, by itself, has many power conversion modules. The simulation results verify that the IPS model can be used to perform simulations for scenarios such as failure emulation, power flow path reconfiguration and energy management. This model provides an effective tool for AES system research.

- *Designed a new power flow model for the dual active bridge DC/DC converter*

  In addition to those major parameters used by conventional power flow analysis, this new model also considers minor parameters, namely the power semiconductor voltage loss and dead time. The minor parameters are critical for explaining the observed internal power transfer and phase drift phenomena, which are relevant to power flow characterization of the DAB converter. While the new model provides a more accurate prediction over a wide range of operating conditions,

it also identifies new characteristics such as reverse power transfer and energy sink that are observed in experiments. Therefore, the new model can serve as a research tool for optimal hardware design, operating range selection and power management strategy development.

- *Proposed a novel current mode PWM strategy for the dual active bridge DC/DC converter*

  The proposed modulation strategy can avoid the drawbacks of the conventional phase shift modulation and achieve: (1) zero circulating current to reduce conduction loss; (2) soft-switching over the full operating range to reduce switching loss; (3) zero idling power to eliminate idle loss; (4) simple but accurate power flow characterization; and (5) controllable output power between zero and the maximum for different combinations of terminal voltages. Moreover, the proposed modulation strategy enables the converter to achieve the same power density under the same current stress as that of a phase shift modulated converter. Therefore, in comparison with the traditional ones, the proposed strategy is more suitable for energy storage system application.

- *Developed and implemented LMPC and NLMPC for a full bridge DC/DC converter*

  Both the LMPC and NLMPC schemes are employed to control the full bridge DC/DC converter. The controllers can successfully regulate the output voltage without violating the peak current constraint. Moreover, comparative evaluation of the LMPC and NLMPC schemes is performed. The computation time and closed loop system performances under starting, overload and load step change conditions are compared. The experimental results reveal that both the LMPC and NLMPC schemes can successfully achieve voltage regulation and

peak current protection. Considering the algorithm complexity, the closed loop performance and the necessary computation time, the NLMPC scheme is more desirable than the LMPC for this application. This is the first implicit MPC application for power electronics system with very fast dynamics.

8.2 Future Work

Although substantial progress has been made on the modeling, analysis, optimization, and control of the DC hybrid power system, the results of this dissertation point to several interesting directions for future work.

- *Investigating control methodologies for power converters with multiple operating modes*

  Our testbed has two full bridge DC/DC converters. The full bridge DC/DC converter can operate with either a discontinuous conduction mode or a continuous conduction mode. In this dissertation, we developed a dynamic model and designed the MPC schemes for the full bridge DC/DC converter based on the assumption that it operates with a discontinuous conduction mode. Although we designed the converter to operate with a discontinuous conduction mode to eliminate the negative current, the converter could operate with a continuous conduction mode under certain conditions. Therefore, we could use the hybrid control scheme for the power converters to ensure the closed loop performance if the power converter operates with multiple modes.

- *Exploring advanced control methodologies for the DC hybrid power system*

  In this dissertation, we employed LMPC and NLMPC schemes to control the full bridge DC/DC converter in Chapter 7. The DC hybrid power system investigated in this dissertation has multiple power converters. It is a challenging

control problem to coordinate the power converters to achieve fast power tracking without violating the physical limitations of the power converters. Therefore, development of an efficient strategy for the coordination of decentralized MPC schemes could be an opportunity and a challenge in enhancing the system level control performance.

Appendix

Appendix A

Gas Turbine Model

The turbine model is based on [102]. For a self contained presentation, we include the key equations in this appendix.

The compressor mass flow is given by

$$W_c = \frac{\sqrt{T_{amb}}}{p_{amb}}\phi_c$$

The mass flow parameter ϕ_c is a function of the corrected speed parameter $\hat{\omega}_{tc}$ ($= \frac{\omega_{tc}}{\sqrt{T_{c,in}}}$) and pressure ratio across the compressor $\Gamma_{PR,c}$. This is determined using zero slope line method ([103]) and is given by

$$\frac{\phi_c}{\phi_{ZS,c}} = \begin{cases} 1 + k_{c2}\left(1 - e^{k_{c1}\left(\frac{\Gamma_{PR,c}}{\Gamma^{ZS}_{PR,c}} - 1\right)}\right), \ (\Gamma_{PR,c} < \Gamma^{ZS}_{PR,c}) \\ 1 - k_{c2}k_{c1}\left(\frac{\Gamma_{PR,c}}{\Gamma^{ZS}_{PR,c}} - 1\right), \ (\Gamma_{PR,c} \geq \Gamma^{ZS}_{PR,c}) \end{cases}$$

where $\phi_{ZS,c}$, $\Gamma_{ZS,c}$ are zero slope mass flow parameter and pressure ratio respectively. These along with the constants k_{c1} and k_{c2} are polynomial functions of $\hat{\omega}_{tc}$, whose coefficients are determined by regression on the compressor maps.

The compressor isentropic efficiency is given by

$$\eta_{is,c} = k_{c3}\phi_c^2 + k_{c4}\phi_c + k_{c5}$$

where k_{c3}, k_{c4}, k_{c5} are quadratic functions of the speed parameter $\widehat{\omega}_{tc}$ whose coefficients are determined by regression on the compressor efficiency maps.

The turbine mass flow (W_t) is given by

$$W_t = \frac{\sqrt{T_b}}{p_b}\phi_t$$

$\Gamma_{PR,t}$ is the pressure ratio across the turbine. The function ϕ_t depends on the turbine expansion ratio $\Gamma_{PR,t}$, corrected speed parameter $\hat{\omega}_{tc}$ and is given by

$$\phi_t = \begin{cases} A_t\sqrt{\frac{2\gamma}{\gamma-1}\left(\Gamma_{PR,t}^{\frac{2}{\gamma}} - \Gamma_{PR,t}^{\frac{\gamma+1}{\gamma}}\right)}, & (\Gamma_{PR,t} > p_{crit}) \\ A_t\sqrt{\frac{2\gamma}{\gamma-1}\left(p_{crit}^{\frac{2}{\gamma}} - p_{crit}^{\frac{\gamma+1}{\gamma}}\right)}, & (\Gamma_{PR,t} \leq p_{crit}) \end{cases}$$

where A_t is the effective flow area and is given by

$$A_t = \frac{k_{t1}}{\Gamma_{PR,t}^2} + \frac{k_{t2}}{\Gamma_{PR,t}} + k_{t3}.$$

The coefficients k_{t1}, k_{t2} and k_{t3} are polynomial functions of the corrected speed parameter $\hat{\omega}_{tc}$ and is determined using regression on the turbine maps.

The turbine isentropic efficiency is given by

$$\eta_{is,t} = k_{t4}\Gamma_{PR,t}^2 + k_{t5}\Gamma_{PR,t} + k_{t6}$$

where k_{t4}, k_{t5}, k_{t6} are cubic functions of the speed parameter $\widehat{\omega}_{tc}$ whose coefficients

are determined by regression on the turbine efficiency maps.

Bibliography

Bibliography

[1] N. Doerry and J. C. Davis, "Integrated power system for marine applications," *Naval Engineers Journal*, 1994.

[2] N. Doerry, H. Robey, J. Amy and C. Petry, "Power the future with the integrated power system," *Naval Engineers Journal*, 1996.

[3] C. Petry and J. Rumburg, "Zonal electrical distribution systems: an affordable architecture for the future," *Naval Engineers Journal*, 1993.

[4] J. G. Ciezki and R. W. Ashton, "Selection and stability issues associated with a navy shipboard DC zonal electric distribution system," *IEEE Transactions on Power Delivery*, 2000.

[5] T. Ericsen and A. Tucker, "Power electronics building blocks and potential power modulator applications," *IEEE Conference Record of the Twenty-Third International Power Modulator Symposium*, New York, 1998.

[6] Z. Ye, K. Xing, S. Mazumder, D. Borojevic and F.C. Lee, "Modeling and control of parallel three-phase PWM boost rectifiers in PEBB-based DC distributed power systems," *IEEE Applied Power Electronics Conference*, 1998.

[7] C. Dufour and J. Belanger, "A PC-based real-time parallel simulator of electric systems and drives," *International Conference on Parallel Computing in Electrical Engineering*, 2004.

[8] P. Moraal and I. Kolmanovsky, "Turbocharger modeling for automotive control applications," *Journal of Engg. For Gas Turbines and Power*, 2003.

[9] V. Tsourapas, J. Sun and A. Nickens, "Control oriented modeling and analysis of a hybrid solid oxide fuel cell and gas turbine (SOFC/GT) system," *Proceedings of the 2006 Fuel Cell Seminar,* 2006.

[10] E. A. Lewis, "Cyclo convertor drive systems," *Sixth International Conference on Power Electronics and Variable Speed Drives*, 1996.

[11] D. Fu, F. C. Lee, "Phase compensation driving scheme for SR," *Patent Application No:11/749,405*

[12] D. Fu, F. C. Lee, Y. Liu, and M. Xu, "Multi-element resonant converters," *Patent Application No.:12/134,413*

[13] D. Fu, F. C. Lee, Y. Qiu, F. Wang, "A novel high-power-density three-level LCC resonant converter with constant-power-factor-control for charging applications," *IEEE Transaction on Power Electronics*, 2008.

[14] P. Tenti, L. Malesani and L. Rossetto, "Optimum control of N-input K-output matrix converters," *IEEE Transactions on Power Electronics*, 1992.

[15] S. S. Kalsi, B. B. Gamble, G. Snitchler and S. O. Ige, "The status of HTS ship propulsion motor developments," *IEEE Power Engineering Society General Meeting*, 2006

[16] T. I. Fossen, *Marine Control Systems: Guidance, Navigation and Control of Ships, Rigs and Underwater Vehicles,* Marine Cybernetics AS, 2002.

[17] D. Fu, Y. Liu, F. C. Lee, M. Xu, "A novel driving scheme for synchronous rectifiers (SR) for LLC resonant converters," *IEEE Transaction on Power Electronics,* 2009.

[18] D. Huang, D. Fu, F. C. Lee, "High switching frequency, high efficiency CLL resonant converter with synchronous rectifier," in *Proc. IEEE ECCE, 2009.*

[19] D. Fu, F. C. Lee, Y. Liu, M. Xu, "Novel multi-element resonant converters for front-end DC/DC converters," in *Proc. IEEE PESC 2008.*

[20] R. C. Bansal, "Automatic reactive power control of isolated wind-diesel hybrid power systems," *IEEE Trans. Industrial Electronics,* vol. 53, pp.1116-1126, Jun. 2006.

[21] T. Senjyu, T. Nakaji, K. Uezato and T. Funabashi,"A hybrid power system using alternative energy facilities in isolated island," *IEEE Trans. Energy Conversion,* vol. 20, pp.406-414, Jun. 2005.

[22] V. Tsourapas, A. Stefanopoulou, and J. Sun, "Model-based control of an integrated fuel cell and fuel processor with exhaust heat recirculation," *IEEE Trans. on Control Systems Technology,* vol. 15, pp.233-245, Mar. 2007.

[23] A. T-Raissi and D. L. Block, "Hydrogen: automotive fuel of the future," *IEEE Power and Energy Magazine,* vol. 2, pp.40-45, Nov./Dec. 2004.

[24] D. Fu, B. Lu, F. C. Lee, "1MHz high efficiency LLC resonant converters with synchronous rectifier," in *Proc. IEEE PESC, 2007.*

[25] D. Fu, Y. Qiu, Y. Sun, F. C. Lee, "A 700kHz high-efficiency high-power-density three-level parallel resonant DC-DC converter for high-voltage charging applications," in *Proc. IEEE APEC, 2007.*

[26] Y. Qiu, B. Lu, B. Yang, D. Fu, F. C. Lee, "A high-frequency high-efficiency three-level LCC converter for high-voltage charging applications," in *Proc. IEEE PESC, 2004.*

[27] W. Gao,"Performance comparison of a fuel cell-battery hybrid powertrain and a fuel cell-ultracapacitor hybrid powertrain," *IEEE Trans. Vehicular Technology,* vol. 54, pp.846-855, May 2005.

[28] A. Emadi, S. S. Williamson and A. Khaligh,"Power electronics intensive solutions for advanced electric, hybrid electric, and fuel cell vehicular power systems," *IEEE Trans. Power Electronics,* vol. 21, pp.567-577, May 2006.

[29] X. Zhang, C. Mi, A. Masrur, and D. Daniszewski, "Wavelet based power management of hybrid electric vehicles with multiple onboard power sources," *Journal of Power Sources,* vol. 185, pp. 1533-1543, Dec. 2008.

[30] H. Sheng, W. Shen, H. Wang, D. Fu, Y. Pei, "Design and implementation of high power density three-level parallel resonant converter for capacitor charger," in *Proc. IEEE APEC, 2007.*

[31] D. Fu, Y. Qiu, B. Lu, F. Wang, F. C. Lee, "An improved three-level LCC converter with a novel control strategy for high-frequency high-power-density capacitor-charging power supplies," in *Proc. IEEE APEC, 2006.*

[32] H. Bai, and C. Mi, "Eliminate reactive power and increase system efficiency of isolated bidirectional dual-active-bridge dc-dc converters using novel dual-phase-shift control," *IEEE Trans. Power Electronics,* vol.23, pp.2905-2914, Nov. 2008.

[33] J. Sun, D. M. Mitchell, M. F. Greuel, P. T. Krein, and R. M. Bass, "Averaged modeling of PWM converters operating in discontinuousconduction mode," *IEEE Trans. Power Electronics,* vol. 16, pp.482-492, Jul. 2001.

[34] R. Morrison, and M. G. Egan, "A new power-factor-corrected single-transformer UPS design," *IEEE Trans. Industry Applications,* vol.36, pp.171-179, Jan./Feb. 2000.

[35] F. Krismer, J. Biela, and J. W. Kolar, "A comparative evaluation of isolated bidirectional dc/dc converters with wide input and output voltage range," in *Proc. Industrial Applications Society Annual Meeting,* 2005, pp.599-606.

[36] F. Krismer, J. Biela, and J. W. Kolar, "Performance optimization of a high current dual active bridge with a wide operating voltage range," in *Proc. IEEE Power Electronics Specialists Conf. (PESC),* 2006, pp.1-7.

[37] J. L. Duarte, M. Hendrix, and M. G. Simoes, "Three-port bidirectional converter for hybrid fuel cell systems," *IEEE Trans. Power Electronics,* vol.22, pp.480-487, Mar. 2007.

[38] H. M. Tao, A. Kotsopoulos, J.L. Duarte, and M.A.M. Hendrix, "Transformer-coupled multiport ZVS bidirectional dc-dc converter with wide input range," *IEEE Trans. Power Electronics,* vol.23, pp.771-781, Mar. 2008.

[39] J. Walter, and R. W. De Doncker, "High-power galvanically isolated dc/dc converter topology for future automobiles", in *Proc. IEEE Power Electronics Specialists Conf. (PESC),* 2003, pp.27-32.

[40] D. Fu, P. Kong, S. Wang, F. C. Lee, M. Xu, "Analysis and suppression of conducted EMI eEmissions for front-end LLC resonant DC/DC converters," in *Proc. IEEE PESC, 2008.*

[41] D. Fu, Y. Liu, F. C. Lee, M. Xu, "An improved novel driving scheme of synchronous rectifiers for LLC resonant converters," in *Proc. IEEE APEC, 2008.*

[42] F. C. Lee, S. Wang, P. Kong, C. Wang, D. Fu, "Power architecture design with improved system efficiency, EMI and power density," in *Proc. IEEE PESC, 2008.*

[43] H. Sangtaek, and D. Divan,"Bi-directional dc/dc converters for plug-in hybrid electric vehicle (PHEV) applications," in *Proc. IEEE Appl. Power Electron. Conf. Expo (APEC),* 2008, pp.1-5.

[44] C. Zhao, S. D. Round, and J. W. Kolar, "An isolated three-port bidirectional dc-dc converter with decoupled power flow management," *IEEE Trans. Power Electron.,* vol.23, pp.2443-2453, Sept. 2008.

[45] H. Bai, C. Mi, and S. Gargies, "The short-time-scale transient processes in high-voltage and high-power isolated bidirectional dc-dc converters," *IEEE Trans. Power Electron.,* vol.23, pp.2648-2656, Nov. 2008.

[46] S. Inoue, and H. Akagi, "A bidirectional dc-dc converter for an energy storage system with galvanic isolation," *IEEE Trans. Power Electron.,* vol.22, pp.2299-2306, Nov. 2007.

[47] S. Inoue, and H. Akagi, "A bidirectional isolated dc-dc converter as a core circuit of the next-generation medium-voltage power conversion system," *IEEE Trans. Power Electronics,* vol.22, pp.535-542, Mar. 2007.

[48] N. M. L. Tan, S. Inoue, A. Kobayashi, and H. Akagi, "Voltage balancing of a 320-V, 12-F electric double-layer capacitor bank combined with a 10-kW bidirectional isolated dc-dc converter," *IEEE Trans. Power Electronics,* vol.23, pp.2755-2765, Nov. 2008.

[49] F. Z. Peng, H. Li, G.-J. Su, and J. S. Lawler, "A new ZVS bi-directional dc-dc converter for fuel cell and battery application," *IEEE Trans. Power Electronics,* vol. 19, pp.54-65, Jan. 2004.

[50] H. Xiao, and S. Xie, "A ZVS bidirectional dc-dc converter with phase-shift plus PWM control scheme," *IEEE Trans. Power Electronics,* vol. 23, pp. 813-823, Mar. 2008.

[51] J. Zhang, F. Zhang, X. Xie, D. Jiao, and Z. Qian, "A novel ZVS DC/DC converter for high power applications," *IEEE Trans. Power Electronics,* vol. 19, pp. 420-429, Mar. 2004.

[52] H. Zhou, and A. M. Khambadkone, "Hybrid modulation for dual active bridge bi-directional converter with extended power range for ultracapacitor application", in *Proc. Industry Applications Society Annual Meeting (IAS),* 2008, pp.1-8.

[53] A. K. Jain, and R. Ayyanar, "PWM control of dual active bridge: comprehensive analysis and experimental verification", in *Proc. Annual Conference of the IEEE Industry Electronics Society (IECON),* 2008, pp.909-915.

[54] R. W. De Doneker, D. M. Divan, and M. H. Kheraluwala, "A three-phase soft-switched high-power-density dc/dc converter for high-power applications," *IEEE Trans. Industry Applications,* vol. 27, pp.797-806, Jan./Feb. 1991.

[55] M. H. Kheraluwala, R. W. Gascoigne, D.M. Divan, and E. D. Baumann, "Performance characterization of a high-power dual active bridge dc-to-dc converter," *IEEE Trans. Industry Applications,* vol. 28, pp.1294-1301, Nov./Dec. 1992.

[56] F. Z. Peng, H. Li, G.-J. Su, and J. S. Lawler, "A new ZVS bi-directional dc-dc converter for fuel cell and battery application," *IEEE Trans. Power Electronics,* vol. 19, pp.54-65, Jan. 2004.

[57] D. H. Xu, C. H. Zhao, and H. F. Fan," A PWM plus phase-shift control bidirectional dc-dc converter," *IEEE Trans. Power Electronics,* vol. 19, pp.666-675, May 2004.

[58] L. Zhu, "A novel soft-commutating isolated boost full-bridge ZVS-PWM dc-dc converter for bi-directional high power applications," *IEEE Trans. Power Electronics,* vol. 21, pp.422-429, Mar. 2006.

[59] H.-J. Chiu, and L.-W. Lin, "A bidirectional dc-dc converter for fuel cell electric vehicle driving system," *IEEE Trans. Power Electronics,* vol. 21, pp. 950-958, Jul. 2006.

[60] J. Zhang, J.-S. Lai, R.-Y. Kim, and W. Yu, "High-power density design of a soft-switching high-power bidirectional dc-dc converter," *IEEE Trans. Power Electronics,* vol. 22, pp. 1145-1153, Jul. 2007.

[61] R.-J. Wai, and R.-Y. Duan, "High-efficiency bidirectional converter for power sources with great voltage diversity," *IEEE Trans. Power Electronics,* vol. 22, pp. 1986-1996, Sept. 2007.

[62] H. Xiao, and S. Xie, "A ZVS bidirectional dc-dc converter with phase-shift plus PWM control scheme," *IEEE Trans. Power Electronics,* vol. 23, pp. 813-823, Mar. 2008.

[63] H. Sheng, D. Fu, X. Yang, F. Wang, F. C. Lee, "Comparison of ZVS operation modes with and without phase shift for three-level resonant converters," in *Proc. IEEE APEC, 2006.*

[64] D. Fu, "Improved resonant converters with a novel control strategy for high-voltage pulsed power supplies," Master's thesis, Virginia Polytechnic Institute and State University, 2004.

[65] R. W. Erickson, and D. Maksimovic, *Fundamentals of Power Electronics,* Second Edition, Norwell, Mass.: Kluwer Academic, 2001.

[66] L. Chen, and F. Z. Peng, "Dead-time elimination for voltage source inverters," *IEEE Trans. Power Electronics,* vol.23, pp.574-580, Mar. 2008.

[67] G. Seenumani, J. Sun, and H. Peng, "Real-time Power Management of Integrated Power Systems in All Electric Ships Using Time Scale Separation," submitted to *IEEE Transactions On Control System Technology*, 2009.

[68] G. Seenumani, J. Sun, and H. Peng, "Exploiting Time Scale Separation For Efficient Real-Time Optimization Of Integrated Shipboard Power Systems," in *Proc. ASME Dynamic Systems and Control Conference*, 2008.

[69] G. Seenumani, J. Sun and H. Peng, "A Numerically Efficient Iterative Procedure for Hybrid Power System Optimization Using Sensitivity Functions," in *Proc. American Control Conference*, 2007.

[70] S. Chattopadhyay and S. Das, "A digital current-mode control technique for DC-DC converters," *IEEE Trans. Power Electronics,* vol. 21, pp.1718-1726, Nov. 2006.

[71] M. Chen, A. Mathew, and J. Sun, "Nonlinear current control of single-phase PFC converters," *IEEE Trans. Power Electronics,* vol. 18, pp.2187-2194, Nov. 2007.

[72] Y. Lu, K. W. E. Cheng, and S. L. Ho, "Quasi current mode control for the phase-shifted series resonant converter," *IEEE Trans. Power Electronics,* vol. 23, pp.353-358, Jan. 2008.

[73] J. Sun and M. Chen, "Nonlinear average current control using partial current measurement," *IEEE Trans. Power Electronics,* vol. 23, pp.1641-1648, Jul. 2008.

[74] R. Redl and I. Novak, "Instabilities in current-mode controlled switching voltage regulators," in *Proc. IEEE Power Electronics Specialists Conf. (PESC),* 1981, pp.17-28.

[75] S. Kouro, P. Cortes, R. Vargas, U. Ammann, and J. Rodriguez, "Model predictive control-a simple and powerful method to control power converters," in *IEEE Trans. Industrial Electronics,* vol. 56, pp.1826-1838, Jun. 2009.

[76] T. Geyer, G. Papafotiou, and M. Morari, "Model predictive direct torque control-part I: concept, algorithm, and analysis," in *IEEE Trans. Industrial Electronics,* vol. 56, pp.1894-1905, Jun. 2009.

[77] T. Geyer, G. Papafotiou, and M. Morari, "Model predictive direct torque control-part II: implementation and experimental evaluation," in *IEEE Trans. Industrial Electronics,* vol. 56, pp.1906-1915, Jun. 2009.

[78] E. I. Silva, B. P. McGrath, D. E. Quevedo, and G. C. Goodwin, "Predictive control of a flying capacitor converter," in *Proc. American Control Conference*, 2007, pp.3763-3768.

[79] S. Qin and T. Badgwell, "A survey of industrial model predictive control technology," *Control engineering practice*, vol. 11, pp.733-764, 2003.

[80] D. Q. Mayne, J. B. Rawlings, C. V. Rao, and P. O. M. Scokaert, "Constrained model predictive control: stability and optimality," *Automatica,* vol. 36, pp.789-814, Jun. 2000.

[81] M. Morari and J. Lee, "Model predictive control: past, present and future," *Computers and Chemical Engineering*, vol. 23, pp.667-682, 1999.

[82] G. Pannocchia, and A. Bemporad, "Combined design of disturbance model and observer for offset-free model predictive control," *IEEE Trans. Automatic Control,* vol. 52, pp.1048-1053, Jun. 2007.

[83] F. Borrelli, and M. Morari, "Offset free model predictive control," in *Proc. IEEE Conference on Decision and Control*, 2007, pp.1245-1250.

[84] V. L. Bageshwar, and F. Borrelli, "Observer pole placement limitations for a class of offset-free model predictive controllers," in *Proc. American Control Conference*, 2008, pp.447-452.

[85] G. Pannocchia and J. B. Rawlings, "Disturbance models for offset-free MPC control," *AIChE Journal,* vol. 49, pp.426-437, 2002.

[86] A. Bemporad, M. Morari, V. Dua, and E. N. Pistikopoulos, "The explicit linear quadratic regulator for constrained systems," *Automatica,* vol. 38, pp.3-20, Jan. 2002.

[87] P. T∅ndel, T. A. Johansen, and A. Bemporad, "An algorithm for multi-parametric quadratic programming and explicit MPC solutions," *Automatica,* vol. 39, pp.489-497, Mar. 2003.

[88] T. Geyer, G. Papafotiou, and M. Morari, "Hybrid model predictive control of the step-down DC-DC converter," *IEEE Trans. Control Systems Technology,* vol. 16, pp.1112-1124, Nov. 2008.

[89] Y. Wang and S. Boyd, "Fast model predictive control using online optimization," in *Proc. of the 17th IFAC World Congress*, 2008, pp.6974-6997.

[90] R. Ghaemi, J. Sun, and I. Kolmanovsky, "An integrated perturbation analysis and sequential quadratic programming approach for model predictive control," *Automatica*, vol. 45, pp. 2412-2418, Sep. 2009.

[91] R. Ghaemi, J. Sun, and I. Kolmanovsky, "Neighbering extremal solution for nonlinear dicrete-time optimal control problems with state inequality constraints," *IEEE Trans. Automatic Control,* vol. 54, 2009.

[92] Y. Xie, G. Seenumani, and J. Sun, "Real-time simulation and optimization of multi-scale shipboard power systems," in *Proc. Grand Challenges in Modelling and Simulation,* 2008.

[93] Y. Xie, G. Seenumani, J. Sun, Y. Liu, and Z. Li, "A PC-cluster cased real-time simulator for all electric ship integrated power systems analysis and optimization," in *Proc. IEEE Electric Ship Technology Symposium (ESTS),* 2007.

[94] Y. Xie, J. Sun, and J. S. Freudenberg, "Power flow characterization of a bidirectional galvanically isolated high power DC/DC converter over a wide operating range," *IEEE Trans. Power Electronics,* 2010.

[95] Y. Xie, J. Sun, and J. S. Freudenberg, "Development of a CM-PWM for a dual active bridge DC/DC converter," submitted to *IEEE Transaction on Power Electronics,* 2009.

[96] Y. Xie, R. Ghaemi, J. Sun, and J. S. Freudenberg, "Implicit model predictive control of a full bridge DC/DC converter", to appear, *IEEE Trans. Power Electronics,* 2009.

[97] Y. Xie, R. Ghaemi, J. Sun, and J. S. Freudenberg, "Nonlinear model predictive control for a isolated high power full bridge DC/DC converter," submitted to, *IEEE Trans. Control System Technology,* 2010.

[98] Y. Xie, R. Ghaemi, J. Sun, and J. S. Freudenberg, "Comparative evaluation of linear and nonlinear model predictive control for a isolated high power full bridge DC/DC converter," submitted to, *American Control Conference (ACC'10),* 2010.

[99] Y. Xie, J. Sun, C. Mi, and J. S. Freudenberg, "Analysis and modeling of a DC hybrid power system testbed for power management strategy development," in *Proc. IEEE Vehicle Power and Propulsion Conf. (VPPC'09),* 2009.

[100] Y. Xie, J. Sun, and J. S. Freudenberg, "Integrated voltage regulation and current-sensorless power tracking control for a DC hybrid power system," in Proc. *American Control Conference (ACC'08)*, 2008.

[101] W. S. Levine, *The control handbook,* CRC Press and IEEE Press, 1996.

[102] G. G. Kulikov, and H. A. Thompson, *Dynamic Modelling of Gas Turbines*, Springer.

[103] P. Moraal, and I. Kolmanovsky, "Turbocharger modeling for automotive control applications," *Journal of Eng. For Gas Turbines and Power*, 2003.

[104] C. Kong, J. Ki, and M. Kang, "A new scaling method of component maps of Gas Turbines using system identification," in *Proc. American Control Conference*, 2004.

[105] J. Kurzke, and C. Riegler, "A new compressor map scaling procedure for preliminary conceptional design of gas turbines," in *Proc. ASME IGTI*, 2000.

[106] J. T. Pukrushpan, A. G. Stefanopoulou, and H. Peng, *Control of fuel cell power systems,* Springer.

[107] J. S. Freudenberg, *A first graduate course in feedback control,* 2006.